Dissertation for the Degree of Doctor of Philosophy

Control of MMC-HVDC System and Its Application to the Jeju Island Power System

Quach Ngoc Thinh

Faculty of Applied Energy System

Major of Electrical Engineering

GRADUATE SCHOOL

JEJU NATIONAL UNIVERSITY

December 2014

Control of MMC-HVDC System and Its Application to the Jeju Island Power System

Quach Ngoc Thinh

(Supervised by Professor Ho-Chan Kim)

A thesis submitted in partial fulfillment of the requirements

for the degree of Doctor of Philosophy

2014. 12

This thesis has been examined and approved

....

Thesis director, Seong-Bo Oh, Prof. of Electrical Engineering

Se-Ho Kim ....

Gae-Myoung Lee ....

Bong-Woon Ko...

Ho-Chan Kim...

Faculty of Applied Energy System

Major of Electrical Engineering

GRADUATE SCHOOL

JEJU NATIONAL UNIVERSITY

ACKNOWLEDGEMENTS

CONTENTS

LIST OF FIGURES

LIST OF TABLES

LIST OF ABBREVIATIONS

MMC	Modular multilevel converter
VSC	Voltage source converter
LCC	Line-commutated current source converter
CSC	Line-commutated current source converter
HVDC	High-voltage direct current
HVAC	High-voltage alternating current
DC	Direct current
AC	Alternating current
PI	Proportional-integral
PR	Proportional-resonant
PCC	Point of common coupling
SM	Submodule
GTO	Gate turn-off thyristor
IGBT	Insulated gate bipolar transistor
PWM	Pulse-width modulation
SPWM	Sinusoidal pulse-width modulation
SHE PWM	Selective harmonic elimination pulse-width modulation
OHSW	Optimized harmonic stepped waveform
SVM	Space vector modulation
NLM	Nearest level modulation
PS	Phase-shifted
LS	Level-shifted
PD	Phase disposition
POD	Phase opposite disposition
APOD	Alternative phase opposite disposition
STR	Saw-tooth rotation
THD	Total harmonic distortion
RMS	Root mean square
PLL	Phase-locked loop
EMF	Electromotive force

αβ   Stationary reference frame

dq   Synchronous rotating reference frame

CB   Circuit breaker

SUMMARY

This dissertation presents an analysis and control of a MMC-HVDC system under various conditions and its application to Jeju Island power system. The MMC is a promising converter topology for the HVDC applications. Thus, the structure and operating principle of the MMC should be understood well. The suitable selection of the modulation methods will reduce losses in the converter. To design the MMC, the principles to calculate two of main components, namely arm inductance and submodule capacitance, are also important. After getting the parameters, the control methods of the MMC-HVDC system will be analyzed under various operating conditions. The effectiveness is verified by using PSCAD/EMTDC simulation program.

Under normal operating conditions, the aim is to demonstrate that the MMC can operate as a VSC. The operation is tested in three cases:

➢ Independent control of the active and reactive powers

➢ Active power reversal control

➢ AC grid voltage control

Under unbalanced voltage conditions, the HVDC is required to operate reliably without any trip. If the PI controller is used, the operation method of the HVDC will depend on the reference values of the negative sequence currents. That is three cases of controlling:

➢ Eliminating negative sequence currents

➢ Eliminating oscillation of the active power at the PCC

➢ Eliminating oscillation of the reactive power at the PCC

If the PR controller is used, the control aim will be the elimination of the negative sequence currents. The effectiveness of the PI and PR controllers will be compared by using simulation results.

Under nonpermanent DC faults, the control objective is to protect for the IGBTs and diodes in the submodules. In this case, two thyristor switches are used to connect in parallel to the diode D_2 of the submodule. A DC fault will become an AC fault, and the DC fault current will be extinguished. Then, the MMC-HVDC system is back to the normal operation.

The control method to eliminate the circulating current is also analyzed. Under unbalanced voltage conditions, the controller of the circulating current is the PR controller instead of the PI controller.

The application of the MMC-HVDC system in this dissertation is to check its response to

a real system such as Jeju Island power system. In this case, the modeling of the Jeju Island power system in PSCAD/EMTDC simulation program is established based on the parameters and measured data from the real Jeju Island power system. The application is performed in two cases:

➢ The application of the MMC-HVDC system for regulating grid voltage based on the Jeju Island power system. In this simulation, the HVDC #1 is replaced by the MMC-HVDC system. The effectiveness of using the MMC-HVDC system will be verified by comparing to the case of using HVDC #1.

➢ The application of the MMC-HVDC system for stabilizing the Jeju Island power system in 2020. The mission of the MMC-HVDC system is to ensure a power balancing in the Jeju Island power system under different situations. It can transfer the active power from the mainland to the Jeju Island power system and vice versa.

Chapter 1. Introduction

1.1 Background

The rapid and unequal development of the power generation sources like the renewable energy leads to a requirement to transfer power from an area to another area. Especially, the wind power and solar energy sources only focus on the areas where have strong wind velocity and solar radiation. In addition, the power transmission systems to the islands, where are far away from the main energy source, are also necessary. The transmission techniques have been known, including high-voltage alternating current (HVAC) and high-voltage direct current (HVDC) transmissions. The HVAC transmission is suitable to transfer the power over a short distance and in the synchronous systems. Meanwhile, the HVDC transmission is applied to transfer the power over long distance or under the sea because of low losses and cost, especially it has ability of connecting between the asynchronous systems. The HVDC transmission has been used widely in the last several years [1], [2]. There are two kinds of HVDC system, namely line-commutated current source converter (LCC or CSC)-HVDC and voltage source converter (VSC)-HVDC systems [3]. The use of LCC-HVDC is limited in comparison with the VSC-HVDC because of the high costs of the converter infrastructure, requirement of the reactive power and limit controllability. Recently, a new HVDC system has been developed which is called by a modular multilevel converter (MMC)-HVDC system [4]. The MMC is a type of VSC. However, it has many advantages over other VSCs such as low harmonic, high efficiency, high capacity and so on [5]-[7]. Thus, the MMC is a promising converter topology in the near future [8]. The first MMC-HVDC system, Trans Bay Cable, was commissioned in 2010 by Siemens [9]. The HVDC Light from ABB and HVDC Maxsine from Alstom are other examples of MMC application for HVDC system [10]-[11].

The MMC has been researched and analyzed by many authors over the world. The normal operation of the MMC has been introduced in [5]-[7], [12]. In [13], the authors present a control method to achieve capacitor voltage balancing without any external circuit by combining the averaging and balancing controls. Another control method of the capacitor voltage balancing is also proposed in [14]. This method is based on the sort of capacitor voltages and sign of the arm current to switch on/off submodules (SMs). The function of arm inductor and the analysis of circulating current are shown in [15]. The circulating current

suppressing controller is proposed in [16], [17]. The dynamic performances of the MMC-HVDC system are analyzed in [18]. Similar to the other HVDC system, the stable and reliable operations of the system must be researched carefully, especially when the system operates under unbalanced voltage conditions. In [19], [20], the authors show out the control methods of the MMC-HVDC system under unbalanced voltage conditions. However, almost all of them haven't shown out the detail process of design and control of the MMC-HVDC system. Moreover, the authors have just focused on the use of the proportional-integral (PI) controller under balanced and unbalanced voltage conditions, but not on the use of the proportional-resonant (PR) controller. In a control system, a simple controller is necessary, but it still ensures the reliability. The PR controller is one of those controllers [21].

1.2 Objectives

This dissertation presents an analysis and control of the MMC-HVDC system under various conditions and its application to the Jeju Island power system. To have a good understanding of the MMC, the background principles are first introduced, including the operating principle, capacitor voltage balancing, modulation methods, and calculating values of arm inductance and submodule capacitance. Then, the control methods of the MMC-HVDC system under normal operation, unbalanced voltage and DC fault conditions will be analyzed in detail. In case of the unbalanced voltage conditions, the PR controller is also applied to the MMC-HVDC system and compared to the PI controller. Finally, the MMC-HVDC system is applied to the Jeju Island power system. The purpose is to have a general view about the overall operations of the MMC-HVDC system in the power system. The study cases in this dissertation will be modeled and verified by using PSCAD/EMTDC simulation program.

1.3 Dissertation outline

Chapter 2 presents the basic theory of the MMC-HVDC system such as the structure, operating principle, and modulation methods. In addition, the arm inductance and SM capacitance are also explained in this chapter.

Chapter 3 analyzes the operation of the MMC-HVDC system under normal and fault conditions. The control structure and operations of the MMC-HVDC system under normal operating conditions are expressed. The control methods of the negative sequence currents under unbalanced voltage conditions are performed by using the PI and PR controllers.

Under nonpermanent DC fault, the protection method for the MMC-HVDC system with bidirectional thyristor switches is analyzed.

The applications of the MMC-HVDC system to the Jeju Island power system are expressed in chapter 4. It consists of the MMC-HVDC system for regulating the grid voltage based on the Jeju Island power system and the MMC-HVDC system for stabilizing the Jeju Island power system in 2020.

Chapter 5 gives the conclusions of the dissertation.

Chapter 2. Basic Theory of the MMC-HVDC System

2.1 HVDC systems

To transfer a large amount of power over long distance, a HVAC or a HVDC can be used. However, the HVDC transmission systems often provide a more economical alternative the AC transmission systems. A HVDC system with two conductors can transfer the same amount of power as a HVAC system with three conductors. This results in smaller transmission towers and lower line losses than with the AC lines. Moreover, the DC lines do not consume the reactive power, and thus the line investments can be reduced because of the absence of the compensation devices. The savings in line construction are approximate about 30%. The HVDC transmission is favorable for distances exceeding 500 km with the overhead lines and 40 km with the cable systems [22]. There are two kinds of converters which are applied to the HVDC systems, including a LCC and a VSC.

2.1.1 LCC-HVDC system

The LCC using the thyristor valves was introduced during the 1970s. The advantages of the LCC-HVDC system are that it can deliver a large power and operates at the high voltage for the capacity increase and the loss saving. The largest disadvantage is that both the inverter and the rectifier absorb a varying amount of the reactive power from the grid [23]. The simple LCC-HVDC system is shown in Fig. 1. To minimize the harmonic contents, the LCC-HVDC is designed with two 6-pulse bridges in parallel on the AC side and in the series on the DC side. The two bridges are shifted by 30 degrees in phase on the AC side. This phase shift is achieved by feeding one bridge through a transformer with a wye-connected secondary and other bridge through a transformer with delta connected secondary [22].
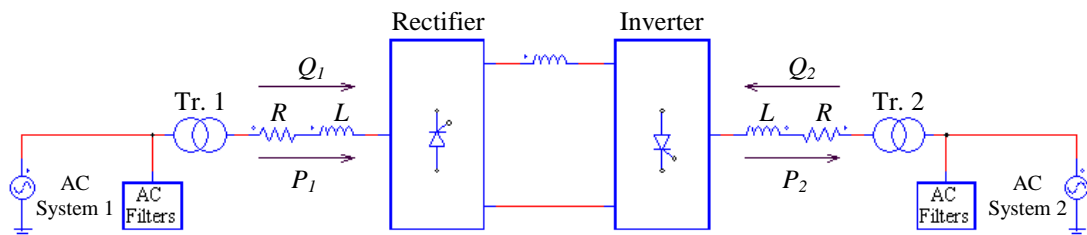
Fig. 1 Configuration of the LCC-HVDC system

2.1.2 VSC-HVDC system

Because of the rapid development of the high power and high voltage semiconductor devices such as GTO and IGBT valves, a VSC is proposed as a new selection for the HVDC system with their advantages such as [3], [24], [25]:

➢ To control the active and reactive powers independently.

➢ To support the reactive power for the power grid.

➢ To connect to the weak and passive grids.

➢ To have the black start capability.

➢ To operate in all four quadrants of the PQ plant.

➢ To have a fast active power reversal.

➢ Don't need special converter transformers.

The simplest VSC-HVDC topology is the conventional two-level three-phase bridge as shown in Fig. 2. It consists of two converter stations. These converters are connected together by using two DC transmission lines that have opposite polarity. The DC side capacitors are used to support and filter the DC-link voltage. The converters are linked to the AC system through phase reactors and power transformers. The phase reactors are responsible for the limitation of fault currents and suppressing current harmonics due to the PWM. In addition, AC filters are also used to eliminate the high-order harmonics from the PWM voltages. The VSC-HVDC system can transfer the power in two directions, from the AC system 1 to the AC system 2 and vice versa, with a constant DC-link voltage.

To increase the power rating and reduce harmonics, the other kinds of VSCs have been developed such as diode-clamped multilevel converter, flying-capacitors multilevel converter and cascade multilevel converter. However, the structure and control of these converters are very complicated. The diode-clamped multilevel converter requires excessive clamping diodes when the number of levels is high. Similarly, the flying-capacitors multilevel converter requires a high number of capacitors for higher number of levels. This converter is also more difficult to package with the bulky power capacitors and more
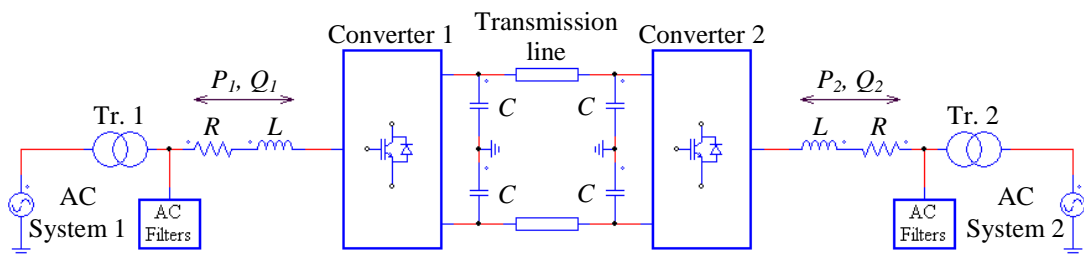
Fig. 2 Configuration of the VSC-HVDC system

expensive. The cascade multilevel converter needs separate DC sources for real power conversions, thereby limiting its applications [26].

2.1.3 MMC-HVDC system

To overcome the disadvantages of the conventional VSC-HVDC systems, a new topology of the VSC-HVDC system has been developed in recent years. It is called by a MMC-HVDC system. This HVDC topology is expected to substitute to the existing VSC-HVDC topologies in the nearest future with their advantages as mentioned in Subsection 2.2.1 [26]. The configuration of the MMC-HVDC system is shown in Fig. 3. Its structure is similar to the VSC-HVDC system in Fig. 2. In this case, the MMCs are used instead of the conventional VSCs. The quality of the output voltage depends on the number of SMs per arm N. If N tends to an infinite value, the output voltage will be near sinusoidal waveform. Thus, the size of the AC filters can be significantly reduced, or even omitted. Moreover, the DC-link capacitor is also not necessary because of the use of the capacitors in the SMs [5].

➤ **Fault ride-through requirements**

A HVDC system is required to remain transiently stable and connected to the system without tripping for a close-up solid three-phase short circuit fault or any unbalanced short circuit fault for a total fault clearance time of up to 140 ms as shown in Fig. 4. The fault will affect the level of active power that can be transferred, and therefore a load reduction or rejection is necessary. When the grid voltage is restored to 90% of nominal or greater within 0.5 s, the active power shall be restored to at least 90% of the level before the fault. During the fault, the converter shall generate maximum reactive power without exceeding the transient rating limit of the converter [27].
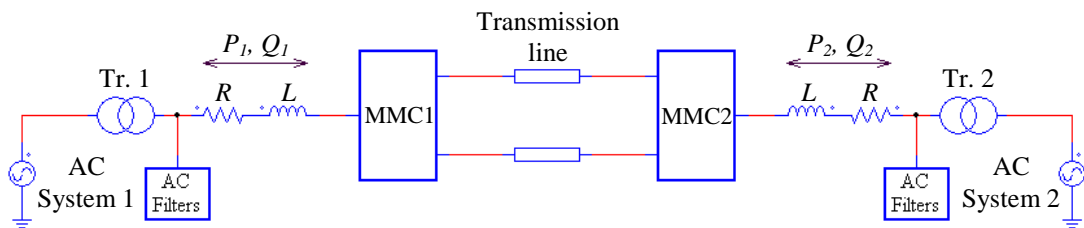
Fig. 3 Configuration of the MMC-HVDC system
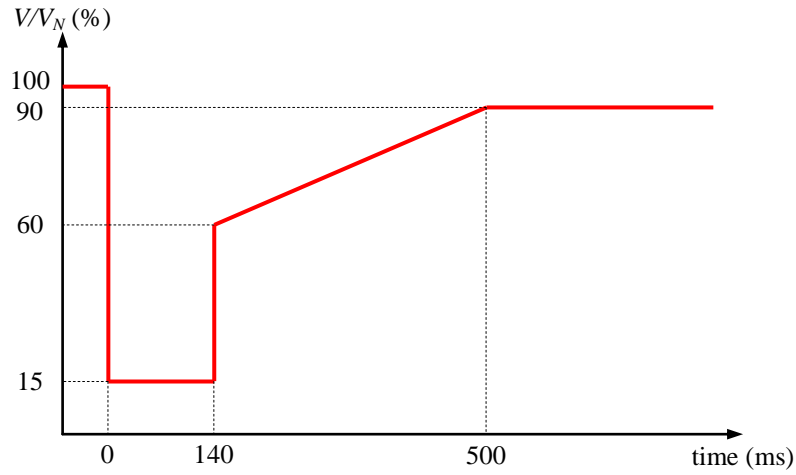
Fig. 4 Fault ride-through requirement

2.2 Modular multilevel converter

2.2.1 Structure and operating principle

The basic structure of the MMC is shown in Fig. 5. It is created by six arms which are arranged as illustrated in Fig. 5(a). Each arm has a total of N SMs connected in series and a series inductor which provides a current control within the phase arms and limits fault
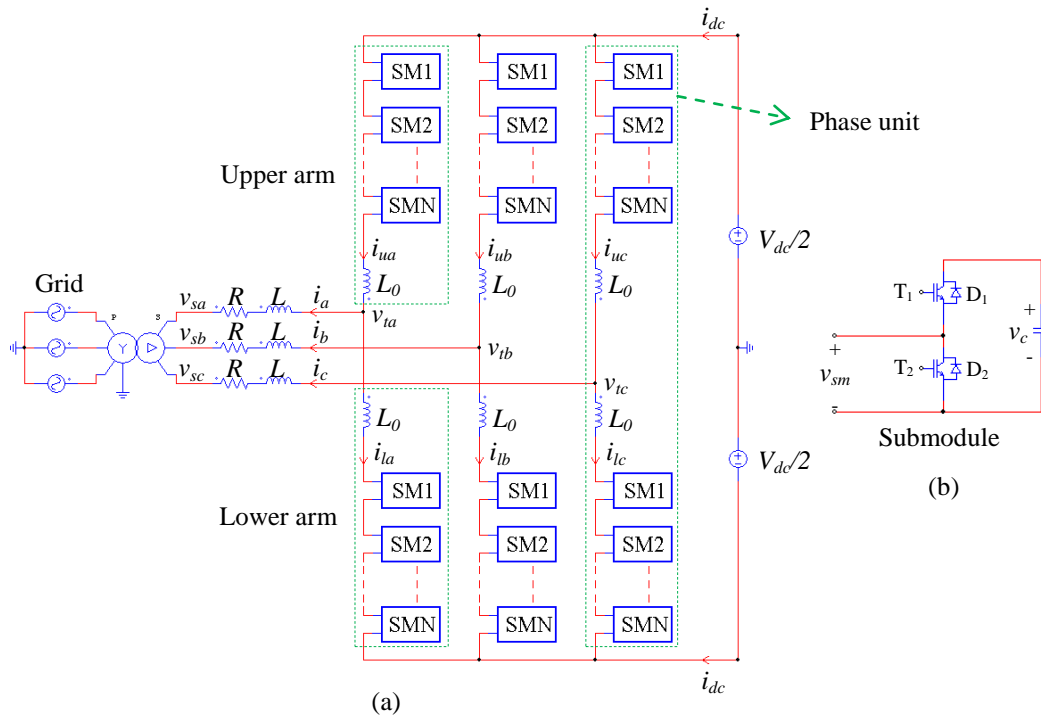
Fig. 5 Circuit diagram of the MMC

currents. Two arms in the same leg comprise a phase unit. A SM is a half-bridge cell that consists of two IGBTs, two anti-parallel diodes, and a capacitor. The AC side of the MMC is connected to the unity grid through a Y-Δ three-phase transformer.

The operations of SM are shown in Fig. 6. The conduction paths of the SM depend on whether the IGBT need to be on or off along with the polarity of the current. There are two states of operation.

On-state: T_1 is switched on and T_2 is switched off. If the current i_{sm} flows into the SM as shown in Fig. 6(a), the capacitor will be charged through the anti-parallel diode D_1. If the i_{sm} flows out of the SM (Fig. 6(b)), the capacitor will be discharged through T_1. In both cases, the output voltage of the SM is equal to the capacitor voltage v_c (neglecting the path voltage drop).

Off-state: T_1 is switched off and T_2 is switched on. If the i_{sm} flows into the SM (Fig. 6(c)), the i_{sm} will pass through the T_2. If the i_{sm} flows out of the SM (Fig. 6(d)), the i_{sm} will pass through the D_2.

Both T_1 and T_2 must never be switched on at the same time because it causes a short circuit across the capacitor. If both T_1 and T_2 are switched off, the current will only conduct through the anti-parallel diodes D_1 and D_2. This case is not useful because it produces different output voltages depending on the current direction.

Each arm of the MMC can operate as a controllable voltage source. Six arms are corresponding to the six controllable voltage sources. These sources must meet the criterion that their voltage sum always has to match the constant DC-link voltage. Thus, if the magnitude of the voltage source in the upper arm is increased, the magnitude of the
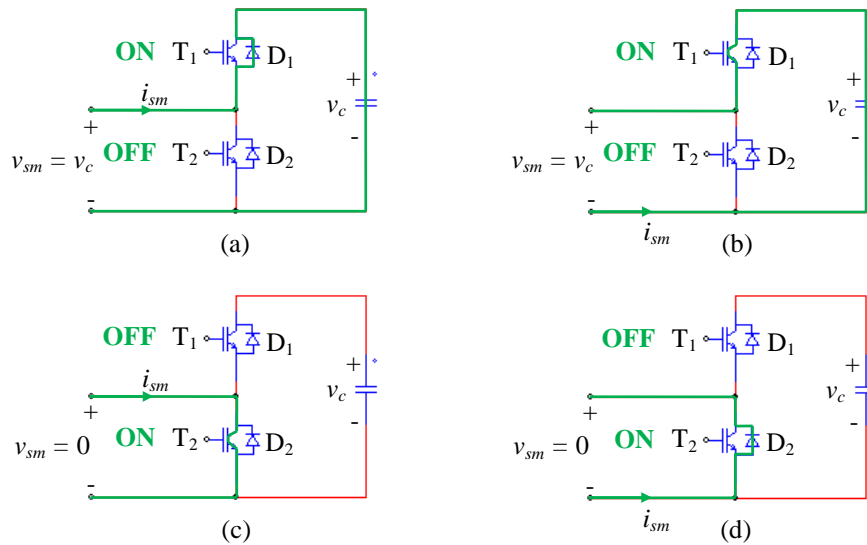
Fig. 6 The operations of submodule

voltage source in the lower arm must be decreased and vice versa. In the MMC, the maximum number of levels of the AC output voltage is related strictly to the number of SMs per each arm. If there are N SMs per each arm, the number of levels of the output voltage will be $N+1$. Each level will be generated depending on the number of SMs in the on-state in upper and lower arms. At any time, N SMs have to be in the on-state and N SMs have to be in the off-state in each phase. This ensures that the DC-link voltage always has a constant value. The value of each level is V_{dc}/N. The output voltage waveform of the MMC is shown in Fig. 7.

The advantages of the MMC are as follows [5]-[7]:

➢ The MMC is structured by the SMs which are connected in series. Thus, it can be easily scaled to different power and voltage levels. In other words, it is easy to change the capacity of the MMC.

➢ The MMC operates at a low switching frequency. Therefore, the semiconductor losses are low. It means that the efficiency of the MMC is increased.

➢ The harmonic contents at the AC side are very low because the output voltage of the MMC is near sinusoidal waveform. Thus, the use of the AC filter can be eliminated.

➢ The MMC can supply a high availability because of the use of redundant SMs in the case of a cell failure.

2.2.2 Mathematical model

Assuming that the MMC is consisting of a large number of the SMs in each arm. Therefore, a selection of the SMs, which are inserted (on-state) or bypassed (off-state), is necessary to balance the capacitor voltages of the SMs. However, this is not really easy
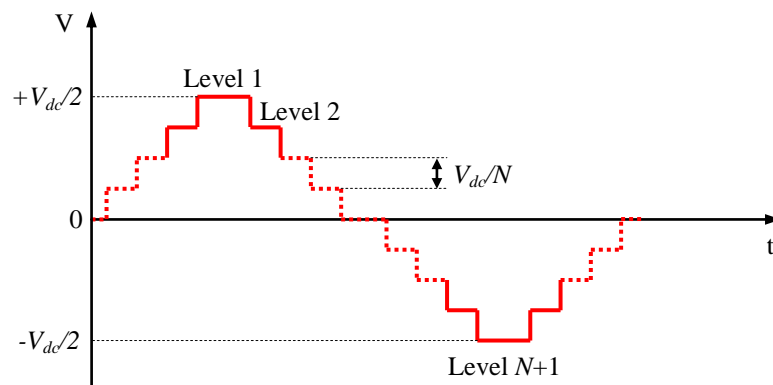
Fig. 7 Output voltage waveform of the MMC

because it requires all of the knowledges of the arm currents and the capacitor voltages in the SMs. As a result, the use of the detailed model to analyze the operation of the MMC is complicated. Thus, a simpler model should be developed to overcome this problem. In [12], the authors have proposed a continuous model for the single-phase MMC. It is able to describe an arm of the MMC as a variable capacitance in series with an equivalent resistance and an arm inductance as shown in Fig. 8. To use the continuous model, it is assumed that the switching frequency and the number of the SMs per arm are infinite. This means that the AC output voltage of the MMC will be a perfect sinusoidal voltage.

Considering the MMC with N SMs per arm, each arm is controlled by an insertion index $m_x(t)$ that is a continuous value and go from 0 to 1. $m_x(t) = 0$ if all N SMs in the arm are bypassed, while $m_x(t) = 1$ if all N SMs in the arm are inserted. If C is the capacitance of each SM capacitor, the effective capacitance of the arm x will be calculated by

$$C_x = \frac{C}{Nm_x(t)} \tag{1}$$

where C is the capacitance of the SM. Subscript x represents the upper and lower arms, $x = u, l$.

If the total voltage of the capacitors in the each arm is $v_{cx}^{\Sigma}(t)$, the inserted arm voltage can be expressed by

$$v_{cx} = m_x(t)v_{cx}^{\Sigma}(t) \tag{2}$$
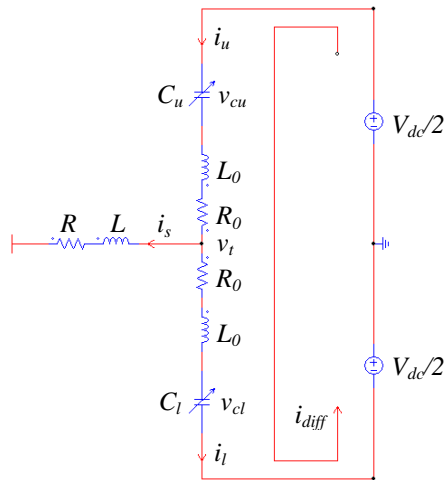
Fig. 8 Continuous model of the single-phase MMC

When the arm current $i_x(t)$ flows through the effective capacitance, the total capacitor voltages are described by

$$\frac{dv_{cx}^{\Sigma}(t)}{dt} = \frac{i_x(t)}{C_x} \tag{3}$$

Assuming that the direction of the arm currents is shown in Fig. 8, the output phase current can be calculated by using the Kirchhoff's current law as

$$i_s = i_u - i_l \tag{4}$$

where i_u and i_l are the upper and lower arm currents.

Because the capacitors are charged or discharged depending on the direction of the arm currents, thus the SM capacitor voltages are not constant. The sum of the capacitor voltages in the phase unit is not equal to the DC-link voltage. There will be a current which flows through both the upper and lower arms. This current is called "inner difference current". If the output phase current is assumed to be equally shared by both the upper and lower arms, the arm currents will be expressed by

$$i_u = i_{diff} + \frac{i_s}{2} \tag{5}$$

$$i_l = i_{diff} - \frac{i_s}{2} \tag{6}$$

Then, the inner difference current can be calculated by

$$i_{diff} = \frac{i_u + i_l}{2} \tag{7}$$

From Fig. 8, the AC voltage will be computed according to the upper and lower arm currents as

$$v_t = \frac{V_{dc}}{2} - R_0 i_u - L_0 \frac{di_u}{dt} - m_u v_{cu}^{\Sigma} \tag{8}$$

or

$$v_t = -\frac{V_{dc}}{2} + R_0 i_l + L_0 \frac{di_l}{dt} + m_l v_{cl}^{\Sigma} \tag{9}$$

11

Subtracting (8) to (9) and expressing for the inner difference current, we get

$$V_{dc} - 2R_0 i_{diff} - 2L_0 \frac{di_{diff}}{dt} - \left(m_u v_{cu}^{\Sigma} + m_l v_{cl}^{\Sigma} \right) = 0 \tag{10}$$

where R_0 and L_0 are the resistor and inductor of arm, respectively.

Finally, the differential equations can be obtained from (1), (3), and (10) as follows.

$$\frac{d}{dt} \begin{bmatrix} i_{diff} \\ v_{cu}^{\Sigma} \\ v_{cl}^{\Sigma} \end{bmatrix} = \begin{bmatrix} -\dfrac{R_0}{L_0} & -\dfrac{m_u}{2L_0} & -\dfrac{m_l}{2L_0} \\ \dfrac{Nm_u}{C} & 0 & 0 \\ \dfrac{Nm_l}{C} & 0 & 0 \end{bmatrix} \begin{bmatrix} i_{diff} \\ v_{cu}^{\Sigma} \\ v_{cl}^{\Sigma} \end{bmatrix} + \begin{bmatrix} \dfrac{V_{dc}}{2} \\ \dfrac{Nm_u i_s}{2C} \\ -\dfrac{Nm_l i_s}{2C} \end{bmatrix} \tag{11}$$

From (4), (8), (9), and (10), it can be seen that the inner different current does not affect to the output phase current and voltage. It only depends on the DC-link voltage and the inserted arm voltage.

2.3 Capacitor voltage balancing control

In the MMC, there are only two states which have no complicated configurations, that is the generation of the maximum positive and negative voltages. For generating the other levels, there are several possible switching configurations that can determine which SMs will be in the on-state or the off-state. The problem is how to keep a balance in the capacitor voltages. A balancing failure in the capacitor voltages not only distorts the output voltage but also results in equipment damage if individual SM voltages fluctuate outside of the rated values of the equipment. Moreover, an unbalance in the capacitor voltages among three phase units leads to the circulating currents that flow through the six arms and distort the arm currents. This causes the increasing losses in the arms [5].

The magnitude of the capacitor voltages of the SMs will be changed depending on the on-state/off-state and the direction of the arm current. Therefore, the selection of the SMs will be used to balance the capacitor voltages. When the SMs are in the on-state, the capacitor voltages will increase if the current is positive. If the current is negative, the capacitor voltages will decrease. When the SMs are in the off-state, the capacitor voltages remain constant without considering the direction of the current.

Based on these characteristics, a procedure for balancing the capacitor voltages is

performed as follows [14]. For each PWM period, the capacitor voltages of each arm are measured and sorted in ascending order. The sign of the arm current and the number of required SMs are determined. If the arm current is positive, the SMs with the lowest capacitor voltages will be in the on-state. Hence, the capacitors of those SMs are charged, and the capacitor voltages increase and conform to the other capacitor voltages. If the arm current is negative, the SMs with the highest capacitor voltages will be in the on-state. The capacitors are discharged and the capacitor voltages decrease. With this procedure, all capacitor voltages in the arm will be balanced, and it will oscillate within a small voltage band that is typical about ±5~10%. This procedure can be summarized in Fig. 9.

To illustrate for this method, a simulation is set up for a MMC that has 20 SMs per arm. The rated power is 20 MW. The average capacitor voltage is 1 kV. The capacitor voltages of SMs in upper and lower arms are shown in Fig. 10. By applying the capacitor voltage balancing method for the MMC, the capacitor voltages in each arm are balanced together. The capacitor voltages in the upper arm are almost the same amplitude with the capacitor voltages in the lower arm, but it is shifted by 180^0 in phase.
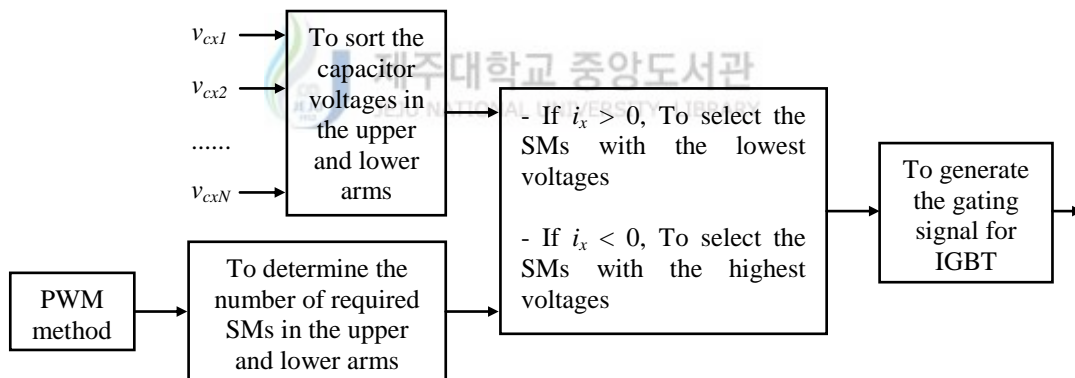
Fig. 9 Block diagram of the capacitor voltage balancing control for the MMC
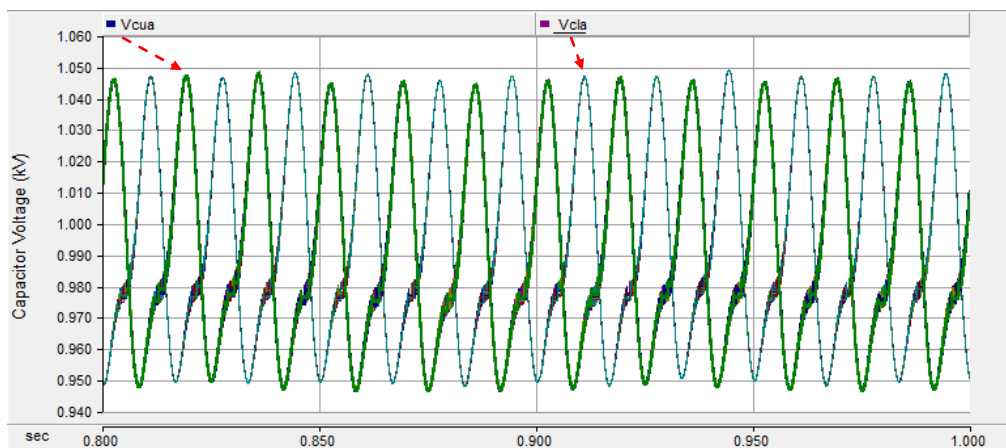
Fig. 10 Capacitor voltage balancing

2.4 Modulation methods

Generally, the modulation methods of the MMC may be classified into selective harmonic elimination pulse-width modulation (SHE PWM), optimized harmonic stepped waveform (OHSW), sinusoidal pulse-width modulation (SPWM), space vector modulation (SVM), and nearest level modulation (NLM) as shown in Fig. 11 [28]-[34]. It is accepted that the performance of a converter with any modulation methods can be related to the harmonic contents of the output voltage and switching losses. Each method has its own advantages and disadvantages. This section will explain the principle of the SPWM and NLM which are most commonly used for the MMC.

2.4.1 Multicarrier sinusoidal pulse-width modulation method

The sinusoidal pulse-width modulation (SPWM) is one of the conventional methods used for control of VSCs which are single-phase/three-phase half-bridge or full-bridge converters. In this method, a modulating or reference signal is compared to a carrier wave to generate gating signals for the IGBT valves. A MMC is structured by several SMs, which are the half-bridge cell and need to be individually controlled. It means that each SM will require a carrier wave. Because of using a lot of carrier waves, the SPWM method for the MMC is
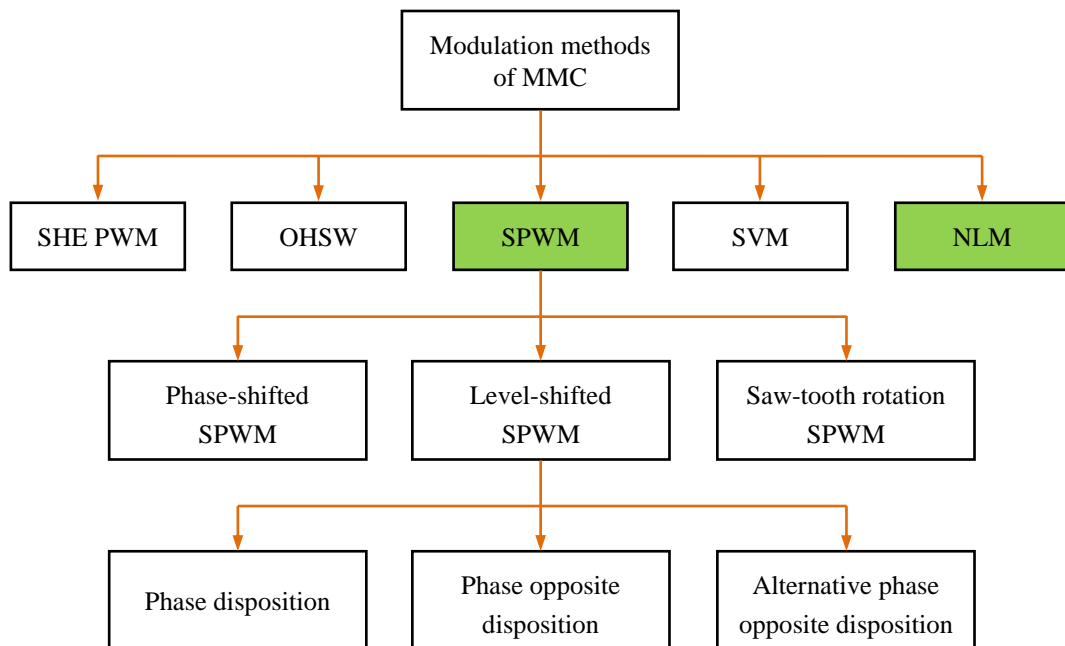
Fig. 11 Modulation methods of the MMC

considered as a multicarrier SPWM method. Depending on the arrangement of the carrier waves, this method is classified into categories as follows [29]-[31].

2.4.1.1 Phase-shifted SPWM method

A MMC with (N+1) levels requires N triangular carrier waves. In the phase-shifted SPWM (PS-SPWM) method, all carrier waves have the same frequency and the same peak-to-peak amplitude, but there is a phase shift between two adjacent carrier waves. This phase shift is given by

$$\varphi_{cr} = \frac{360^0}{N} \tag{12}$$

To generate the gating signals for the IGBTs, the reference signal is compared to all carrier waves. The frequency and amplitude modulation indices are calculated by

$$m_f = \frac{f_{cr}}{f_m} \tag{13}$$

$$m_a = \frac{V_m}{V_{cr}} \tag{14}$$

where m_f and m_a are the frequency and amplitude modulation indices, respectively. f_{cr} and f_m are the frequencies of the carrier and reference waves. V_{cr} and V_m are the peak amplitudes of the carrier and reference waves, respectively. The frequency modulation index relates the device switching frequency to the fundamental frequency of the converter, while the amplitude modulation index relates the difference in deviation between the carrier and reference waves.

To illustrate for the modulation methods, a 5-level MMC is taken as an example. In this case, each arm of the MMC comprises 4 SMs which are connected in series together as shown in Fig. 12. The DC-link voltage is ±200 V.
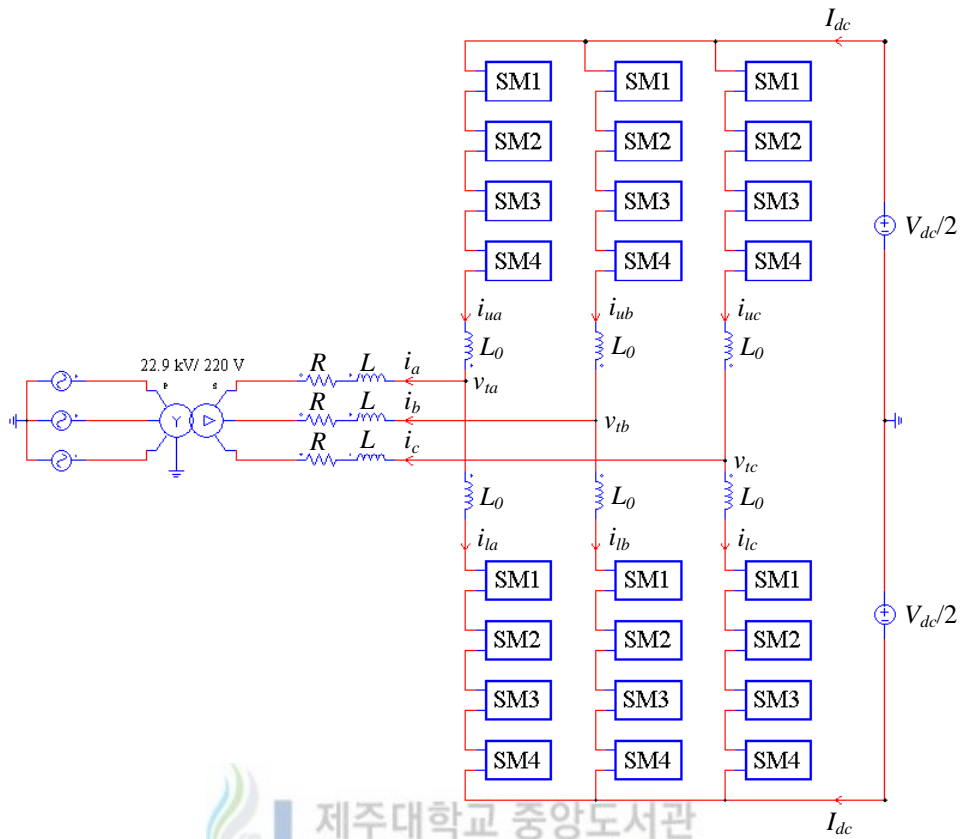
Fig. 12 Circuit diagram of the 5-level MMC

Fig. 13 shows the PS-SPWM method for the 5-level MMC. Four triangular carrier waves are required. Each carrier wave is phase-shifted 90^0 to the others as seen in Fig. 13(a). The output voltage has five levels in its waveform with a high switching frequency. Thus, the harmonics can be reduced. The harmonics are positioned as sidebands around Nf_{cr}. The higher number of levels of the converter, the gap between the fundamental and the first significant harmonics is wider. The PS-SPWM has device switching frequency equal to the carrier frequency. The output currents are the sinusoidal waveforms and contain the harmonics which their amplitudes are small as shown in Fig. 13(c).

2.4.1.2 Level-shifted SPWM method

The level-shifted SPWM (LS-SPWM) method is similar to the PS-SPWM method. With N SMs per arm, it needs N carrier waves that are the same amplitude and frequency. The frequency modulation index is also calculated by using (13). The difference is that the carrier waves are vertically disposed and their bands are contiguous. The amplitude modulation index is expressed by
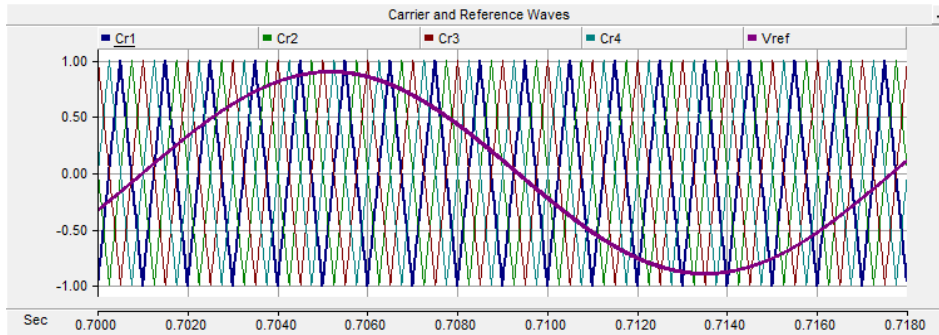
(a)
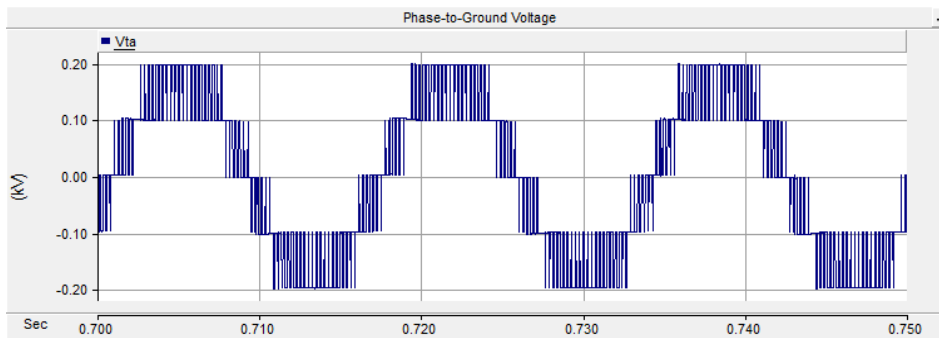
(b)
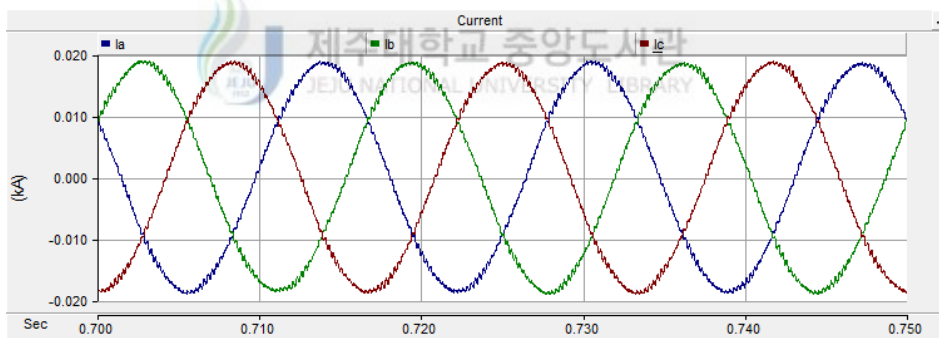
(c)

Fig. 13 Phase-shifted PWM method

$$m_a = \frac{V_m}{NV_{cr}} \tag{15}$$

In this method, each carrier wave only covers a small portion of the reference signal range, and it can affect at a time on the output signal. Total switching of all SMs in each arm will be equal to the carrier frequency. This is also one of the different points to the PS-SPWM method.

Depending on the phase disposition of the carrier waves, the LS-SPWM method can be classified into three cases such as a phase disposition (PD), phase opposite disposition (POD) and alternative phase opposite disposition (APOD).
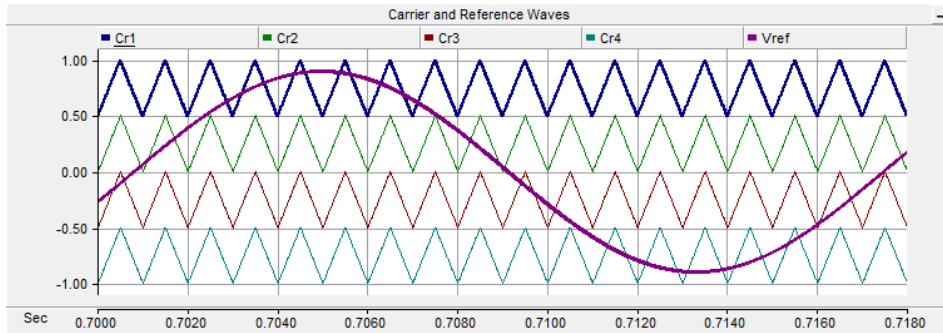
(a)
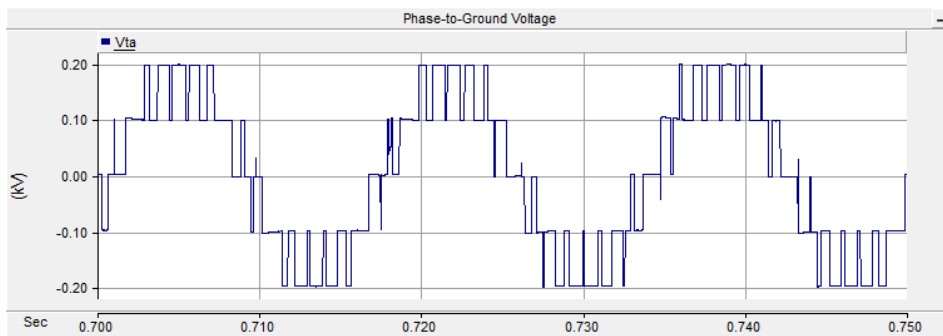
(b)
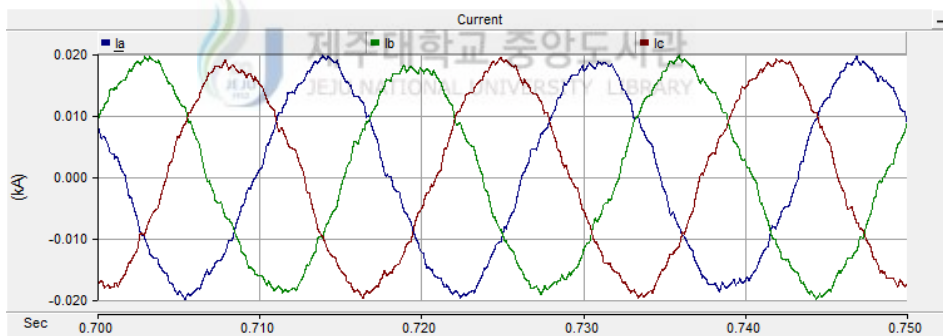
(c)

Fig. 14 Phase disposition SPWM method

A. Phase disposition method

In the PD method, all carrier waves are in phase. Each carrier wave is different to the adjacent one by the voltage offset as shown in Fig. 14. The switching frequency in the output voltage is low, and thus the harmonics will be high in both voltage and current.

B. Phase opposite disposition method

The POD method uses two kinds of carrier waves, the positive and negative carrier waves.
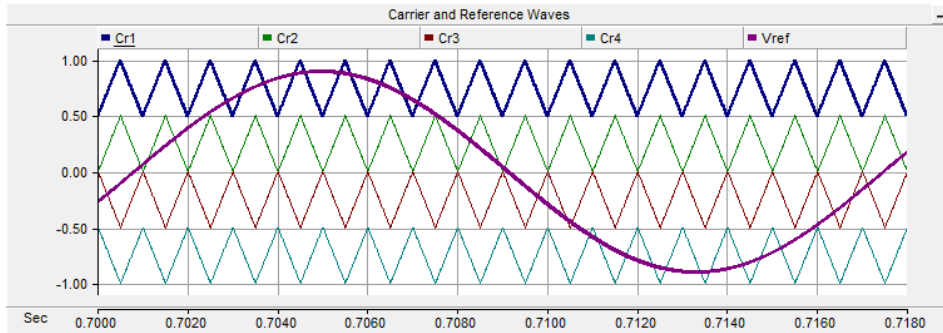
(a)
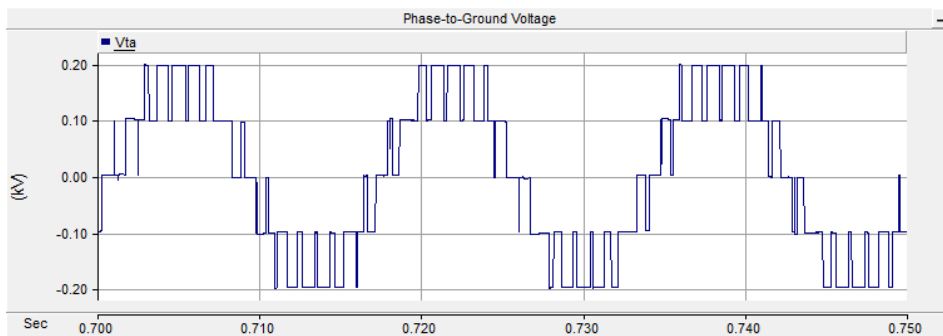
(b)
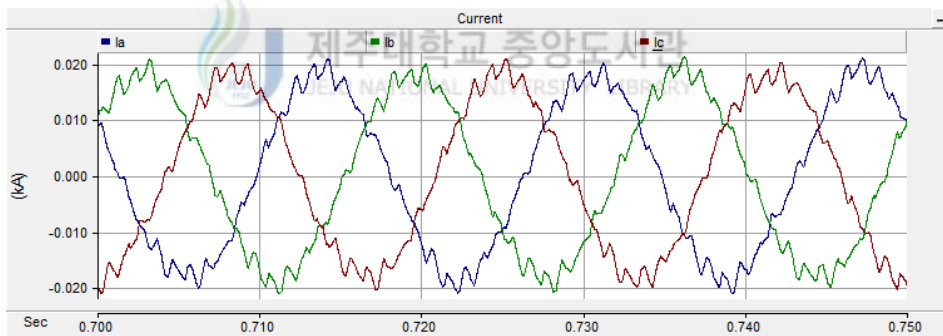
(c)

Fig. 15 Phase opposite disposition SPWM method

The negative carrier waves are shifted by 180^0 with respect to the positive carrier waves. The principle of this method is shown in Fig. 15.

C. Alternative phase opposite disposition method

In the APOD method, the carrier waves are alternately displaced 180^0 between them. The disposition of the carrier waves is described in Fig. 16. Similar to the PD and POD methods, the harmonics in the voltage and current are high with this method.
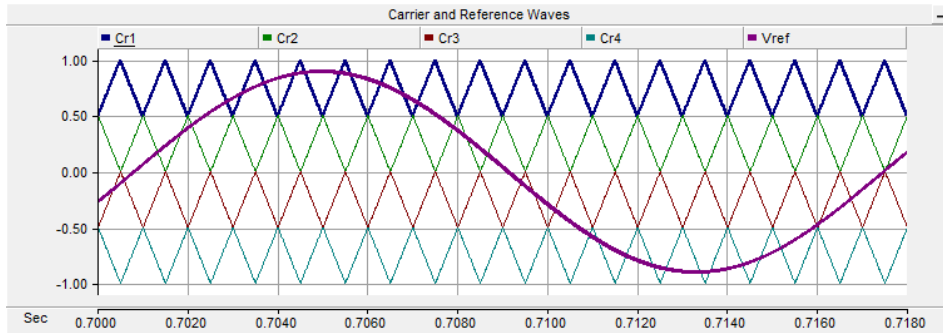
(a)
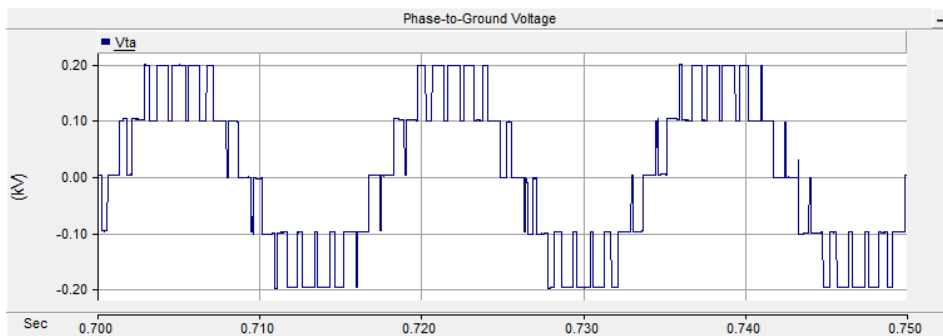
(b)
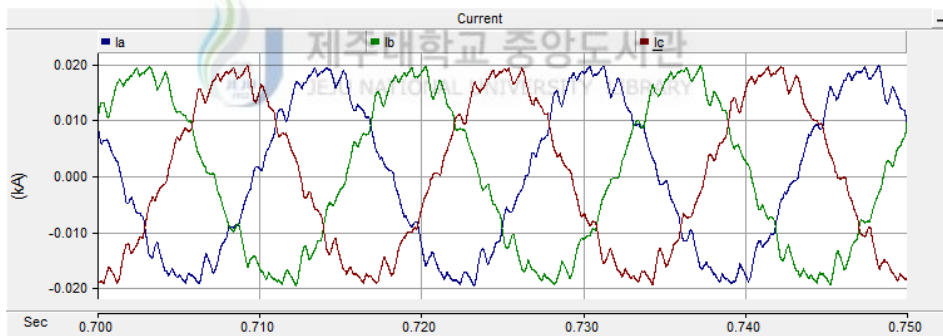
(c)

Fig. 16 Alternative phase opposite disposition SPWM method

2.4.1.3 Saw-tooth rotation SPWM method

The saw-tooth rotation SPWM (STR-SPWM) method is similar to the PS-SPWM method. The difference is that the carrier waves are the saw-tooth waveforms instead of the triangular waveforms. This method also gives a high switching frequency in the output voltage as shown in Fig. 17. Thus, the STR- and PS-SPWM methods will improve significantly the problem of harmonic that has been mentioned in the PD, POD, and APOD methods. However, the high switching frequency causes high losses in the semiconductor devices.
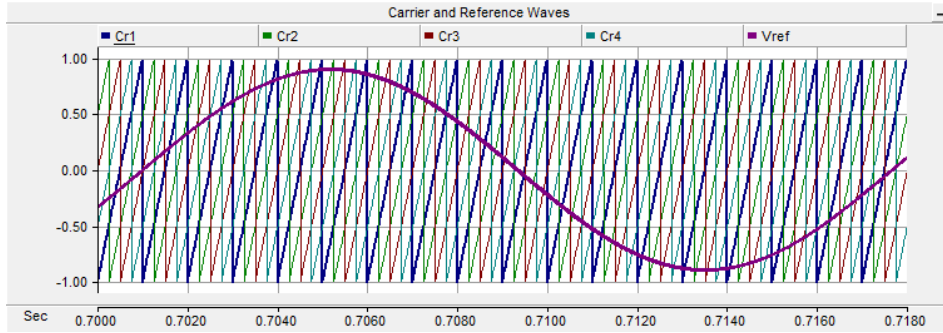
(a)
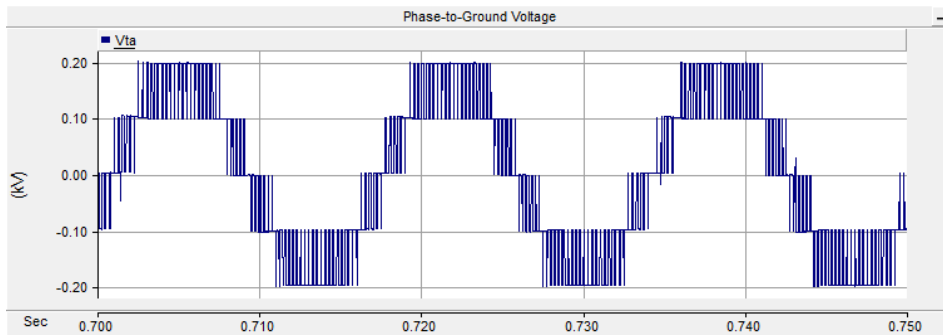
(b)
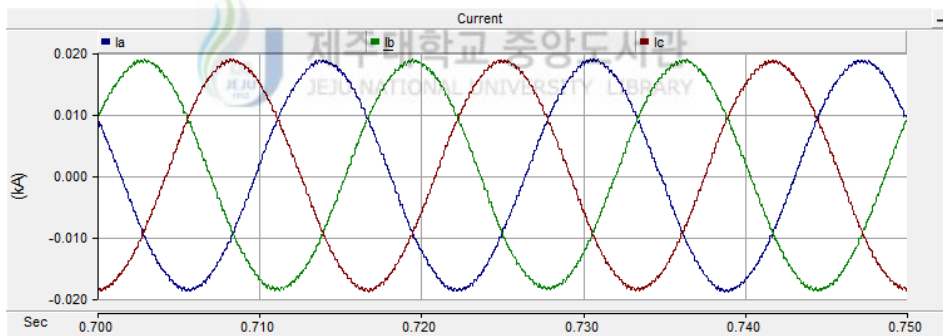
(c)

Fig. 17 Saw-tooth rotation SPWM method

2.4.2 Nearest level modulation method

Assuming that the MMC has N SMs per arm or there are (N+1) levels in the output voltage. V_c represents the average capacitor voltage of all the SMs in phase j, $j = a, b, c$.

$$V_c = \frac{V_{dc}}{N} \tag{16}$$

Let v_{ref_j} is the reference voltage of phase j. The number of SMs in the on-state in the upper and lower arms can be calculated by [14], [33], [34].

21

$$N_{ON\_ju} = \text{int}\left(\frac{0.5V_{dc} - v_{ref\_j}}{V_c}\right) \tag{17}$$

$$N_{ON\_jl} = \text{int}\left(\frac{0.5V_{dc} + v_{ref\_j}}{V_c}\right) \tag{18}$$

where int(y) will get the nearest integer of y. At any time, total of SMs in the on-state in each phase is equal to the number of SMs per arm as given by

$$N = N_{ON\_ju} + N_{ON\_jl} \tag{19}$$

Thus, the number of SMs in the off-state in the upper and lower arms is expressed as

$$N_{OFF\_ju} = N - N_{ON\_ju} \tag{20}$$

$$N_{OFF\_jl} = N - N_{ON\_jl} \tag{21}$$

The output voltage and current of the MMC with the nearest level modulation (NLM) method are shown in Fig. 18. The switching frequency of this method is very low, this leads to the high harmonics. The output current is distorted as seen in Fig. 18(b). Therefore, the NLM method will be suitable for the MMC with a large number of levels.
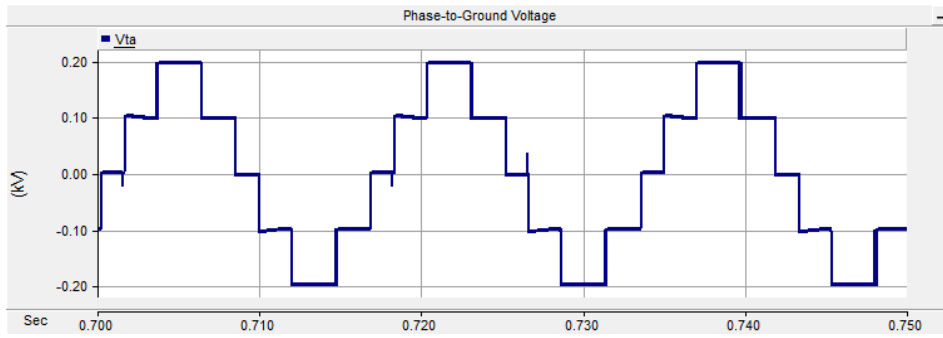
(a)
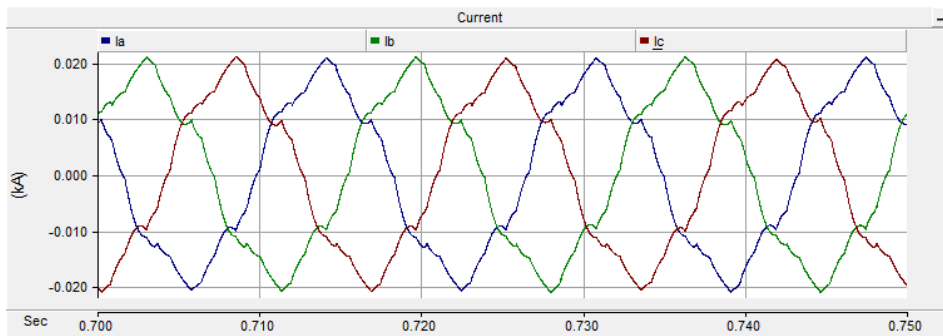
(b)

Fig. 18 Nearest level modulation method

2.4.3 Evaluation of the modulation methods

The quality of the output voltage is one of the important criteria to design a converter system. This relates to the harmonic contents of the output voltage waveform that depend on the modulation method. Total harmonic distortion (THD) of the output voltage and current waveforms is shown in Fig. 19. The PD, POD and APOD methods have a low switching frequency. This leads to low semiconductor device losses and high THD. To reduce the THD, the level number of MMC must be increased. However, if the level number of MMC is very large, these methods will be impossible because the MMC will require an enormous resource of the triangular waveforms. The PS and STR methods have a high switching frequency. It means that the losses are high, and the THD will be low. Hence, the PS and STR methods can be applied to low level MMCs. The NLM method can achieve a very low switching frequency without considering the level number of MMC. Moreover, the NLM method does not need any carrier waves. Thus, this modulation method is suitable for high level MMCs.

2.5 Design of the arm inductance and submodule capacitance

2.5.1 Arm inductance

In the MMC, the arm inductors are connected in series with the SMs in each arm. The
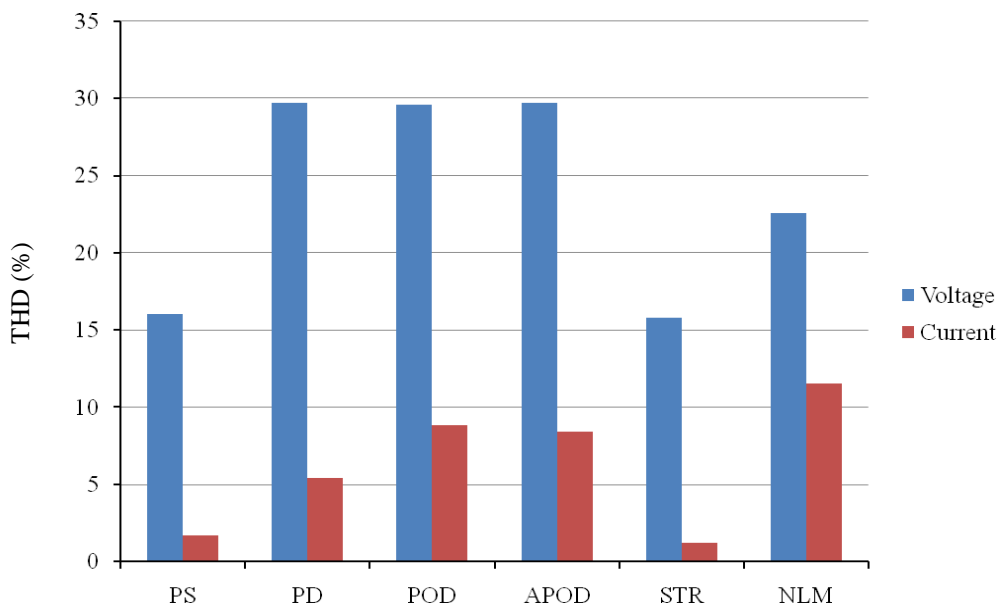
Fig. 19 Comparing THD between the modulation methods

purpose is to compensate for the difference voltage between the total voltage of capacitors in a phase unit and the DC-link voltage. This difference voltage causes the circulating currents that only flow within the three phase units and don't affect to the AC side as shown in Fig. 20. In other words, the arm inductors will eliminate these circulating currents, and thus the losses in the arms will be reduced.

As analyzed in Subsection 2.2.2, the upper and lower arm currents are expressed by [12], [34]

$$i_{uj} = \frac{i_j}{2} + i_{diffj} = \frac{i_j}{2} + \frac{I_{dc}}{3} + i_{cirj} \tag{22}$$

$$i_{lj} = -\frac{i_j}{2} + i_{diffj} = -\frac{i_j}{2} + \frac{I_{dc}}{3} + i_{cirj} \tag{23}$$

where I_{dc} is the DC current. i_{cirj} is the AC component at double fundamental frequency in phase j of the inner difference current named "circulating current".

To make a simple in the calculation, the phase A is taken as an example. The most significant component in the circulating current is the second-order harmonic component [35], [36]. Therefore, the sinusoidal waveforms of the upper and lower arm currents in phase A can be rewritten as
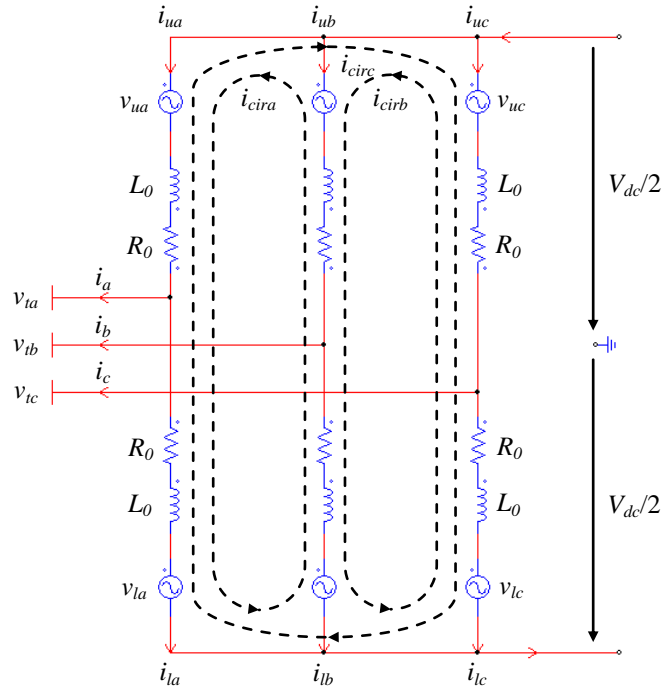
Fig. 20 Circulating currents in the MMC

$$i_{ua} = \frac{I_{ma}}{2}\sin(\omega t + \varphi) + \frac{I_{dc}}{3} + I_{cira}\cos(2\omega t + \varphi_0) \qquad (24)$$

$$i_{la} = -\frac{I_{ma}}{2}\sin(\omega t + \varphi) + \frac{I_{dc}}{3} + I_{cira}\cos(2\omega t + \varphi_0) \qquad (25)$$

where I_{ma} is the amplitude of the output current and φ is the corresponding phase angle. I_{cira} and φ_0 denote the amplitude and the phase angle of the circulating current.

The insertion indices of the upper and lower arms are defined as [12], [36]-[38]

$$m_{ua} = \frac{1}{2}\left(1 - m_v\sin(\omega t)\right) \qquad (26)$$

$$m_{la} = \frac{1}{2}\left(1 + m_v\sin(\omega t)\right) \qquad (27)$$

where m_v denotes the modulation index and is defined by

$$m_v = \frac{2\sqrt{2}V_s}{V_{dc}} \qquad (28)$$

V_s is the RMS value of the output voltage. The insertion indices describe how many modules, on average, are connected in each arm. The average capacitor current of the upper arm is calculated as

$$i_{cua} = m_{ua}i_{ua} = \frac{1}{2}\left(1 - m_v\sin(\omega t)\right)\left[\frac{I_{ma}}{2}\sin(\omega t + \varphi) + \frac{I_{dc}}{3} + I_{cira}\cos(2\omega t + \varphi_0)\right]$$
$$= i_{cua0} + i_{cua1} + i_{cua2} + i_{cua3} \qquad (29)$$

where

$$i_{cua0} = \frac{1}{6}I_{dc} - \frac{1}{8}m_vI_{ma}\cos\varphi \qquad (30)$$

$$i_{cua1} = -\frac{1}{6}m_vI_{dc}\sin(\omega t) + \frac{1}{4}I_{ma}\sin(\omega t + \varphi) + \frac{1}{4}m_vI_{cira}\sin(\omega t + \varphi_0) \qquad (31)$$

$$i_{cua2} = \frac{1}{8}m_vI_{ma}\cos(2\omega t + \varphi) + \frac{1}{2}I_{cira}\cos(2\omega t + \varphi_0) \qquad (32)$$

$$i_{cua3} = -\frac{1}{4}m_vI_{cira}\sin(3\omega t + \varphi_0) \qquad (33)$$

The average capacitor current of the lower arm is calculated as

$$i_{cla} = m_{la}i_{la} = \frac{1}{2}\left(1 + m_v \sin(\omega t)\right)\left[-\frac{I_{ma}}{2}\sin(\omega t + \varphi) + \frac{I_{dc}}{3} + I_{cira}\cos(2\omega t + \varphi_0)\right]$$
$$= i_{cla0} + i_{cla1} + i_{cla2} + i_{cla3}$$

(34)

where

$$i_{cla0} = \frac{1}{6}I_{dc} - \frac{1}{8}m_v I_{ma}\cos\varphi$$

(35)

$$i_{cla1} = \frac{1}{6}m_v I_{dc}\sin(\omega t) - \frac{1}{4}I_{ma}\sin(\omega t + \varphi) - \frac{1}{4}m_v I_{cira}\sin(\omega t + \varphi_0)$$

(36)

$$i_{cla2} = \frac{1}{8}m_v I_{ma}\cos(2\omega t + \varphi) + \frac{1}{2}I_{cira}\cos(2\omega t + \varphi_0)$$

(37)

$$i_{cla3} = \frac{1}{4}m_v I_{cira}\sin(3\omega t + \varphi_0)$$

(38)

By neglecting the losses in the converter, the AC active power must be equal to the DC active power and it is shown by

$$P = P_{ac} = P_{dc}$$
$$\Leftrightarrow 3V_s I_s \cos\varphi = V_{dc}I_{dc}$$
$$\Leftrightarrow I_{dc} = \frac{3\sqrt{2}m_v I_s \cos\varphi}{4}$$

(39)

where I_s is the RMS value of the output current.

Comparing (30) and (35), the DC component in (29) is equal to the DC component in (34). Substituting (39) into (30), we get

$$i_{cua0} = i_{cla0} = \frac{1}{6}\left[\frac{3\sqrt{2}m_v I_s \cos\varphi}{4}\right] - \frac{1}{8}m_v I_{ma}\cos\varphi = 0$$

(40)

The DC component in the average capacitor currents of the upper and lower arms is zero. The capacitor voltage is the sum of all the harmonic components which are calculated by multiplying the nth harmonic current component with the corresponding capacitive reactance ($Z_{cn} = 1/(jn\omega C)$, $n = 1, 2, 3$). The capacitor voltage of the upper arm is expressed as

$$v_{cua} = i_{cua1} \frac{1}{j\omega C} + i_{cua2} \frac{1}{j2\omega C} + i_{cua3} \frac{1}{j3\omega C}$$
$$= v_{cua1} + v_{cua2} + v_{cua3}$$
(41)

where

$$v_{cua1} = \frac{m_v I_{dc}}{6\omega C} \cos(\omega t) - \frac{I_{ma}}{4\omega C} \cos(\omega t + \varphi) - \frac{m_v I_{cira}}{4\omega C} \cos(\omega t + \varphi_0)$$
(42)

$$v_{cua2} = \frac{m_v I_{ma}}{16\omega C} \sin(2\omega t + \varphi) + \frac{I_{cira}}{4\omega C} \sin(2\omega t + \varphi_0)$$
(43)

$$v_{cua3} = \frac{m_v I_{cira}}{12\omega C} \cos(3\omega t + \varphi_0)$$
(44)

The capacitor voltage of the lower arm is expressed as

$$v_{cla} = i_{cla1} \frac{1}{j\omega C} + i_{cla2} \frac{1}{j2\omega C} + i_{cla3} \frac{1}{j3\omega C}$$
$$= v_{cla1} + v_{cla2} + v_{cla3}$$
(45)

where

$$v_{cla1} = -\frac{m_v I_{dc}}{6\omega C} \cos(\omega t) + \frac{I_{ma}}{4\omega C} \cos(\omega t + \varphi) + \frac{m_v I_{cira}}{4\omega C} \cos(\omega t + \varphi_0)$$
(46)

$$v_{cla2} = \frac{m_v I_{ma}}{16\omega C} \sin(2\omega t + \varphi) + \frac{I_{cira}}{4\omega C} \sin(2\omega t + \varphi_0)$$
(47)

$$v_{cla3} = -\frac{m_v I_{cira}}{12\omega C} \cos(3\omega t + \varphi_0)$$
(48)

The output voltage of the SM in the upper and lower arms can be calculated by considering the insertion indices as

$$v_{SMua} = m_{ua} v_{cua} = \frac{1}{2}(1 - m_v \sin(\omega t))(v_{cua1} + v_{cua2} + v_{cua3})$$
$$= v_{SMua1} + v_{SMua2} + v_{SMua3}$$
(49)

$$v_{SMla} = m_{la} v_{cla} = \frac{1}{2}(1 + m_v \sin(\omega t))(v_{cla1} + v_{cla2} + v_{cla3})$$
$$= v_{SMla1} + v_{SMla2} + v_{SMla3}$$
(50)

where

$$v_{SMua1} = \frac{1}{2}\left(1 - m_v \sin(\omega t)\right)v_{cua1}$$

$$= -\frac{m_v I_{ma}}{16\omega C}\sin\varphi - \frac{m_v^2 I_{cira}}{16\omega C}\sin\varphi_0 + \frac{m_v I_{dc}}{12\omega C}\cos(\omega t) - \frac{I_{ma}}{8\omega C}\cos(\omega t + \varphi) - \frac{m_v I_{cira}}{8\omega C}\cos(\omega t + \varphi_0)$$

$$- \frac{m_v^2 I_{dc}}{24\omega C}\sin(2\omega t) + \frac{m_v I_{ma}}{16\omega C}\sin(2\omega t + \varphi) + \frac{m_v^2 I_{cira}}{16\omega C}\sin(2\omega t + \varphi_0)$$

$$(51)$$

$$v_{SMla1} = \frac{1}{2}\left(1 + m_v \sin(\omega t)\right)v_{cla1}$$

$$= -\frac{m_v I_{ma}}{16\omega C}\sin\varphi - \frac{m_v^2 I_{cira}}{16\omega C}\sin\varphi_0 - \frac{m_v I_{dc}}{12\omega C}\cos(\omega t) + \frac{I_{ma}}{8\omega C}\cos(\omega t + \varphi) + \frac{m_v I_{cira}}{8\omega C}\cos(\omega t + \varphi_0)$$

$$- \frac{m_v^2 I_{dc}}{24\omega C}\sin(2\omega t) + \frac{m_v I_{ma}}{16\omega C}\sin(2\omega t + \varphi) + \frac{m_v^2 I_{cira}}{16\omega C}\sin(2\omega t + \varphi_0)$$

$$(52)$$

$$v_{SMua2} = \frac{1}{2}\left(1 - m_v \sin(\omega t)\right)v_{cua2}$$

$$= -\frac{m_v^2 I_{ma}}{64\omega C}\cos(\omega t + \varphi) - \frac{m_v I_{cira}}{16\omega C}\cos(\omega t + \varphi_0) + \frac{m_v I_{ma}}{32\omega C}\sin(2\omega t + \varphi) + \frac{I_{cira}}{8\omega C}\sin(2\omega t + \varphi_0) \quad (53)$$

$$+ \frac{m_v^2 I_{ma}}{64\omega C}\cos(3\omega t + \varphi) + \frac{m_v I_{cira}}{16\omega C}\cos(3\omega t + \varphi_0)$$

$$v_{SMla2} = \frac{1}{2}\left(1 + m_v \sin(\omega t)\right)v_{cla2}$$

$$= \frac{m_v^2 I_{ma}}{64\omega C}\cos(\omega t + \varphi) + \frac{m_v I_{cira}}{16\omega C}\cos(\omega t + \varphi_0) + \frac{m_v I_{ma}}{32\omega C}\sin(2\omega t + \varphi) + \frac{I_{cira}}{8\omega C}\sin(2\omega t + \varphi_0) \quad (54)$$

$$- \frac{m_v^2 I_{ma}}{64\omega C}\cos(3\omega t + \varphi) - \frac{m_v I_{cira}}{16\omega C}\cos(3\omega t + \varphi_0)$$

$$v_{SMua3} = \frac{1}{2}\left(1 - m_v \sin(\omega t)\right)v_{cua3}$$

$$= \frac{m_v^2 I_{cira}}{48\omega C}\sin(2\omega t + \varphi_0) + \frac{m_v I_{cira}}{24\omega C}\cos(3\omega t + \varphi_0) - \frac{m_v^2 I_{cira}}{48\omega C}\sin(4\omega t + \varphi_0)$$

$$(55)$$

$$v_{SMla3} = \frac{1}{2}\left(1 + m_v \sin(\omega t)\right)v_{cla3}$$

$$= \frac{m_v^2 I_{cira}}{48\omega C}\sin(2\omega t + \varphi_0) - \frac{m_v I_{cira}}{24\omega C}\cos(3\omega t + \varphi_0) - \frac{m_v^2 I_{cira}}{48\omega C}\sin(4\omega t + \varphi_0)$$

$$(56)$$

If the MMC has N SMs per arm, the total voltage of all SMs in a phase unit will be given by

$$v_{pha} = Nv_{SMua} + Nv_{SMla}$$
$$= v_{pha1} + v_{pha2} + v_{pha3} \tag{57}$$

where

$$v_{pha1} = -\frac{Nm_v I_{ma}}{8\omega C}\sin\varphi - \frac{Nm_v^2 I_{cira}}{8\omega C}\sin\varphi_0 \tag{58}$$

$$v_{pha2} = -\frac{Nm_v^2 I_{dc}}{12\omega C}\sin(2\omega t) + \frac{3Nm_v I_{ma}}{16\omega C}\sin(2\omega t + \varphi)$$
$$+ \frac{Nm_v^2 I_{cira}}{6\omega C}\sin(2\omega t + \varphi_0) + \frac{NI_{cira}}{4\omega C}\sin(2\omega t + \varphi_0) \tag{59}$$

$$v_{pha3} = -\frac{Nm_v^2 I_{cira}}{24\omega C}\sin(4\omega t + \varphi_0) \tag{60}$$

The total voltage of all SMs in a phase unit contains a DC component, second- and fourth-order harmonic components. These harmonic components can cause the circulating currents in arms with the corresponding frequencies. As mentioned before, the significant harmonic component in the circulating current is the second-order harmonic component. Thus, the fourth-order harmonic component in (57) can be neglected. The total voltage in phase unit B and C can be calculated in a similar way. However, there is a phase shift of $2\pi/3$ between two adjacent phases in the negative sequence. From the above analysis, the equivalent circuit of the circulating currents is formed in Fig. 21.

The purpose of using arm inductors is to make the DC-link voltage constant or eliminate the circulating currents. The voltage drop on the inductance of $2L_0$ as shown in Fig. 21 has the same amplitude with the v_{pha2}, but it has opposite direction. Thus, the circulating current can be calculated as
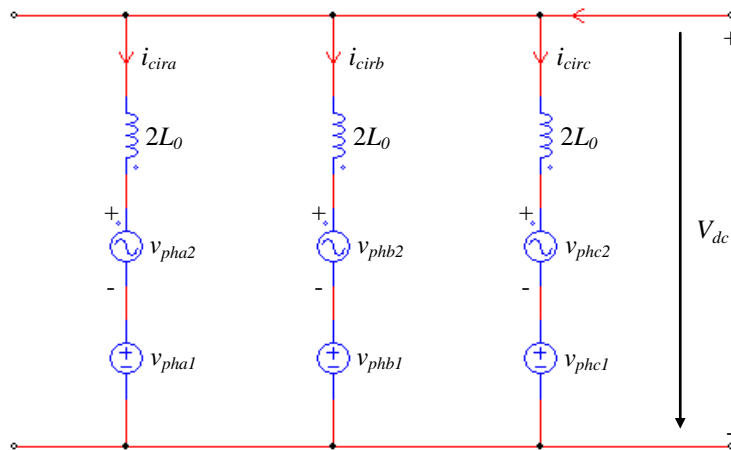

Fig. 21 Equivalent circuit of the circulating currents

$$i_{cira} = -\frac{v_{pha2}}{j4\omega L_0} \tag{61}$$

Substituting the sinusoidal form of the circulating current and (59) into (61), we can obtain

$$
\begin{aligned}
I_{cira}\cos(2\omega t + \varphi_0) = &-\frac{Nm_v^2 I_{dc}}{48\omega^2 L_0 C}\cos(2\omega t) + \frac{3Nm_v I_{ma}}{64\omega^2 L_0 C}\cos(2\omega t + \varphi) \\
&+ \frac{Nm_v^2 I_{cira}}{24\omega^2 L_0 C}\cos(2\omega t + \varphi_0) + \frac{NI_{cira}}{16\omega^2 L_0 C}\cos(2\omega t + \varphi_0)
\end{aligned} \tag{62}
$$

By solving (62), the amplitude of the circulating current will be achieved as

$$I_{cira} = \frac{\sqrt{\left(\dfrac{3}{64}Nm_v I_{ma}\cos\varphi - \dfrac{1}{48}Nm_v^2 I_{dc}\right)^2 + \left(\dfrac{3}{64}Nm_v I_{ma}\sin\varphi\right)^2}}{\omega^2 L_0 C - \dfrac{Nm_v^2}{24} - \dfrac{N}{16}} \tag{63}$$

Finally, the arm inductance can be derived from (63) with a certain value of the circulating current as given by

$$L_0 = \frac{1}{\omega^2 C}\left[\frac{\sqrt{\left(\dfrac{3}{64}Nm_v I_{ma}\cos\varphi - \dfrac{1}{48}Nm_v^2 I_{dc}\right)^2 + \left(\dfrac{3}{64}Nm_v I_{ma}\sin\varphi\right)^2}}{I_{cira}} + \frac{Nm_v^2}{24} + \frac{N}{16}\right] \tag{64}$$

A simulation will be set up to verify the calculating value of the arm inductor in (64). The parameters of the MMC are shown in Table 1.

The relationship between the circulating current and the arm inductance is shown in Fig. 22. It can be seen that the calculation result by using (64) and simulation result are almost similar. The error between two results is very small. The circulating current is reduced with the increase of the arm inductance. With small values of the arm inductor, the circulating current is significantly changed. However, the circulating current only has a small change to the larger values of the arm inductor. This characteristic is an important principle to select the size of the arm inductor for the MMC. The arm inductance is not too small to avoid the high circulating current, but it shouldn't be also too large to avoid the voltage drop and losses.

Table 1. Parameters of the MMC

Quantity	Value
Rated active power	20 MW
Power factor	1
AC voltage	22.9 kV
Nominal frequency	60 Hz
Transformer ratio	22.9 kV/11 kV
DC-link voltage	±10 kV
Number of SMs per arm	20
SM capacitance	14000 μF

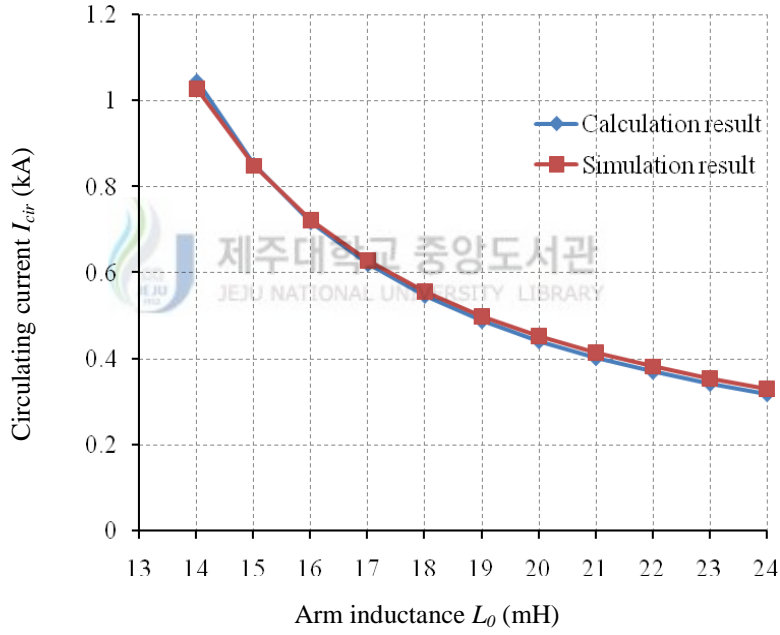Fig. 22 Relationship between the circulating current and the arm inductance

2.5.2 Submodule capacitance

By neglecting the effect of the circulating currents, the upper arm voltage and current of phase A can be rewritten as [4]

$$v_{ua} = \frac{V_{dc}}{2} - e_a = \frac{1}{2}V_{dc}(1 - m_v \sin \omega t) \tag{65}$$

$$i_{ua} = \frac{i_a}{2} + i_{diffa} = \frac{1}{3}I_{dc}[1 + m_i \sin(\omega t + \varphi)] \tag{66}$$

31

where
$$m_i = \frac{3I_{ma}}{2I_{dc}} \tag{67}$$

The instantaneous power of the upper arm is given by

$$p_{ua} = v_{ua}i_{ua} = \frac{1}{6}V_{dc}I_{dc}(1 - m_v \sin \omega t)(1 + m_i \sin(\omega t + \varphi)) \tag{68}$$

The energy of the upper arm is calculated by integrating the instantaneous power between two zero crossings as

$$W_{ua} = \int_{x_1}^{x_2} p_{ua}dt = \int_{x_1}^{x_2} \left[\frac{1}{6}V_{dc}I_{dc}(1 - m_v \sin \omega t)(1 + m_i \sin(\omega t + \varphi)) \right]dt \tag{69}$$

where x_1 and x_2 are the points that the instantaneous power is zero in every half period.

Solving the (69), we get the equation for calculating the energy of the upper arm.

$$W_{ua} = \frac{2}{3} \frac{S}{m_v \omega} \left[1 - \left(\frac{m_v \cos \varphi}{2} \right)^2 \right]^{3/2} \tag{70}$$

where S is the apparent power of the converter, it is determined by

$$S = \frac{P}{\cos \varphi} = \frac{Q}{\sin \varphi} \tag{71}$$

If the MMC has N SMs in each arm, the energy which stores in each SM can be expressed by

$$W_{SMa} = \frac{2}{3} \frac{S}{Nm_v \omega} \left[1 - \left(\frac{m_v \cos \varphi}{2} \right)^2 \right]^{3/2} \tag{72}$$

Because the SM capacitor is charged or discharged depending on the direction of the arm current, thus the capacitor voltage will oscillate around its nominal value. The ripple of the capacitor voltage in this case is typical by a range of $\pm\varepsilon$. The following relation can be achieved as

$$V_c(1 - \varepsilon) \le v_c \le V_c(1 + \varepsilon) \tag{73}$$

The energy of the SM capacitor is given by

$$W_{Ca} = \frac{1}{2} C V_c^2 \tag{74}$$

Using (72) and (74), we can obtain

$$W_{Ca} = \frac{1}{4\varepsilon} W_{SMa} \Leftrightarrow \frac{1}{2} C V_c^2 = \frac{1}{4\varepsilon} \frac{2}{3} \frac{S}{N m_v \omega} \left[1 - \left(\frac{m_v \cos\varphi}{2} \right)^2 \right]^{3/2} \tag{75}$$

Finally, the capacitance of the SM will be calculated as follows.

$$C = \frac{S}{3 N m_v \omega \varepsilon V_c^2} \left[1 - \left(\frac{m_v \cos\varphi}{2} \right)^2 \right]^{3/2} \tag{76}$$

By using the parameters of the MMC in Table 1, the calculation capacitance of the SM capacitor is about 14000 μF. The ripple of the capacitor voltage ε is selected about 5% of the average capacitor voltage. The waveform of the capacitor voltage is shown in Fig. 23.

It can be seen in Fig. 23 that the average capacitor voltage is 1 kV. With the calculating value of the SM capacitor, the capacitor voltage oscillates around its average value. The ripple of the capacitor voltage meets the initial standard design. It is about ±0.05 kV or 5%. This demonstrates that the calculation method of the SM capacitor is quite correct.
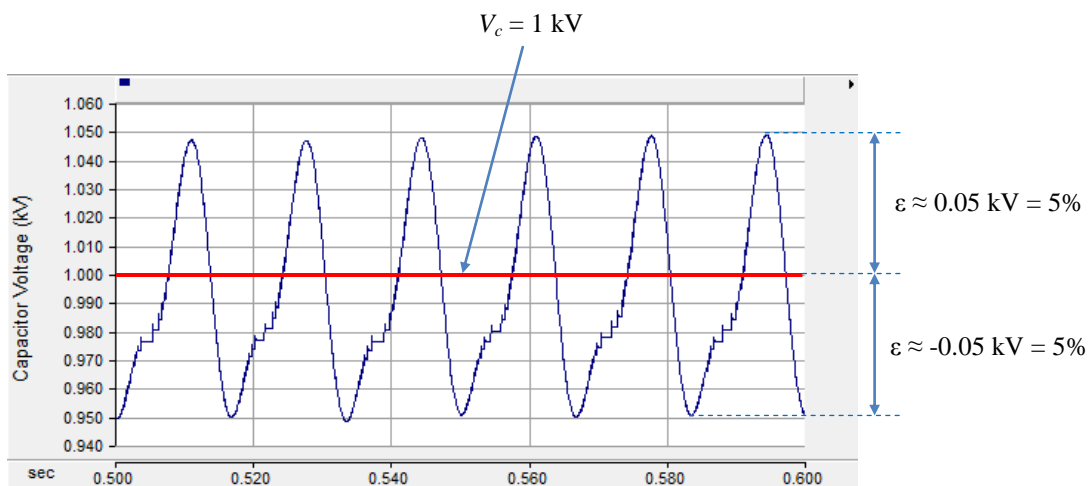

Fig. 23 Waveform of the capacitor voltage

Chapter 3. Control of the MMC-HVDC System

3.1 Control of the MMC-HVDC system under normal operating conditions

The first step to design the controller of the MMC-HVDC system is the transformation of the three-phase voltage and current to DC quantities or the synchronous rotating reference frame (dq-frame). This is done by using the Park's transformation as [39]

$$
\begin{bmatrix} v_{sd} \\ v_{sq} \\ v_{s0} \end{bmatrix} = [T_{dq}] \begin{bmatrix} v_{sa} \\ v_{sb} \\ v_{sc} \end{bmatrix} = \frac{2}{3} \begin{bmatrix} \cos\theta & \cos(\theta-120) & \cos(\theta+120) \\ \sin\theta & \sin(\theta-120) & \sin(\theta+120) \\ \frac{1}{2} & \frac{1}{2} & \frac{1}{2} \end{bmatrix} \begin{bmatrix} v_{sa} \\ v_{sb} \\ v_{sc} \end{bmatrix} \tag{77}
$$

where v_{sa}, v_{sb}, v_{sc} are the three-phase voltage. v_{sd}, v_{sq}, v_{s0} are the d-axis, q-axis, and 0-components in the dq-frame.

If three-phase voltage is balanced, the d- and q-axis components will be DC quantities while the 0-component will be zero. The signals in the dq-frame are suitable for control with a standard PI controller. Moreover, the calculation of the voltage, current, and power is also more simple. To transform from the dq-frame to the three-phase frame, an inverse transformation is used as [39]

$$
\begin{bmatrix} v_{sa} \\ v_{sb} \\ v_{sc} \end{bmatrix} = [T_{dq}^{-1}] \begin{bmatrix} v_{sd} \\ v_{sq} \\ v_{s0} \end{bmatrix} = \begin{bmatrix} \cos\theta & \sin\theta & 1 \\ \cos(\theta-120) & \sin(\theta-120) & 1 \\ \cos(\theta+120) & \sin(\theta+120) & 1 \end{bmatrix} \begin{bmatrix} v_{sd} \\ v_{sq} \\ v_{s0} \end{bmatrix} \tag{78}
$$

The (77) and (78) represent for the three-phase voltage. The transformations of the three-phase current will be done in a similar way.

The problem is how to achieve the theta (θ) angle. In general, the theta angle is achieved by using the phase-locked loop (PLL) control as shown in Fig. 24 [39]. The input voltage is first transformed to the dq-frame by using the Park's transformation. The angular position of this dq-frame is controlled by a feedback loop that regulates the v_{sd} to zero. The steady-state error is enforced to zero by using a PI controller. To obtain the estimated frequency ω, $\Delta\omega$ is added to the initial value ω_{set} that helps to get a faster start-up. The theta angle can be achieved by integrating ω and using the modulators. Depending on the users, the theta angle

can be in range of ($-\pi$, π) or (0, 2π).

The circuit diagram of the MMC-HVDC system is shown in Fig. 25 [18], [40]. It comprises two MMCs connected in back-to-back together. Because the MMC-HVDC system is a type of the VSC-HVDC system, the control structure for the MMC-HVDC system will be the cascade vector control that consists of a fast inner current control loop and outer control loops. Depending on the applications, the outer control loops can be the DC-link voltage control, AC voltage control, the active and reactive power controls. If the MMC-1 is used to control the active and reactive powers, the MMC-2 will be responsible for controlling the DC-link voltage and the reactive power, and vice versa. The control of the AC voltage can be performed in one converter or both converters.
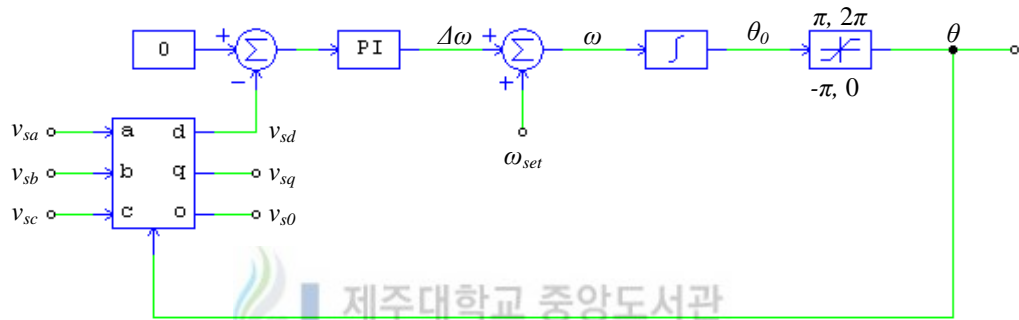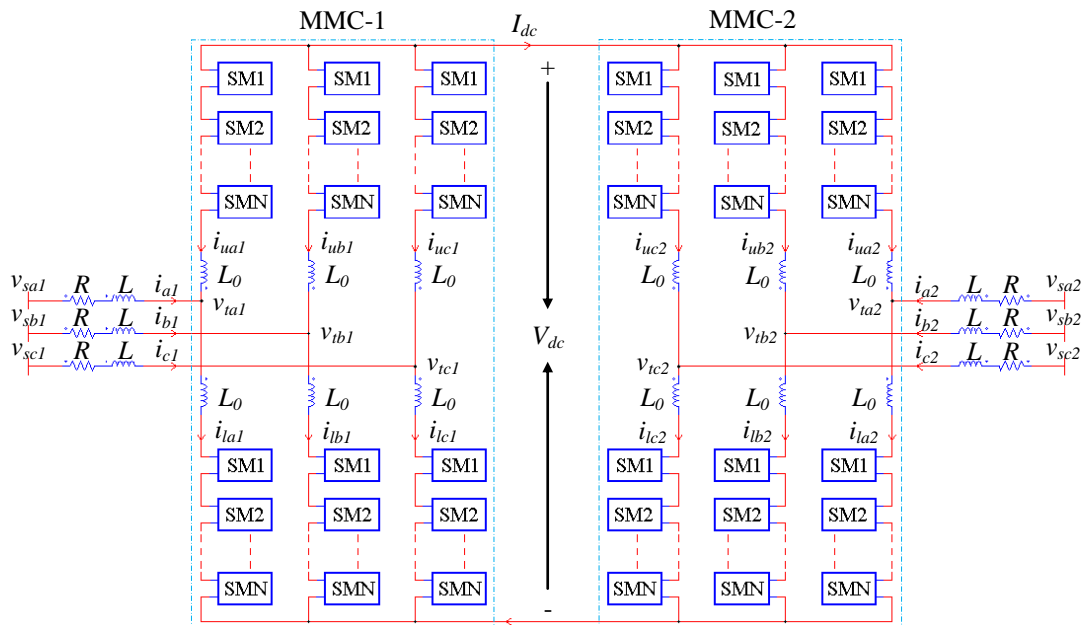

Fig. 24 Phase-locked loop control

Fig. 25 Circuit diagram of the MMC-HVDC system

3.1.1 Current control

The current controller is responsible for tracking the current to the reference value. From Fig. 25, the AC voltage of the MMC-HVDC system is expressed by

$$v_{sj\_k} = Ri_{j\_k} + L\frac{di_{j\_k}}{dt} + v_{tj\_k} \tag{79}$$

where j represents for the three-phase component of the voltage and current, $j = a,\ b,\ c.\ k$ denotes the MMC-1 and MMC-2, $k = 1,\ 2.\ v_{sj\_k},\ v_{tj\_k}$ and i_{j_k} are the three-phase voltage and current of the MMC-k. R and L are the resistance and inductance of the system, respectively.

By using the Park's transformation, the AC voltage can be rewritten in the dq-frame as

$$v_{sd\_k} = Ri_{d\_k} + L\frac{di_{d\_k}}{dt} + v_{td\_k} - \omega Li_{q\_k} \tag{80}$$

$$v_{sq\_k} = Ri_{q\_k} + L\frac{di_{q\_k}}{dt} + v_{tq\_k} + \omega Li_{d\_k} \tag{81}$$

where v_{sd_k}, v_{sq_k}, v_{td_k}, v_{tq_k}, i_{d_k} and i_{q_k} denote the dq-axis components of the three-phase voltage and current of the MMC-k.

From (80) and (81), the dq-axis components of terminal voltage can be calculated as

$$v_{td\_k} = -Ri_{d\_k} - L\frac{di_{d\_k}}{dt} + v_{sd\_k} + \omega Li_{q\_k} \tag{82}$$

$$v_{tq\_k} = -Ri_{q\_k} - L\frac{di_{q\_k}}{dt} + v_{sq\_k} - \omega Li_{d\_k} \tag{83}$$

The terminal voltage will depend on the AC current. If the PI controller is used, the current controllers will be described as

$$v_{td\_k}^* = -\left(K_p + \frac{K_i}{s}\right)\left(i_{d\_k}^* - i_{d\_k}\right) + v_{sd\_k} + \omega Li_{q\_k} \tag{84}$$

$$v_{tq\_k}^* = -\left(K_p + \frac{K_i}{s}\right)\left(i_{q\_k}^* - i_{q\_k}\right) + v_{sq\_k} - \omega Li_{d\_k} \tag{85}$$

where superscript * represents for the reference value of the signal.

By using the Laplace transform, the (80) and (81) can be represented as transfer functions.

$$v_{sd\_k} = Ri_{d\_k} + sLi_{d\_k} + v^*_{td\_k} - \omega Li_{q\_k}$$

$$\Leftrightarrow i_{d\_k} = \frac{1}{R + sL}\left(v_{sd\_k} - v^*_{td\_k} + \omega Li_{q\_k}\right) \qquad (86)$$

$$v_{sq\_k} = Ri_{q\_k} + sLi_{q\_k} + v^*_{tq\_k} + \omega Li_{d\_k}$$

$$\Leftrightarrow i_{q\_k} = \frac{1}{R + sL}\left(v_{sq\_k} - v^*_{tq\_k} - \omega Li_{d\_k}\right) \qquad (87)$$

The control diagram of the current is shown in Fig. 26. The PI controller will track the current to its reference value. The current decoupling and voltage feed-forward terms are added to improve the response of the controller.

3.1.2 DC-link voltage control

From Fig. 25, if the losses in the MMC are neglected, the power balance equation of the MMC-HVDC system can be expressed by [40]

$$P_{dc} = -\left(P_1 + P_2\right) \qquad (88)$$

where P_{dc} is the power of the MMC-HVDC system at the DC side. It is calculated as
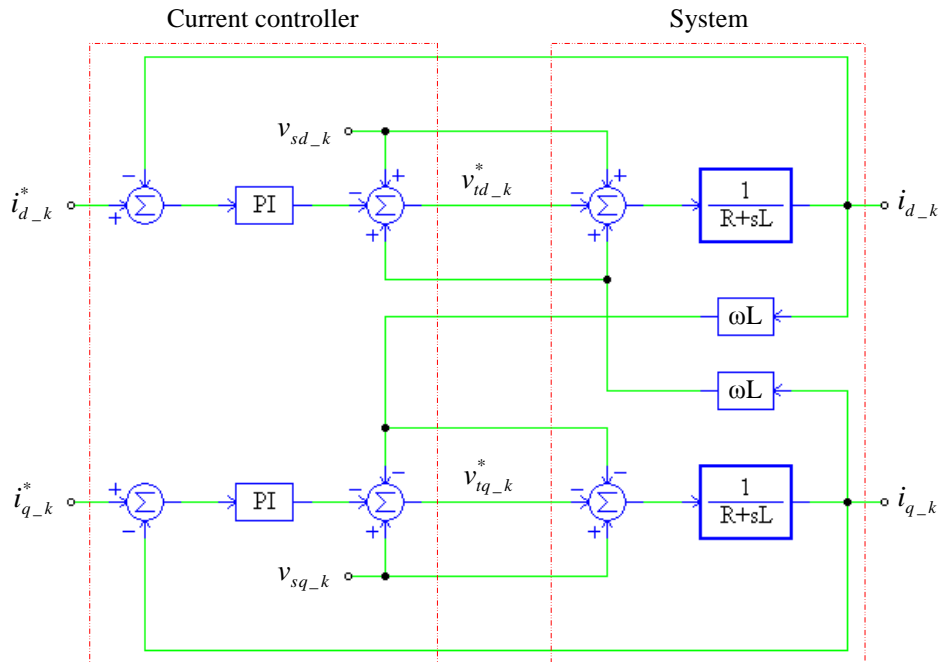
Fig. 26 Control diagram of the current

$$P_{dc} = V_{dc}I_{dc} = \frac{C_{eq}}{2}\frac{dV_{dc}^2}{dt} \tag{89}$$

where C_{eq} is the equivalent capacitance of two MMC units. P_1 and P_2 are the active powers of the MMC-1 and MMC-2. These powers can be calculated by

$$P_1 = \frac{3}{2}\left(v_{sd\_1}i_{d\_1} + v_{sq\_1}i_{q\_1}\right) \tag{90}$$

$$P_2 = \frac{3}{2}\left(v_{sd\_2}i_{d\_2} + v_{sq\_2}i_{q\_2}\right) \tag{91}$$

Substituting (89)-(91) to (88), we get

$$\frac{C_{eq}}{2}\frac{dV_{dc}^2}{dt} = -\left[\frac{3}{2}\left(v_{sd\_1}i_{d\_1} + v_{sq\_1}i_{q\_1}\right) + \frac{3}{2}\left(v_{sd\_2}i_{d\_2} + v_{sq\_2}i_{q\_2}\right)\right] \tag{92}$$

By using the voltage oriented vector control, the d-axis voltage component will be zero. The AC voltages at both MMC sides are assumed to be the same in amplitude ($v_{sq\_1} = v_{sq\_2}$). Hence, the (92) is rewritten as

제주대학교 중앙도서관

$$\frac{C_{eq}}{2}\frac{dV_{dc}^2}{dt} = -\frac{3}{2}v_{sq\_1}\left(i_{q\_1} + i_{q\_2}\right) \tag{93}$$

The q-axis reference currents $i_{q\_1}^*$ and $i_{q\_2}^*$ are defined as [18], [40]

$$i_{q\_1}^* = -i_P^* + i_{Vdc}^* \tag{94}$$

$$i_{q\_2}^* = i_P^* + i_{Vdc}^* \tag{95}$$

where i_P^* is the current corresponding to the pre-specified real power exchange between the AC system-1 and AC system-2. i_{Vdc}^* is a small real current to regulate the net DC-link voltage.

The response of the current controllers (85) to the references (94) and (95) is expressed by

$$i_{q\_1} = -i_P + i_{Vdc} \tag{96}$$

$$i_{q\_2} = i_P + i_{Vdc} \tag{97}$$

Substituting (96) and (97) into (93) and rearranging, we obtain

38

$$\frac{dV_{dc}^2}{dt} = -\frac{6v_{sq\_1}}{C_{eq}} i_{Vdc} \tag{98}$$

The DC-link voltage controller can be derived from (98) as

$$i_{Vdc}^* = \left(K_p + \frac{K_i}{s} \right) \left(V_{dc}^{*2} - V_{dc}^2 \right) \tag{99}$$

Considering V_{dc}^2 as a state variable, the (98) can be rewritten in the Laplace domain as

$$V_{dc}^2 = -\frac{6v_{sq\_1}}{sC_{eq}} i_{Vdc} \tag{100}$$

The (100) describes the relationship between the DC-link voltage and the current command. If the MMC-1 is used to control the DC-link voltage, the control diagram of the DC-link voltage will be shown in Fig. 27.

3.1.3 Active and reactive power controls

The active and reactive powers of the MMC-HVDC system can be calculated by [18], [39], [40]

$$P_k = \frac{3}{2} \left(v_{sq\_k} i_{q\_k} \right) \approx \frac{3}{2} \left(v_{sq\_k} i_P \right) \tag{101}$$

$$Q_k = -\frac{3}{2} \left(v_{sq\_k} i_{d\_k} \right) \tag{102}$$

where P_k and Q_k are the active and reactive powers of the MMC-k.

In order to monitor the output powers of the converter system, the closed-loop control is
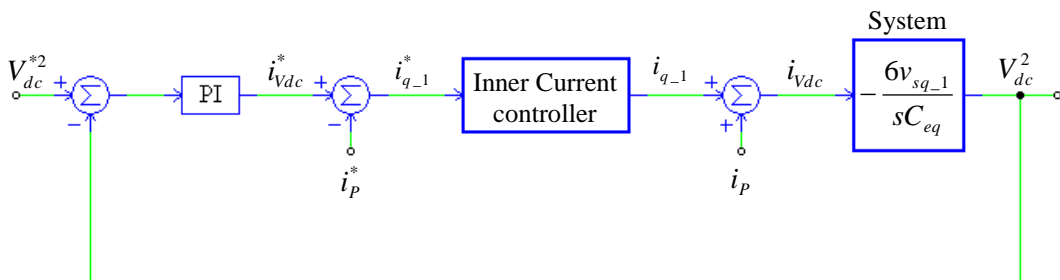
Fig. 27 Control diagram of the DC-link voltage

39

applied for the power controllers. Therefore, the reference currents are expressed from (101) and (102) as

$$i_P^* = \left(K_p + \frac{K_i}{s} \right)\left(P_k^* - P_k \right) \tag{103}$$

$$i_{d\_k}^* = \left(K_p + \frac{K_i}{s} \right)\left(Q_k^* - Q_k \right) \tag{104}$$

3.1.4 AC voltage control

To support for the grid voltage, an AC voltage controller is implemented in the MMC-*k* control. From Fig. 25, the voltage drop over the reactance *RL* is expressed by [41]

$$\begin{aligned} \Delta v_k &= v_{s\_k} - v_{t\_k} \\ &= \frac{RP_k + XQ_k}{v_{s\_k}} + j\,\frac{XP_k - RQ_k}{v_{s\_k}} \end{aligned} \tag{105}$$

The imaginary part in (105) is very small in comparing to the real part, and almost power systems satisfy with $X \gg R$. Thus, the voltage drop can be rearranged as

$$Q_k \approx \frac{v_{s\_k}\Delta v_k}{X} \tag{106}$$

The AC voltage is proportional to the reactive power. Then, the voltage controller can be described by

$$Q_k^* = \left(K_p + \frac{K_i}{s} \right)\left(v_{rms\_k}^* - v_{rms\_k} \right) \tag{107}$$

The output signal of the voltage controller is the reference value of the reactive power. Depending on the reference value of the voltage, the MMC-*k* will generate or consume the reactive power to or from the power system.

3.1.5 Overall control diagram of the MMC-HVDC system

From the above analysis, the overall control diagram of the MMC-HVDC system is shown in Fig. 28. The output signals of the outer control loop are the reference values for the inner

40
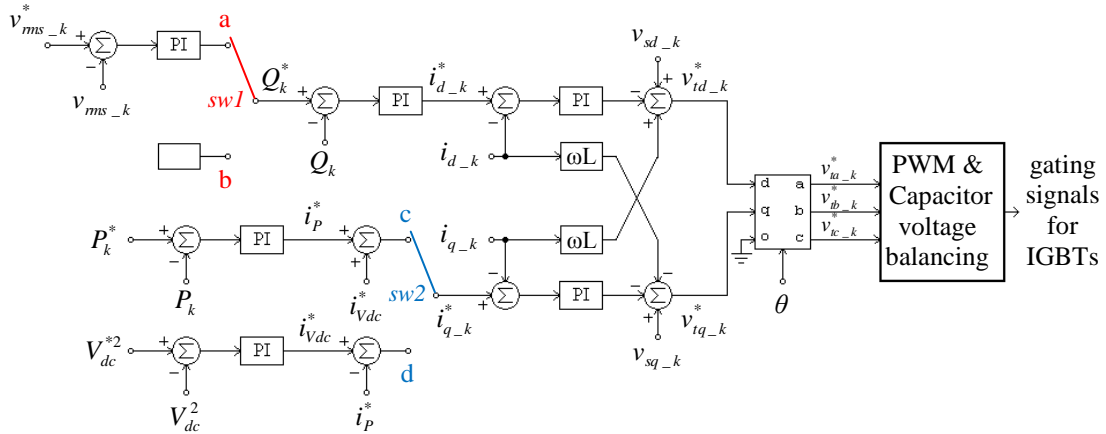
Fig. 28 Overall control diagram of the MMC-HVDC system

current control loop. The current controllers will regulate the currents to its reference values. The output signals of the inner current control loop are the reference values of the terminal voltages that are combined with the modulation methods and the capacitor voltage balancing control to generate the gating signals for the IGBTs. The operation of the "*sw1*" and "*sw2*" is as follows.

➢ *sw1* → a: The AC voltage controller is activated. The reference reactive power depends on the reference value of the AC voltage.

➢ *sw1* → b: The reference reactive power depends on the users.

➢ *sw2* → c: The MMC-*k* is used to control the active power.

➢ *sw2* → d: The MMC-*k* is used to control the DC-link voltage.

At each time, one MMC is employed to control the active power and the reactive power or the AC voltage. The other one is responsible for controlling the DC-link voltage and the reactive power or the AC voltage.

3.1.6 Normal operating cases

To depict the normal operation of the MMC-HVDC system, simulation results are performed by using the PSCAD/EMTDC simulation program. The single-line diagram of the MMC-HVDC system is shown in Fig. 29. The MMC-HVDC system plays a role as an intermediate device to exchange power between the source 1 and source 2. Parameters of the MMC-HVDC system are shown in Table 2. The capacity of the test system is 200 MW. In this simulation, the MMC-1 is used to control the DC-link voltage and the reactive power or the AC voltage. The MMC-2 is employed to control the active and reactive powers or the AC voltage. The simulation is carried out in three cases:
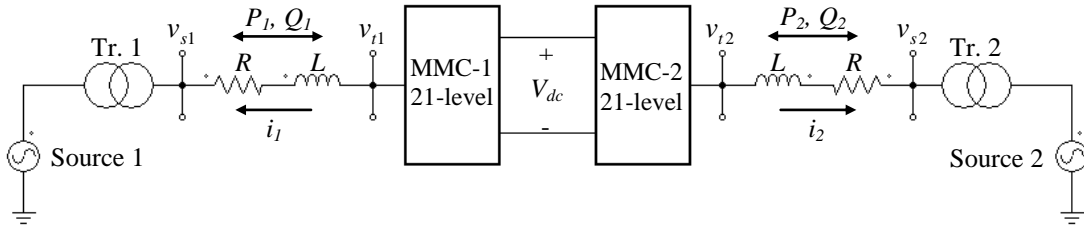
Fig. 29 Single-line diagram of the MMC-HVDC system

Table 2. Parameters of the MMC-HVDC system

Quantity	Value
Active power	200 MW
Reactive power	100 MVar
AC voltage	154 kV
Nominal frequency	60 Hz
Transformer ratio	154 kV/50 kV
DC-link voltage	±50 kV
Number of SMs per arm	20
Arm inductance	0.0035 H
SM capacitance	7800 μF

3.1.6.1 Independent control

Because the MMC-HVDC system is a type of the VSC-HVDC system, thus it can control the active and reactive powers independently. This can be achieved by using the decoupling control method. The simulation results are shown in Fig. 30. The initial condition is zero active and reactive powers in both MMCs. The DC-link voltage is controlled to its reference value. At t = 1 s, the reference active power is ramped up to 200 MW. In this case, the HVDC system is transferring the active power from the source 1 to the source 2. At t = 1.5 s, the reference reactive power of the MMC-2 is changed to 100 MVar. At = 2 s, the reference reactive power of the MMC-1 is ramped up to 50 MVar. The power controllers always ensure that the active and reactive powers will follow its reference values as shown in Fig. 30(a)-(b). The change of the active power will not affect to the reactive power and vice versa. In other words, the active and reactive powers can be controlled independently. Fig. 30(c) shows the DC-link voltage. It is almost constant during the change of the active and reactive powers. At the rated active power, the ripple of the capacitor voltages in the MMC-1 and the MMC-2 is about 4.4% of the nominal value as seen in Fig. 30(d)-(e). However, this ripple will be higher if the reactive power is ramped up. When the reactive power of the MMC-1 is

50 MVar, the ripple of the capacitor voltages is about 5.4%. When the reactive power of the MMC-2 is 100 MVar, the ripple of the capacitor voltages is about 6.6%.
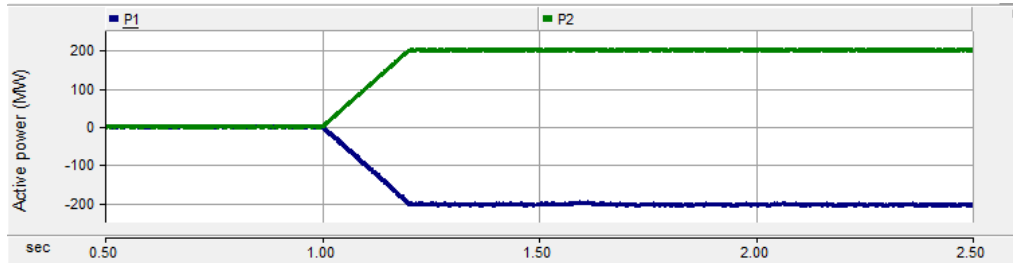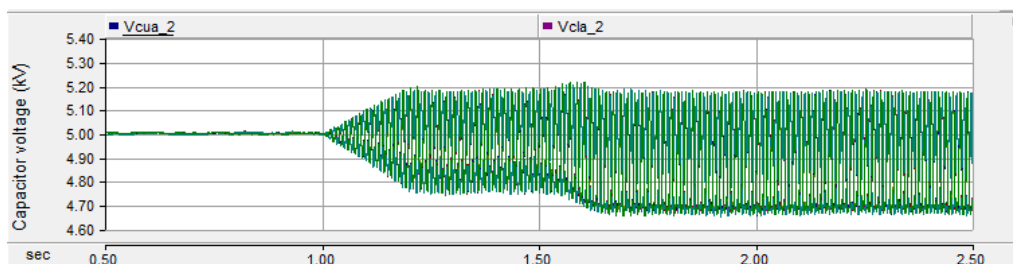

(a) Active powers
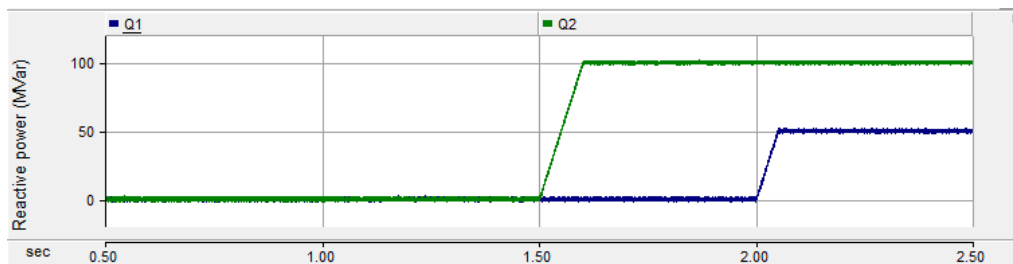
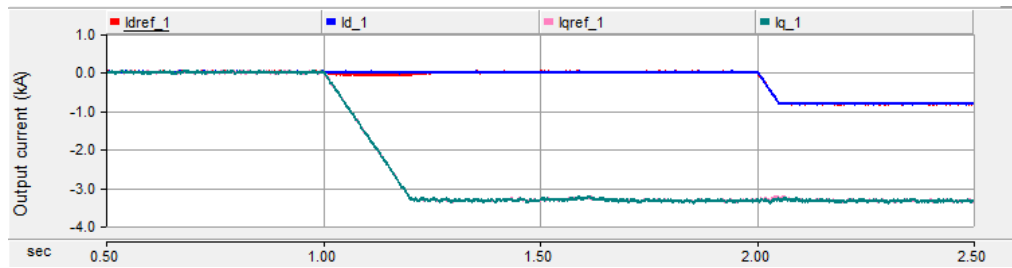
(b) Reactive powers
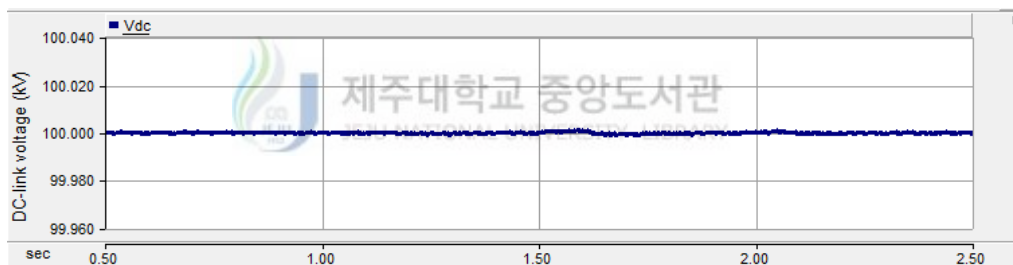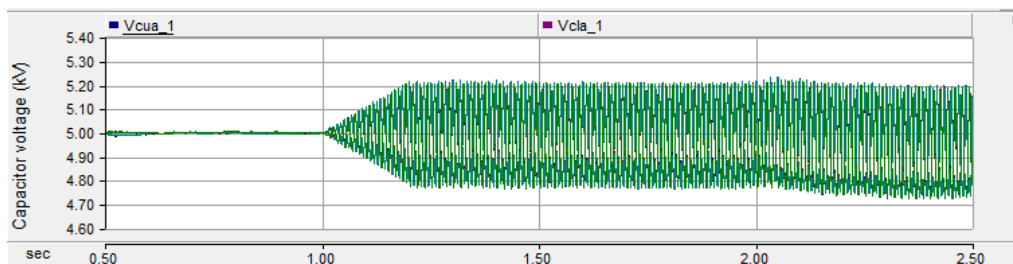
(c) DC-link voltage

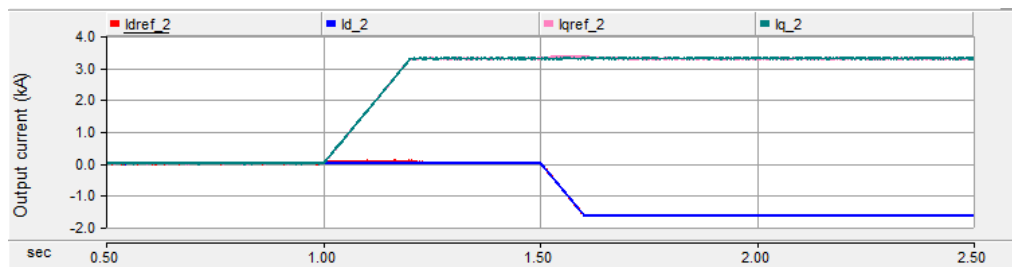(d) Capacitor voltages of the submodules in MMC-1

(e) Capacitor voltages of the submodules in MMC-2

Fig. 30 Independent control of the MMC-HVDC system

43

(a) dq-axis output currents of MMC-1 and its reference currents

(b) dq-axis output currents of MMC-2 and its reference currents

Fig. 31 Response of the current controllers

Fig. 31 shows the response of the output currents of the MMCs to its reference values. The reference currents are forced to vary due to the change of the active and reactive powers. However, the response of the current controllers is fast enough to regulate the current to the reference value.

3.1.6.2 Active power reversal control

Similar to the VSC-HVDC system, the MMC-HVDC system can also transfer the power in two directions, from the source 1 to the source 2 and vice versa. The control of the MMC-HVDC system in this case is shown in Fig. 32. At the starting time, the active power is set to 200 MW, the MMC-HVDC system is transferring the active power from the source 1 to the source 2. At t = 1 s, the active power is reversed to -200 MW, the MMC-HVDC system is transferring the active power from the source 2 to source 1 as shown in Fig. 32(a). The reactive power is set to zero in both MMCs during operation (Fig. 32(b)). Similar to the previous section, the reverse control of the active power does not affect to the control of the reactive power. The DC-link voltage is kept at its reference value during operation as depicted in Fig. 32(c). The ripple of the capacitor voltages at the steady-state is about 4.4% of the nominal value as seen in Fig. 32(d)-(e).
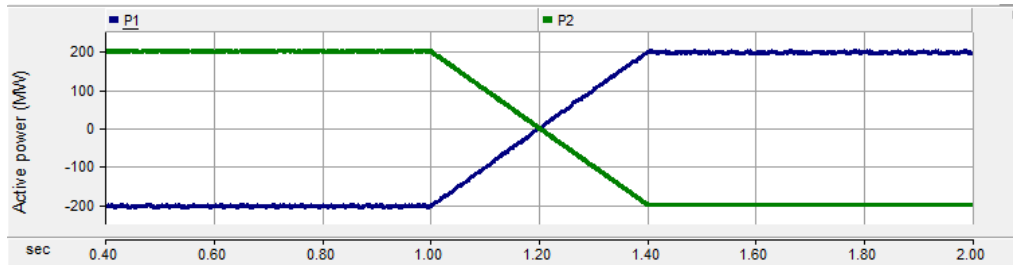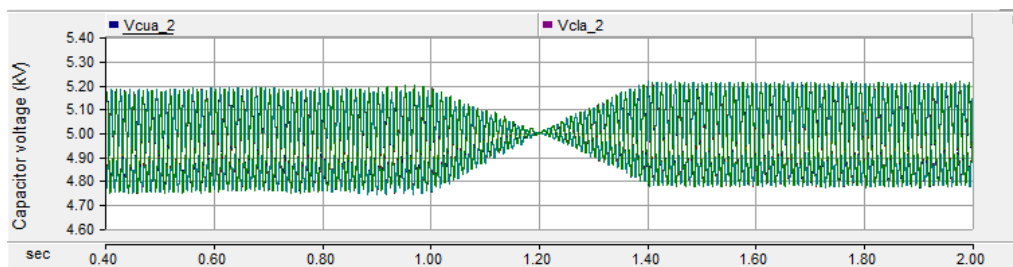
(a) Active powers
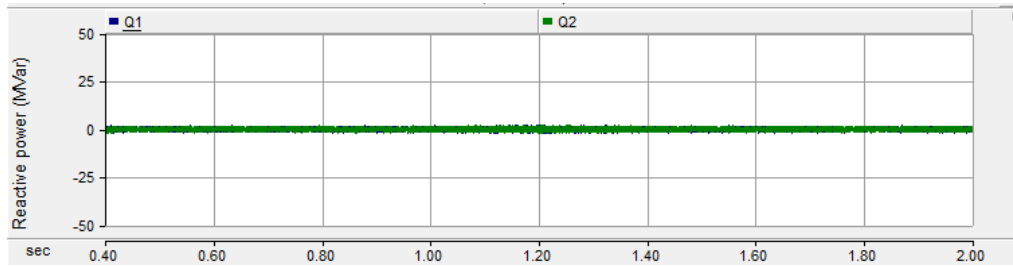
(b) Reactive powers
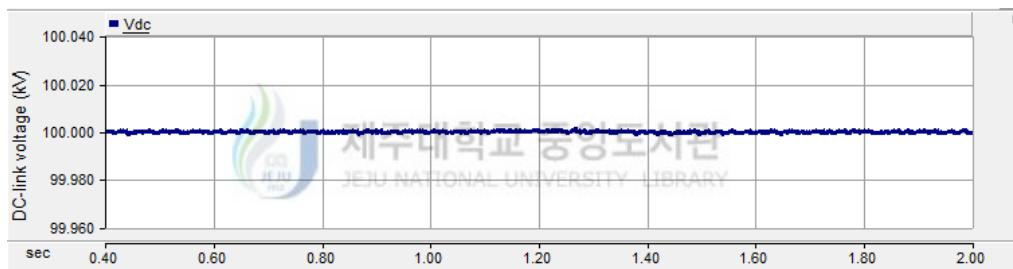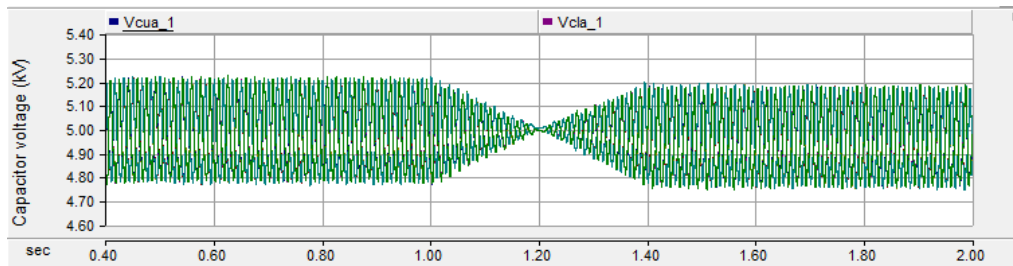
(c) DC-link voltage

(d) Capacitor voltages of the submodules in MMC-1

(e) Capacitor voltages of the submodules in MMC-1

Fig. 32 Active power reversal control of the MMC-HVDC system

3.1.6.3 AC grid voltage control

Normally, the voltage received at the point of common coupling (PCC) or the load side is dropped below the nominal value because of the losses in the transmission lines and transformers. A static synchronous compensator (Statcom) is often used to solve this problem. However, the cost of the Statcom is expensive. The MMC-HVDC system contains the capacitors at the DC side, thus it can supply the reactive power to the power grid. This means that the MMC-HVDC system can regulate the grid voltage at the position where it is connected to. In this case, the use of the Statcom is not necessary. To evaluate the operation of the MMC-HVDC system, a simulation is established based on Fig. 33. The parameters of the MMC-HVDC system are shown in Table 2.

The MMC-HVDC system is controlled to transfer 200 MW of the active power from the system 1 to the system 2 during simulation. The reactive power is set to zero in both converters at the starting time. Because of the losses in the transmission line and the transformers, the grid voltages of two systems are dropped below the nominal value as shown in Fig. 34(a). After the AC voltage controllers are activated at t = 1 s with the MMC-1 and t = 1.5 s with the MMC-2, the MMC-HVDC system supplies the reactive powers to the power grid as depicted in Fig. 34(c). As a result, the grid voltages are improved to the reference value of 154 kV. During the simulation, the DC-link voltage is almost kept at its reference value as seen in Fig. 34(d).
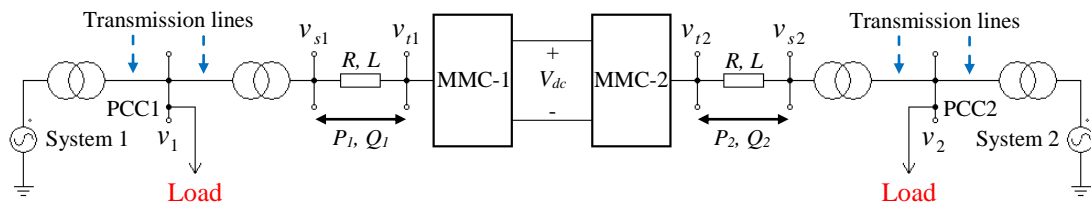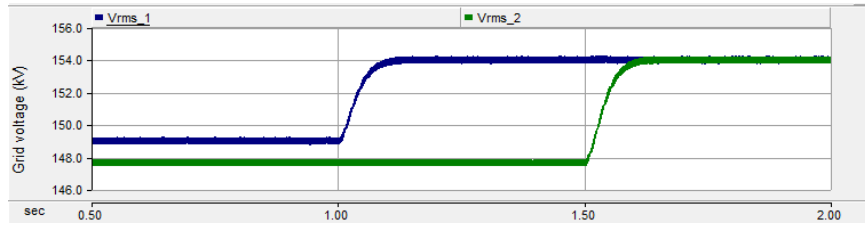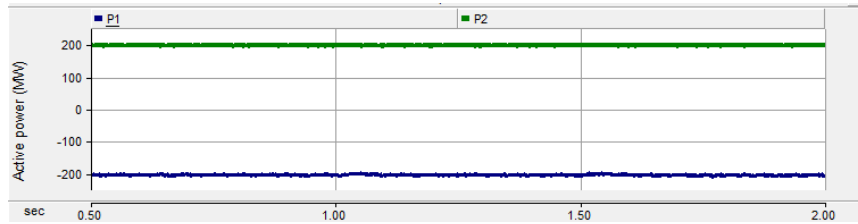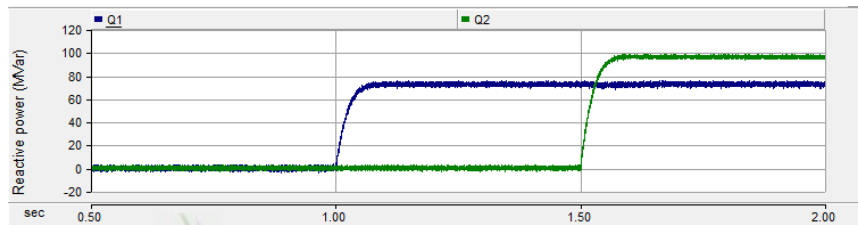

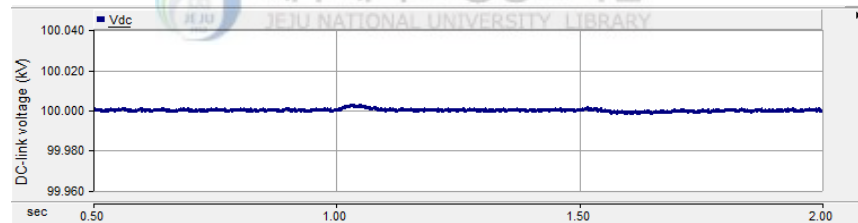Fig. 33 MMC-HVDC system in the power system

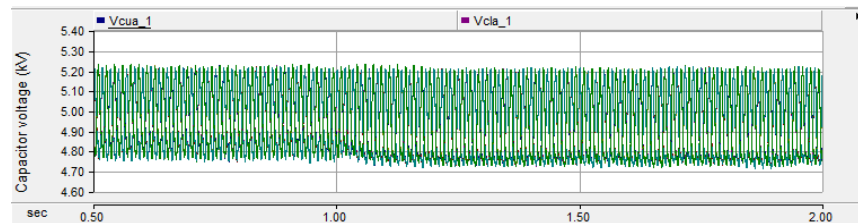(a) RMS values of the grid voltages
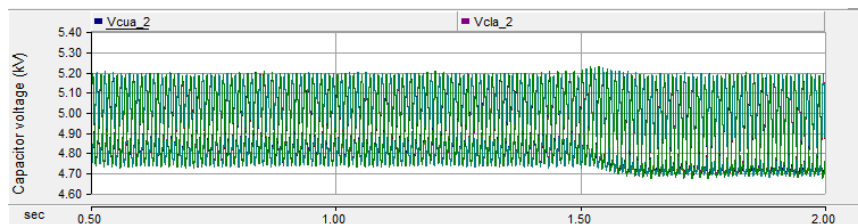

(b) Active powers

(c) Reactive powers

(d) DC-link voltage

(e) Capacitor voltages of the submodules in MMC-1

(f) Capacitor voltages of the submodules in MCC-2

Fig. 34 AC voltage control

3.1.6.4 Circulating current control

As mentioned in Subsection 2.5.1, the inner difference current contains a DC component and an AC component corresponding to the circulating current. The frequency of this current is double fundamental frequency. The expression of the three-phase inner difference current is given as [16], [17]

$$i_{diffa} = \frac{I_{dc}}{3} + I_{cir}\cos(2\omega t + \varphi_0) \tag{108}$$

$$
\begin{aligned}
i_{diffb} &= \frac{I_{dc}}{3} + I_{cir}\cos\left[2\left(\omega t - 120^0\right) + \varphi_0\right] \\
&= \frac{I_{dc}}{3} + I_{cir}\cos\left[2\omega t + \varphi_0 + 120^0\right]
\end{aligned}
\tag{109}
$$

$$
\begin{aligned}
i_{diffc} &= \frac{I_{dc}}{3} + I_{cir}\cos\left[2\left(\omega t + 120^0\right) + \varphi_0\right] \\
&= \frac{I_{dc}}{3} + I_{cir}\cos\left[2\omega t + \varphi_0 - 120^0\right]
\end{aligned}
\tag{110}
$$

where I_{cir} is the amplitude of the circulating current.

It can be seen that the phase sequence of the circulating current is a-c-b. From Fig. 20, the three-phase difference voltage is expressed by

$$v_{diffa} = R_0 i_{diffa} + L_0 \frac{di_{diffa}}{dt} \tag{111}$$

$$v_{diffc} = R_0 i_{diffc} + L_0 \frac{di_{diffc}}{dt} \tag{112}$$

$$v_{diffb} = R_0 i_{diffb} + L_0 \frac{di_{diffb}}{dt} \tag{113}$$

This voltage can be rewritten in the dq-frame as

$$v_{diffd} = R_0 i_{cird} + L_0 \frac{di_{cird}}{dt} - 2\omega L_0 i_{cirq} \tag{114}$$

$$v_{diffq} = R_0 i_{cirq} + L_0 \frac{di_{cirq}}{dt} + 2\omega L_0 i_{cird} \tag{115}$$

where v_{diffd}, v_{diffq}, i_{cird} and i_{cirq} are the dq-axis components of the difference voltage and the circulating current, respectively.

48

It is noted that the phase sequence of the voltage and current transformations is a-c-b. The circulating current controller can be expressed by

$$v_{diffd}^* = \left(K_p + \frac{K_i}{s} \right)\left(i_{cird}^* - i_{cird} \right) - 2\omega L_0 i_{cirq} \qquad (116)$$

$$v_{diffq}^* = \left(K_p + \frac{K_i}{s} \right)\left(i_{cirq}^* - i_{cirq} \right) + 2\omega L_0 i_{cird} \qquad (117)$$

The control diagram of the circulating current is shown in Fig. 35. The reference values of the circulating currents are set to zero, $i_{cird}^* = i_{cirq}^* = 0$, to suppress the circulating currents in the phase units.

To control the circulating currents, the control structure of the MMC in Fig. 28 must be modified. The terminal voltage and difference voltage can be deduced from (8), (9) and Fig. 20 as

$$v_{tj} = e_j - \frac{R_0}{2} i_j - \frac{L_0}{2} \frac{di_j}{dt} \qquad (118)$$

$$v_{diffj} = \frac{V_{dc}}{2} - \frac{v_{uj} + v_{lj}}{2} \qquad (119)$$

where e_j is the inner electromotive force (EMF) generated in phase j, it is expressed by

$$e_j = \frac{v_{lj} - v_{uj}}{2} \qquad (120)$$

The upper and lower arm reference voltages can be derived from (119) and (120) in a
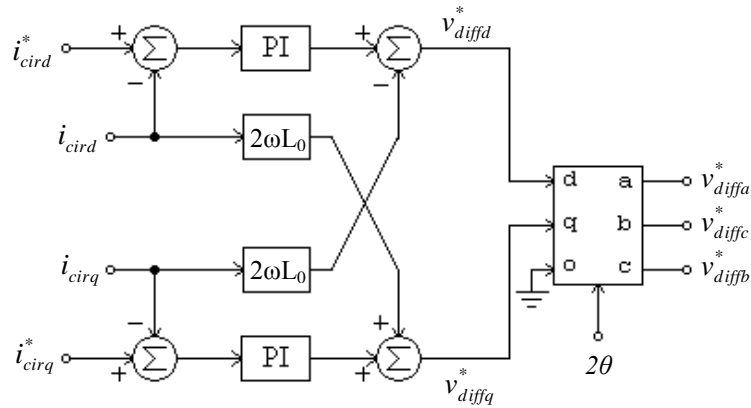
Fig. 35 Circulating current control

consideration of the difference voltage as

$$v_{uj}^* = \frac{V_{dc}}{2} - e_j^* - v_{diffj}^*$$ (121)

$$v_{lj}^* = \frac{V_{dc}}{2} + e_j^* - v_{diffj}^*$$ (122)

By combining Fig. 28, Fig. 35, (121) and (122), the modified control structure of the MMC can be expressed in Fig. 36.

To evaluate the effectiveness of the circulating current control method, a simulation is established based on the parameters in Table 2. The simulation results are carried out in two cases:

Activating the circulating current controller: In this case, the active and reactive powers are set to 200 MW and 0 MVar, respectively, and it is shown in Fig. 37(a). The circulating current controller is deactivated at the starting time. Thus, the circulating current component in the inner difference current is high as seen in Fig. 37(b). The amplitude of the circulating current is about 1 kA. After the circulating current controller is activated at t = 1 s, the circulating current is suppressed. The inner difference current only remains the DC current component. This demonstrates the effectiveness of the control method. It can also be seen that the distortion of the upper and lower arm currents is eliminated, and the arm current waveforms become sinusoidal waveforms as illustrated in Fig. 37(c). With the circulating current controller, the ripple of the capacitor voltages is reduced from 7% to 4.2% as shown
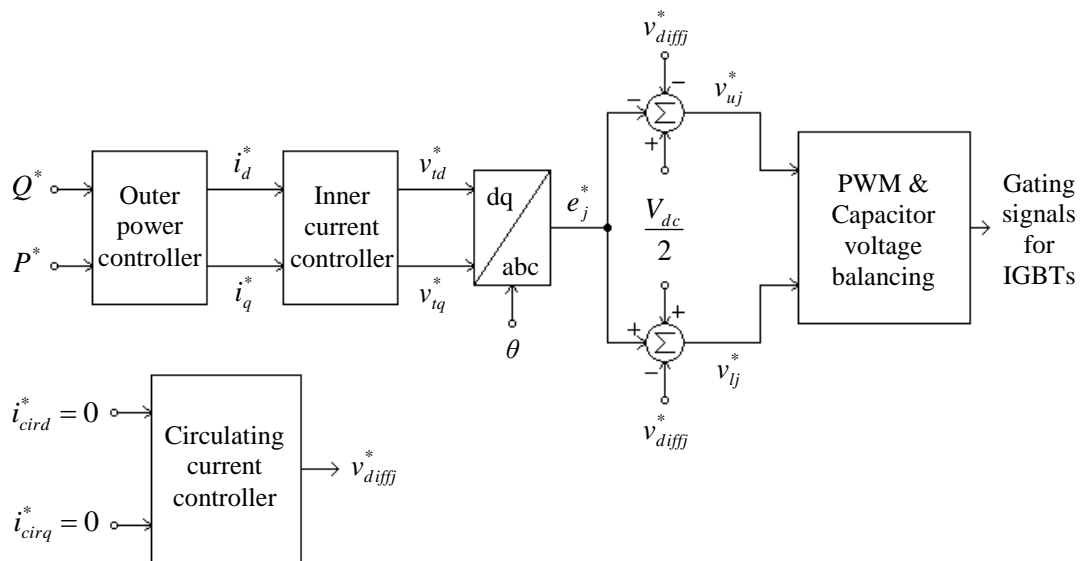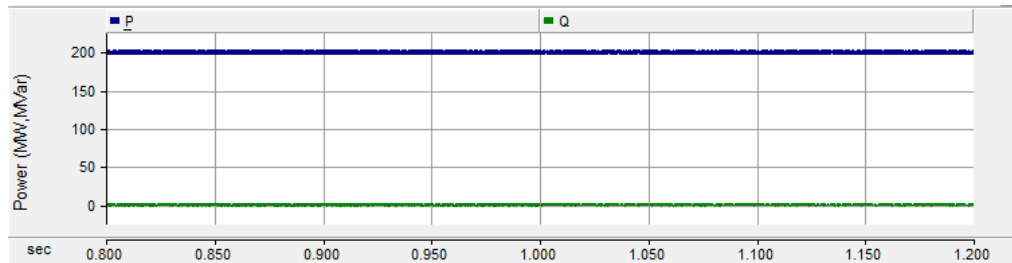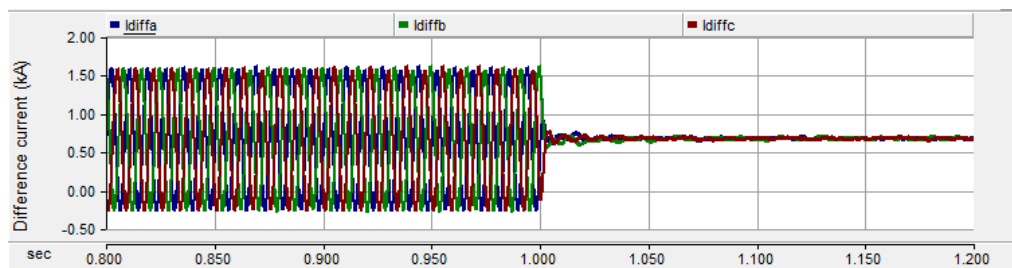

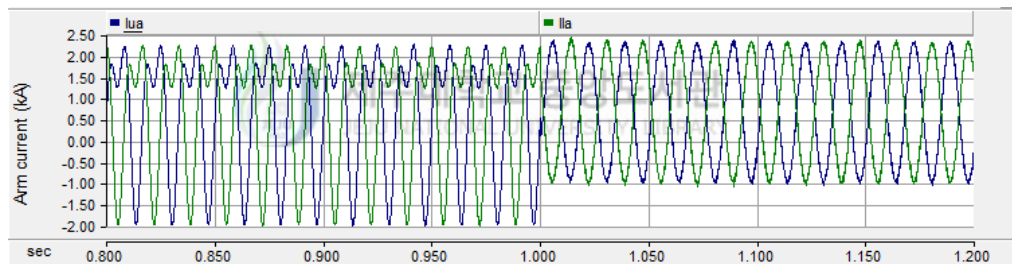Fig. 36 Modified control structure of the MMC in HVDC system

in Fig. 37(d). Fig. 37(e) is the AC output current. It isn't almost changed by the operation of the circulating current controller.
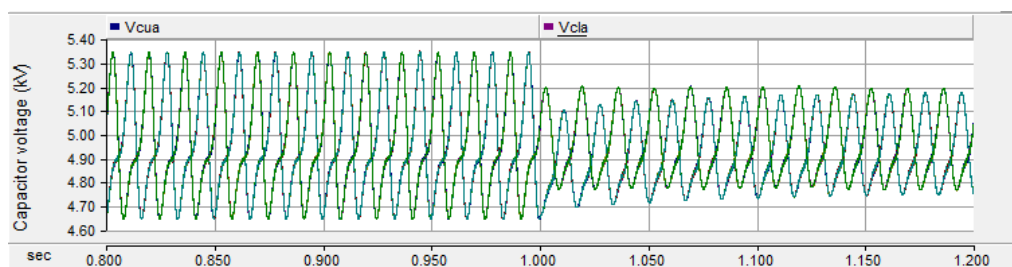

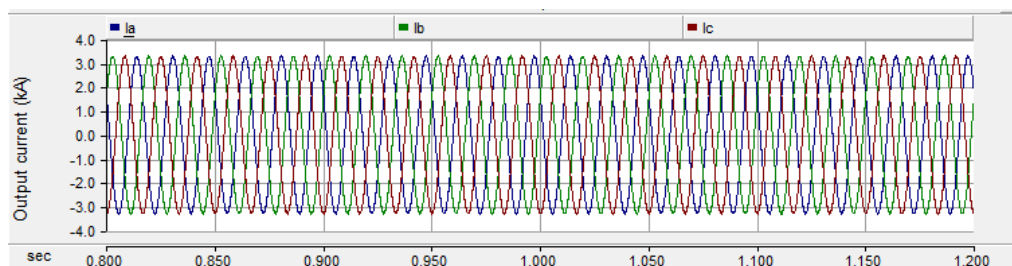(a) Active and reactive powers

(b) Inner difference currents

(c) Upper and lower arm currents

(d) Capacitor voltages

(e) AC output current

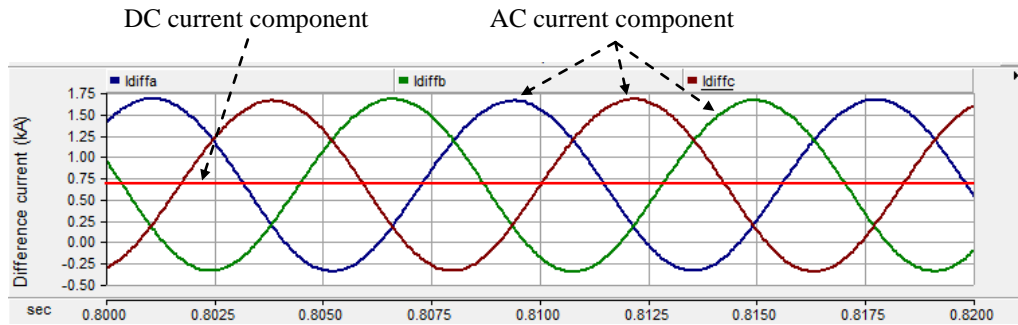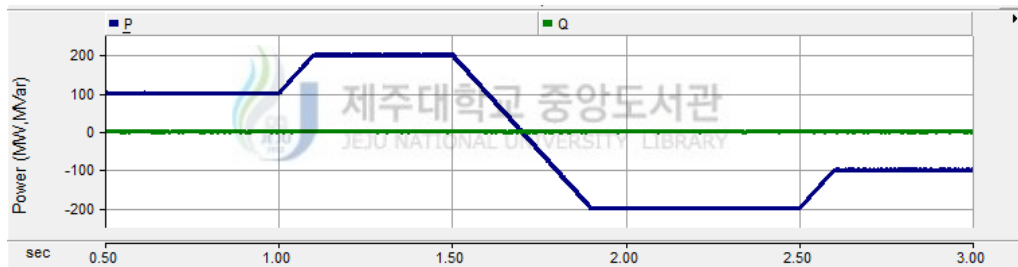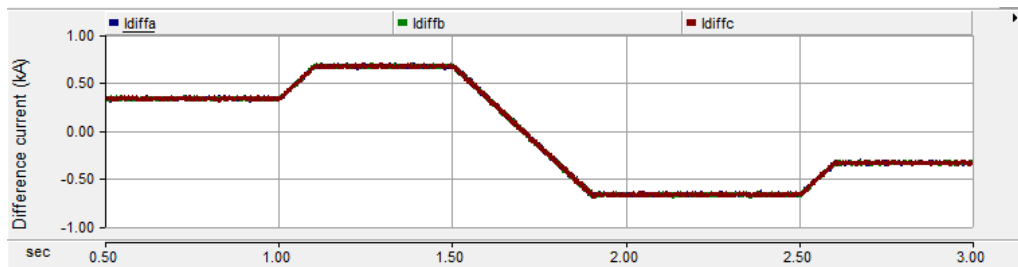Fig. 37 Eliminating the circulating currents

Fig. 38 Zoom of the inner difference currents

A zoom of the inner difference current is shown in Fig. 38 to understand particularly about this current. It can be seen clearly the DC and AC components of the inner difference current. The AC component has the frequency of 120 Hz and the phase sequence is a-c-b.
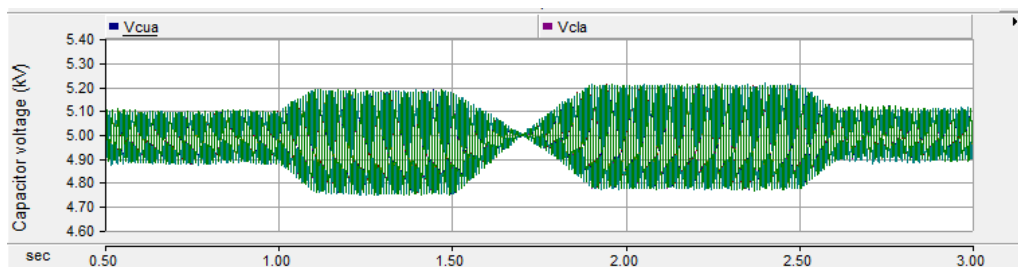
Variable power: In this case, the circulating current controller is tested under the variable power conditions. The initial value of the active power, *P*, is 100 MW. Then, the active

(a) Active and reactive powers

(b) Inner difference current

(c) Capacitor voltages

Fig. 39 Operation of the circulating current controller under variable power

power will be changed at the times as follows: at t = 1 s, P = 200 MW; at t = 1.5 s, P = -200 MW; at t = 2.5 s, P = -100 MW. The reactive power is set to zero, and the circulating current controller is operating during the simulation. The active and reactive powers are shown in Fig. 39(a). The AC current component in the inner difference current is controlled to zero. With the circulating current controller, the inner difference current is a pure DC current as shown in Fig. 39(b). The capacitor voltages in the upper and lower arms are expressed in Fig. 39(c). It is oscillating around the average value and is kept in balancing.

3.2 Control of the MMC-HVDC system under unbalanced voltage conditions

Because of the transient faults on the power grid, the three-phase voltage can become unbalanced. As a result, the waveform of the three-phase current will be distorted. The grid voltage and current contain positive, negative and zero sequence components. The negative sequence component causes oscillation in the active and reactive powers. Thus, the mission of the current controller under unbalanced voltage conditions is to achieve a balance in the output current or to eliminate the oscillation in the active and reactive powers. There are many control methods to solve this problem [20], [21], [42], [43].

This section focuses on two methods that use the PI current controller in the dq-frame and the PR current controller in the stationary reference frame ($\alpha\beta$-frame).

- In the dq-frame, the current controller is divided into a positive sequence current controller and a negative sequence current controller. Thus, four PI controllers are used.

- In the $\alpha\beta$-frame, only two PR controllers are used.

In this study, the single phase to ground fault is considered because it is the most severe fault among the transient faults. The fault occurs on the AC side of the MMC-2 as shown in Fig. 40.
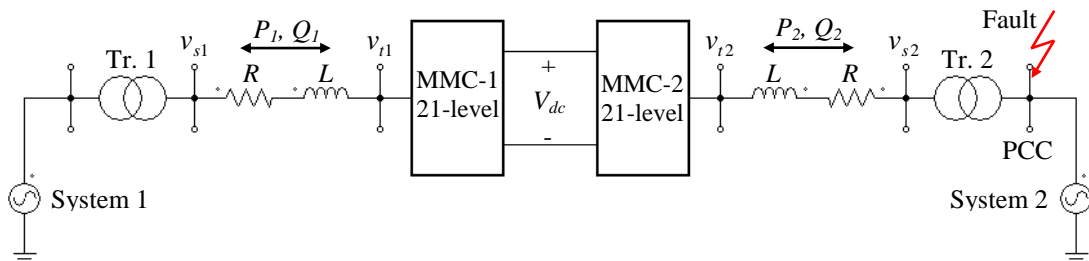

Fig. 40 Single-line diagram of the MMC-HVDC system under fault condition

3.2.1 Symmetrical component theory

Under unbalanced voltage conditions, the three-phase voltage and current will contain three components, namely the positive, negative and zero sequence components. To design the current controller, these components must be separated into three independent components. A method has been proposed in [44] to solve this problem. This method is represented for the voltage. The current will be done in the similar way. The three-phase voltage is first transformed into the αβ-frame by using Clarke transformation as follows.

$$
\begin{bmatrix} v_{s\alpha} \\ v_{s\beta} \\ v_{s0} \end{bmatrix} = \begin{bmatrix} T_{\alpha\beta} \end{bmatrix} \begin{bmatrix} v_{sa} \\ v_{sb} \\ v_{sc} \end{bmatrix} = \begin{bmatrix} 1 & -\dfrac{1}{2} & -\dfrac{1}{2} \\ 0 & \dfrac{\sqrt{3}}{2} & -\dfrac{\sqrt{3}}{2} \\ \dfrac{1}{2} & \dfrac{1}{2} & \dfrac{1}{2} \end{bmatrix} \begin{bmatrix} v_{sa} \\ v_{sb} \\ v_{sc} \end{bmatrix} \tag{123}
$$

where $v_{s\alpha}$ and $v_{s\beta}$ are the αβ-axis components of the three-phase voltage in the αβ-frame.

The αβ-axis voltage contains two components, namely positive and negative sequence components, with the same frequency. If a Y-Δ transformer is used, the zero sequence component will be zero. The positive and negative sequence components in the αβ-frame can be calculated as [44]

$$
\begin{bmatrix} v_{s\alpha}^+ \\ v_{s\beta}^+ \end{bmatrix} = \frac{1}{2} \begin{bmatrix} 1 & -q \\ q & 1 \end{bmatrix} \begin{bmatrix} v_{s\alpha} \\ v_{s\beta} \end{bmatrix} \tag{124}
$$

$$
\begin{bmatrix} v_{s\alpha}^- \\ v_{s\beta}^- \end{bmatrix} = \frac{1}{2} \begin{bmatrix} 1 & q \\ -q & 1 \end{bmatrix} \begin{bmatrix} v_{s\alpha} \\ v_{s\beta} \end{bmatrix} \tag{125}
$$

where $v_{s\alpha}^+, v_{s\beta}^+, v_{s\alpha}^-$ and $v_{s\beta}^-$ are the positive and negative sequence components of the voltage in the αβ-frame. q is a phase shift operator applied in the time domain to obtain an in-quadrature version of the input waveform. If the voltage is defined by $v_{sa} = sin\omega t$, q will be 90^0-leading. If the voltage is defined by $v_{sa} = cos\omega t$, q will be 90^0- lagging.

The transformation of voltage between the dq-frame and αβ-frame are expressed by [39], [44]

$$
\begin{bmatrix} v_{sd}^+ \\ v_{sq}^+ \end{bmatrix} = \begin{bmatrix} \cos\theta & -\sin\theta \\ \sin\theta & \cos\theta \end{bmatrix} \begin{bmatrix} v_{s\alpha}^+ \\ v_{s\beta}^+ \end{bmatrix} \tag{126}
$$

$$\begin{bmatrix} v_{sd}^- \\ v_{sq}^- \end{bmatrix} = \begin{bmatrix} \cos(-\theta) & -\sin(-\theta) \\ \sin(-\theta) & \cos(-\theta) \end{bmatrix} \begin{bmatrix} v_{s\alpha}^- \\ v_{s\beta}^- \end{bmatrix} \tag{127}$$

$$\begin{bmatrix} v_{s\alpha}^+ \\ v_{s\beta}^+ \end{bmatrix} = \begin{bmatrix} \cos\theta & \sin\theta \\ -\sin\theta & \cos\theta \end{bmatrix} \begin{bmatrix} v_{sd}^+ \\ v_{sq}^+ \end{bmatrix} \tag{128}$$

$$\begin{bmatrix} v_{s\alpha}^- \\ v_{s\beta}^- \end{bmatrix} = \begin{bmatrix} \cos(-\theta) & \sin(-\theta) \\ -\sin(-\theta) & \cos(-\theta) \end{bmatrix} \begin{bmatrix} v_{sd}^- \\ v_{sq}^- \end{bmatrix} \tag{129}$$

where $v_{sd}^+, v_{sq}^+, v_{sd}^-$ and v_{sq}^- are the dq-axis voltage components in the positive and negative synchronous reference frames (dq$^+$- and dq$^-$-frames), respectively.

Fig. 41 is an illustration for the above analysis. A single phase to ground fault occurs at t = 0.2 s and is removed at t = 0.4 s. During the fault, the three-phase grid voltage is unbalanced as shown in Fig. 41(a). By using (123)-(129), the voltage components in the αβ-frame and dq-frame are achieved in Fig. 41(b)-(h), respectively.
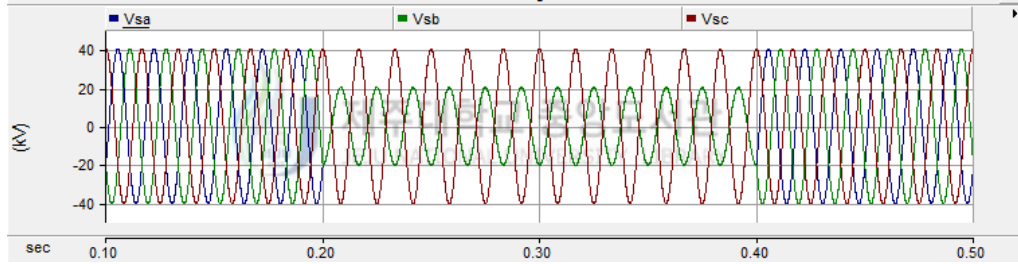
(a) Three-phase grid voltage
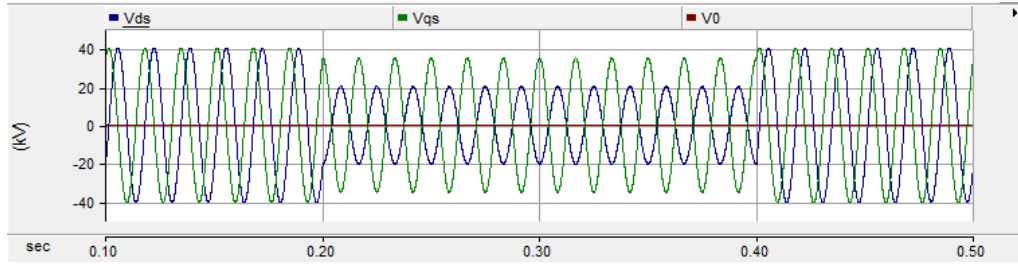
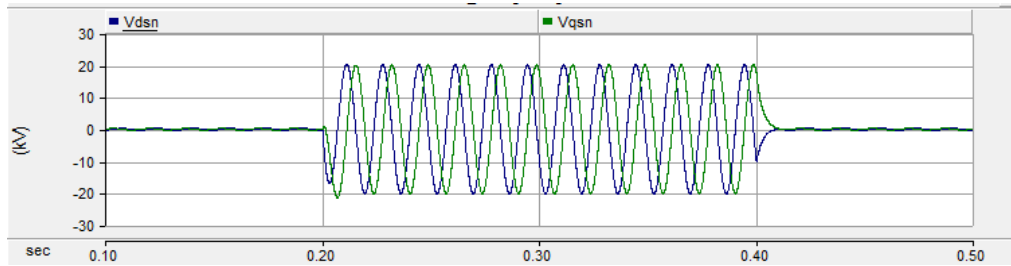(b) Grid voltage in the αβ-frame
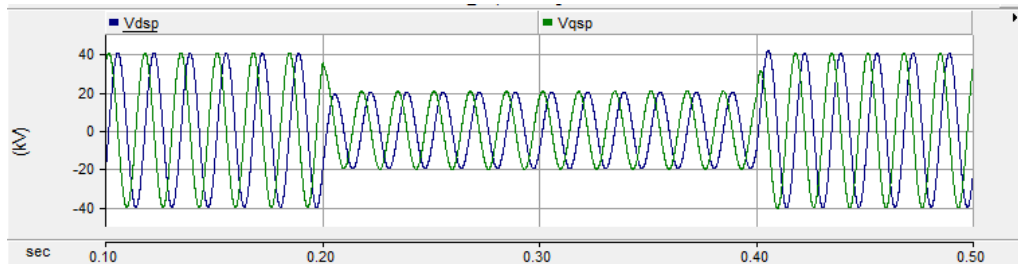
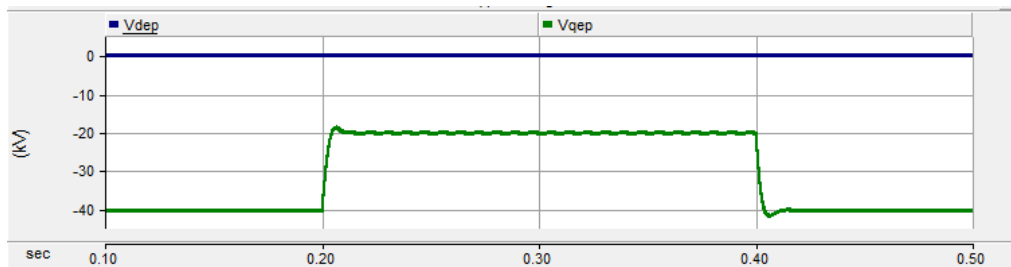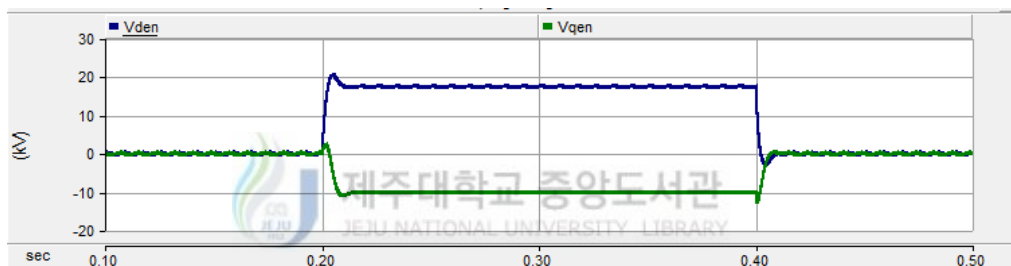(c) Positive sequence component of the grid voltage in the αβ-frame
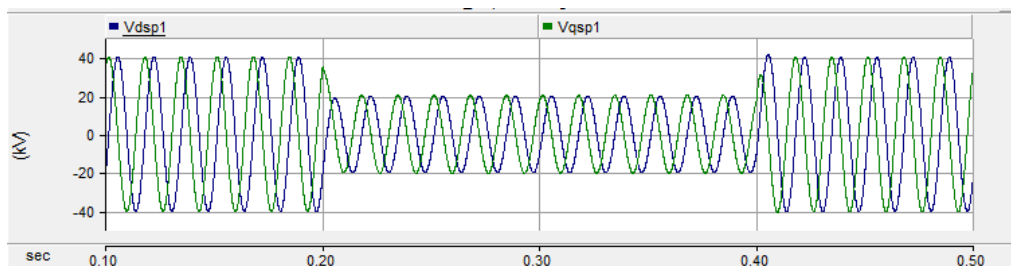
Fig. 41 Separating positive and negative sequence components

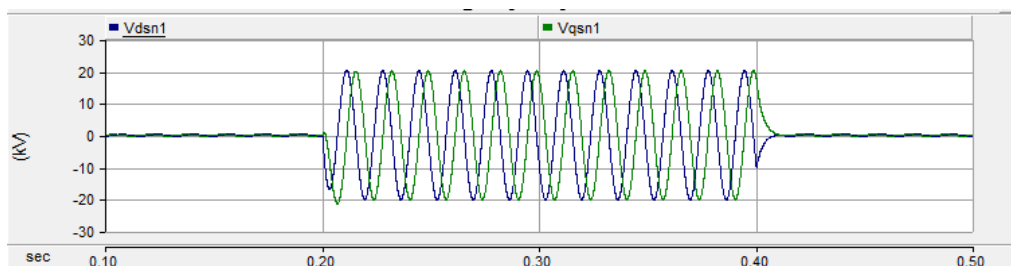(d) Negative sequence component of the grid voltage in the αβ-frame

(e) Positive sequence component of the grid voltage in the dq-frame

(f) Negative sequence component of the grid voltage in the dq-frame

(g) Positive sequence component of the grid voltage in the αβ-frame

(h) Negative sequence component of the grid voltage in the αβ-frame

Fig. 41 Separating positive and negative sequence components (cont.)

3.2.2 Modified circulating current control

Under balanced voltage conditions, the circulating current only contains the negative sequence component at double fundamental frequency. However, under unbalanced voltage conditions, the circulating current contains positive, negative and zero sequence components at the double fundamental frequency. The inner difference current can be redefined as [45]

$$i_{diffj} = \frac{I_{dc}}{3} + i_{cirj} = \frac{I_{dc}}{3} + i_{cirj}^+ + i_{cirj}^- + i_{cirj}^0 \tag{130}$$

where i_{cirj}^+, i_{cirj}^- and i_{cirj}^0 are the positive, negative and zero sequence components of the circulating current.

The positive and negative sequence components of the circulating current only flow within the phase units and don't affect to the AC side and the DC-link, but it can cause losses in the arms. The zero sequence component can flow into the DC-link and generates second-order harmonic in the DC current. Thus, these components of the circulating current should be controlled to zero. In this case, if the controller is designed in the similar way to the current controller in Fig. 45, it will be complicated and many more PI controllers must be used. To overcome this problem, the PR controller in the αβ-frame, which will be explained in the next section, is proposed. The advantage of the PR controller is that it can control the current in the αβ-frame. Decomposition into separate components is not necessary. Moreover, the PR controller is also effective to control the zero sequence component. The modified circulating current controller is shown Fig. 42. The PR controller's cutoff frequency is tuned at the double fundamental frequency because of the double fundamental frequency of the circulating current.
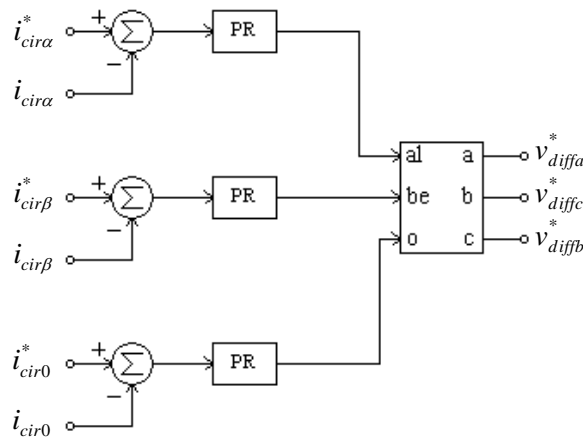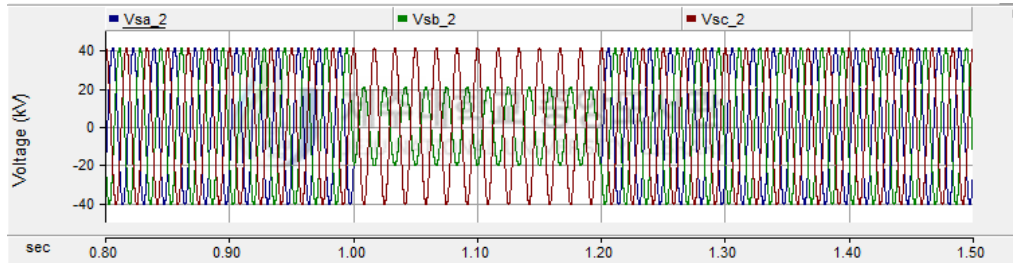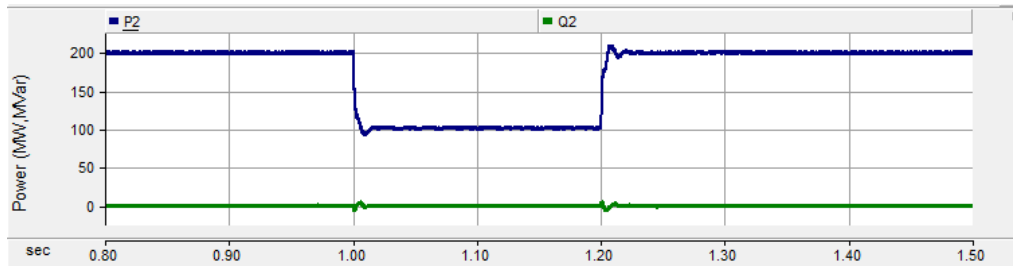

Fig. 42 Modified circulating current control

In Fig. 42, $i_{cirα}$, $i_{cirβ}$, and i_{cir0} are the αβ0-axis components of the circulating current. To eliminate the circulating current, the reference values of these current components are set to zero. A transfer function of the PR current controller is given by

$$G_{PR} = K_p + \frac{K_i s}{s^2 + (2\omega)^2} \tag{131}$$

Fig. 43 and Fig. 44 show the illustration of conventional and modified circulating current control methods under unbalanced voltage condition by using the parameters in Table 2. A single phase to ground fault occurs at t = 1 s and is removed at t = 1.2 s as expressed in Fig. 43(a) and Fig. 44(a). Because the circulating current doesn't affect to the AC side, the active and reactive powers in two methods are almost the same as shown in Fig. 43(b) and Fig. 44(b). The effectiveness of the modified control method with PR controller is proved in Fig. 44(c)-(e). The oscillation in the inner difference current is removed significantly under unbalanced voltage condition. As a result, the ripple in the DC current is also eliminated.

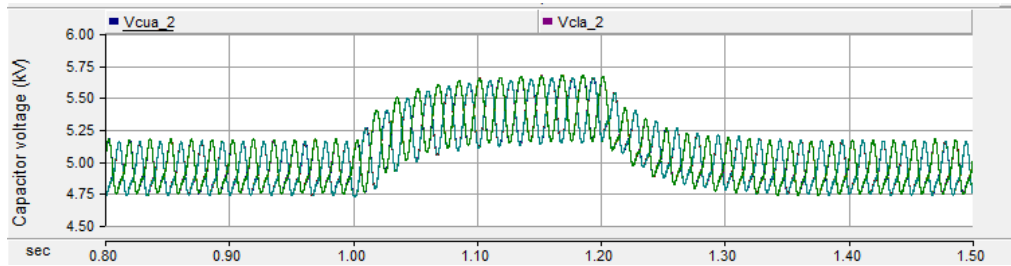
(a) Three-phase grid voltage
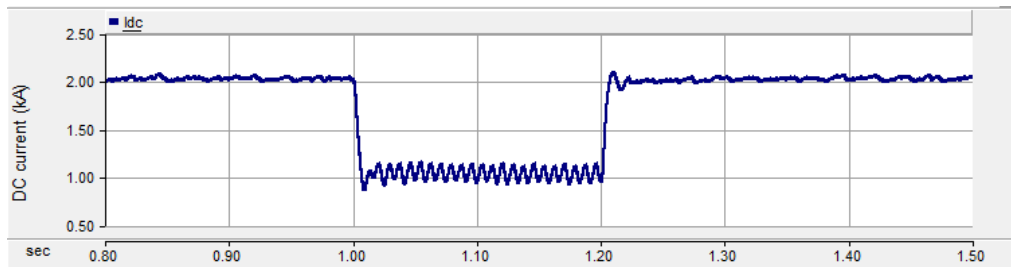

(b) Active and reactive powers
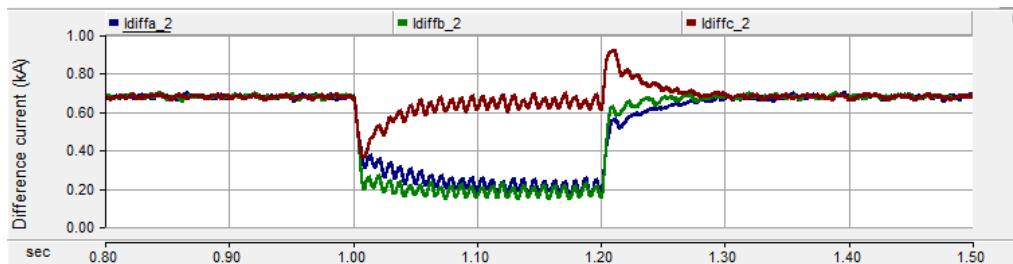
(c) Inner difference currents

Fig. 43 Conventional circulating current control under unbalanced voltage condition
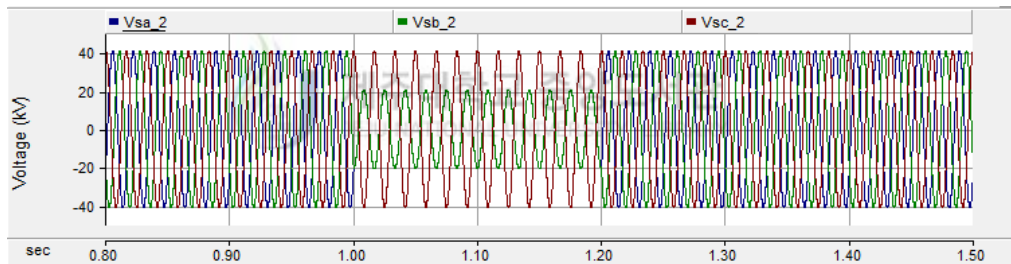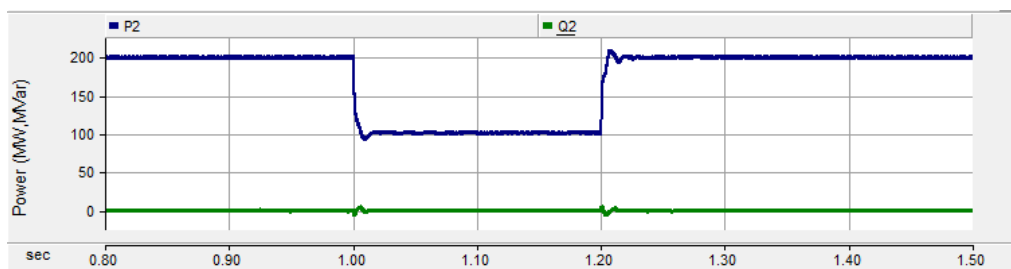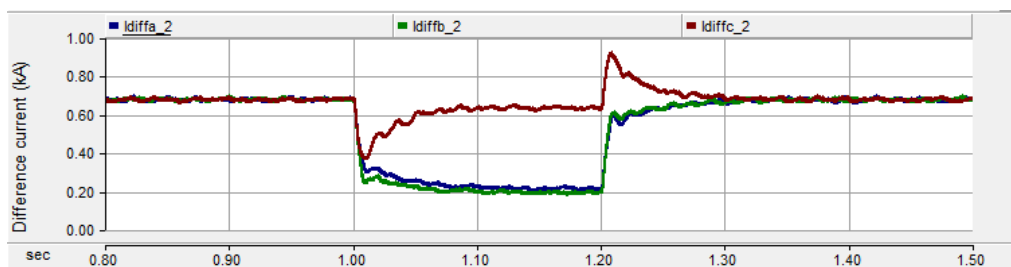
(d) Capacitor voltages

(e) DC current

Fig. 43 Conventional circulating current control under unbalanced voltage condition (cont.)
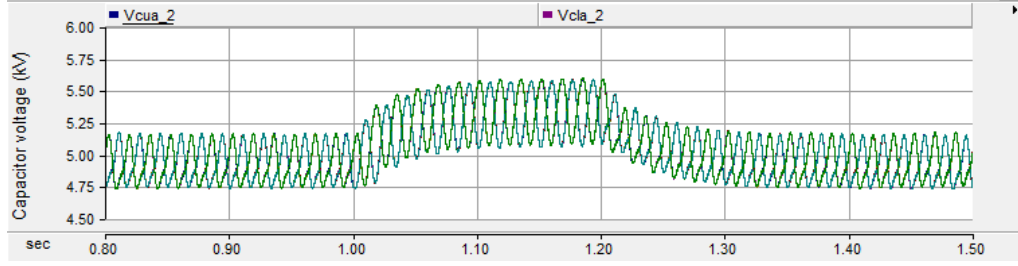

(a) Three-phase grid voltage
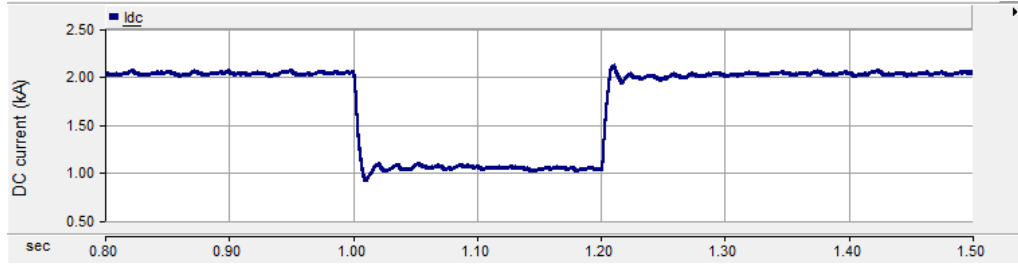

(b) Active and reactive powers

(c) Inner difference currents

Fig. 44 Modified circulating current control under unbalanced voltage condition

59

(d) Capacitor voltages

(e) DC current

Fig. 44 Modified circulating current control under unbalanced voltage condition (cont.)

3.2.3 Current control with PI controller

Because the existence of the negative sequence component under unbalanced voltage conditions, the (82) and (83) are rewritten as

$$v_{td\_k}^+ = -Ri_{d\_k}^+ - L\frac{di_{d\_k}^+}{dt} + v_{sd\_k}^+ + \omega L i_{q\_k}^+ \tag{132}$$

$$v_{tq\_k}^+ = -Ri_{q\_k}^+ - L\frac{di_{q\_k}^+}{dt} + v_{sq\_k}^+ - \omega L i_{d\_k}^+ \tag{133}$$

$$v_{td\_k}^- = -Ri_{d\_k}^- - L\frac{di_{d\_k}^-}{dt} + v_{sd\_k}^- - \omega L i_{q\_k}^- \tag{134}$$

$$v_{tq\_k}^- = -Ri_{q\_k}^- - L\frac{di_{q\_k}^-}{dt} + v_{sq\_k}^- + \omega L i_{d\_k}^- \tag{135}$$

where superscripts "+" and "-" show the positive and negative sequence components of the voltage and current.

Then, the current controller can be expressed by

$$v_{td\_k}^{+*} = -\left(K_p + \frac{K_i}{s}\right)\left(i_{d\_k}^{+*} - i_{d\_k}^+\right) + v_{sd\_k}^+ + \omega L i_{q\_k}^+ \tag{136}$$

60

$$v_{tq\_k}^{+*} = -\left(K_p + \frac{K_i}{s}\right)\left(i_{q\_k}^{+*} - i_{q\_k}^{+}\right) + v_{sq\_k}^{+} - \omega L i_{d\_k}^{+} \qquad (137)$$

$$v_{td\_k}^{-*} = -\left(K_p + \frac{K_i}{s}\right)\left(i_{d\_k}^{-*} - i_{d\_k}^{-}\right) + v_{sd\_k}^{-} - \omega L i_{q\_k}^{-} \qquad (138)$$

$$v_{tq\_k}^{-*} = -\left(K_p + \frac{K_i}{s}\right)\left(i_{q\_k}^{-*} - i_{q\_k}^{-}\right) + v_{sq\_k}^{-} + \omega L i_{d\_k}^{-} \qquad (139)$$

The control diagram of the output current under unbalanced voltage conditions is shown in Fig. 45. It consists of two parts, a positive sequence current controller and a negative sequence current controller. The positive sequence current controller operates in the similar way to the case of balanced voltage. The negative sequence current controller is responsible for eliminating the negative sequence component of the current or the oscillation in the active and reactive powers. The output signals of the current controllers are transformed into
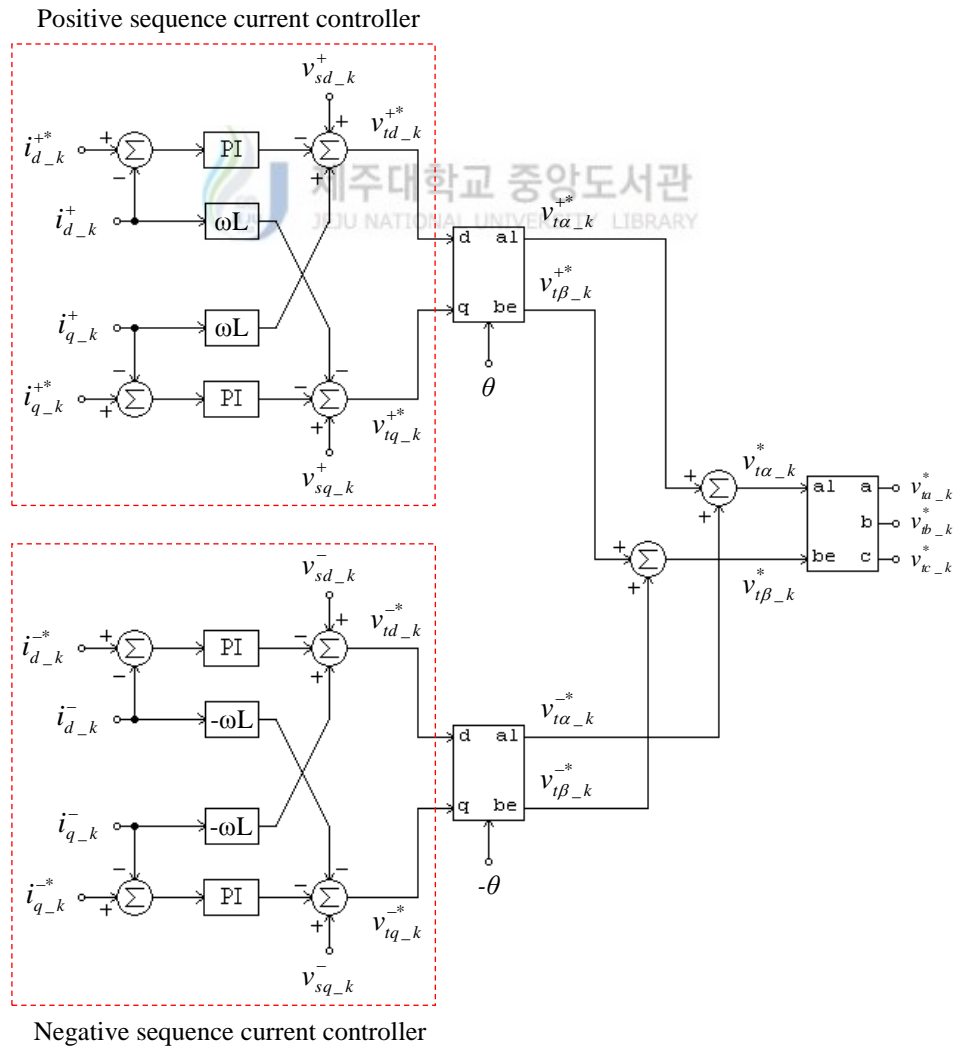

Fig. 45 Control diagram of the current under unbalanced voltage conditions

the αβ-frame. The positive and negative sequence voltages in the αβ-frame are added together to achieve the αβ-axis voltage which is then transformed to the abc-frame.

Under unbalanced voltage conditions, the active and reactive powers at the PCC are calculated by [20], [46]

$$P = P_k + P_{\sin2\_k} \sin 2\omega t + P_{\cos2\_k} \cos 2\omega t \tag{140}$$

$$Q = Q_k + Q_{\sin2\_k} \sin 2\omega t + Q_{\cos2\_k} \cos 2\omega t \tag{141}$$

where P_k and Q_k are the real active and reactive powers which are transferred by the MMC-HVDC system. P_{sin2_k}, P_{cos2_k}, Q_{sin2_k} and Q_{cos2_k} are the power components because of the unbalanced voltage conditions. They are given by

$$
\begin{bmatrix}
P_k \\
P_{\sin2\_k} \\
P_{\cos2\_k} \\
Q_k \\
Q_{\sin2\_k} \\
Q_{\cos2\_k}
\end{bmatrix}
= \frac{3}{2}
\begin{bmatrix}
v_{sd\_k}^+ & v_{sq\_k}^+ & v_{sd\_k}^- & v_{sq\_k}^- \\
-v_{sq\_k}^- & v_{sd\_k}^- & v_{sq\_k}^+ & -v_{sd\_k}^+ \\
v_{sd\_k}^- & v_{sq\_k}^- & v_{sd\_k}^+ & v_{sq\_k}^+ \\
-v_{sq\_k}^+ & v_{sd\_k}^+ & -v_{sq\_k}^- & v_{sd\_k}^- \\
-v_{sd\_k}^- & -v_{sq\_k}^- & v_{sd\_k}^+ & v_{sq\_k}^+ \\
-v_{sq\_k}^- & v_{sd\_k}^- & -v_{sq\_k}^+ & v_{sd\_k}^+
\end{bmatrix}
\begin{bmatrix}
i_{d\_k}^+ \\
i_{q\_k}^+ \\
i_{d\_k}^- \\
i_{q\_k}^-
\end{bmatrix}
\tag{142}
$$

Depending on the control aims, the reference values of the positive and negative sequence currents can be calculated from (142). The test is performed by using the parameters of the MMC-HVDC system in Table 2. The single phase to ground fault, which is shown in Fig. 40, is applied to the AC side of the MMC-2 at t = 1 s and is removed at t = 1.2 s. The reference values of the active and reactive powers are set to 200 MW and 0 MVar during test, respectively.

3.2.3.1 Eliminating negative sequence current

The negative sequence current is controlled to zero under unbalanced voltage conditions to prevent a large current occurred in the MMC-HVDC system and an unbalanced current injected into the power grid. As a result, the output current of the MMC-HVDC system is balanced. The reference values of the dq-axis negative sequence currents are given by

$$i_{d\_k}^{-*} = i_{q\_k}^{-*} = 0 \tag{143}$$

Because $v_{d\_k}^+ = 0$, the references of the dq-axis positive sequence currents are calculated as

$$i_{d\_k}^{+*} = -\frac{2Q_k^*}{3v_{sq\_k}^+} \tag{144}$$

$$i_{q\_k}^{+*} = \frac{2P_k^*}{3v_{sq\_k}^+} \tag{145}$$

The operation of the MMC-HVDC system in this case is shown in Fig. 46 and Fig. 47. The three-phase grid voltage is expressed in Fig. 46(a). The q-axis positive sequence current is set to the limit value, and the dq-axis negative sequence currents are controlled to zero during fault (Fig. 46(c)-(d)). Thus, the three-phase output current is balanced (Fig. 46(b)). The real active power in the MMC-HVDC system is reduced by 30% (Fig. 46(e)), meanwhile the active and reactive powers at the PCC is still oscillating because of the unbalanced voltage condition (Fig. 46(f)). The inner difference currents are distributed unequally in the arms. Phase A and B of the inner difference currents are decreased about 44%, while the phase C has a decrement of 2.9% (Fig. 46(g)). The capacitor voltages are affected by the unbalanced voltage condition. The typical capacitor voltages in phase A are shown in Fig. 46(h). It is shifted from the nominal value.
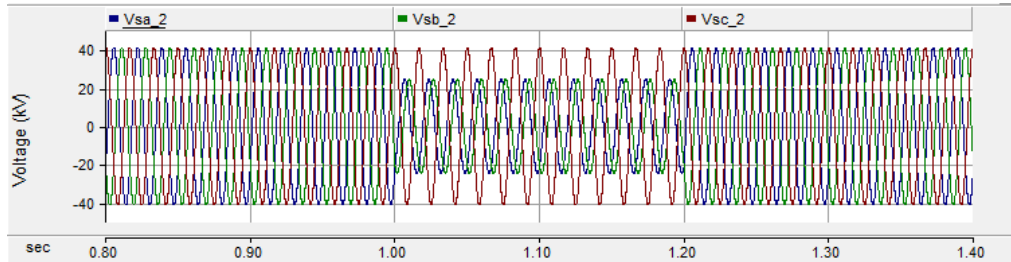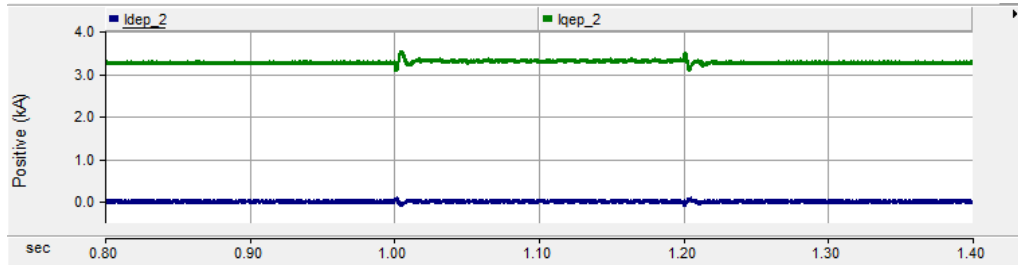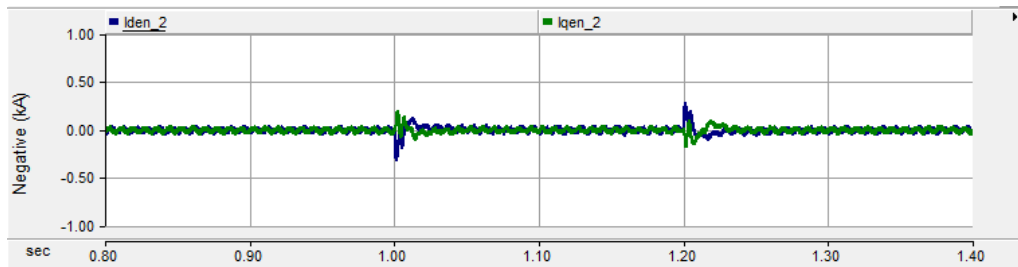

(a) Three-phase grid voltage at MMC-2 side
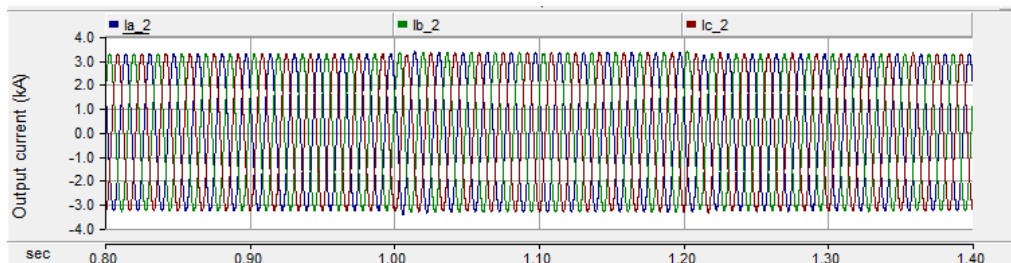
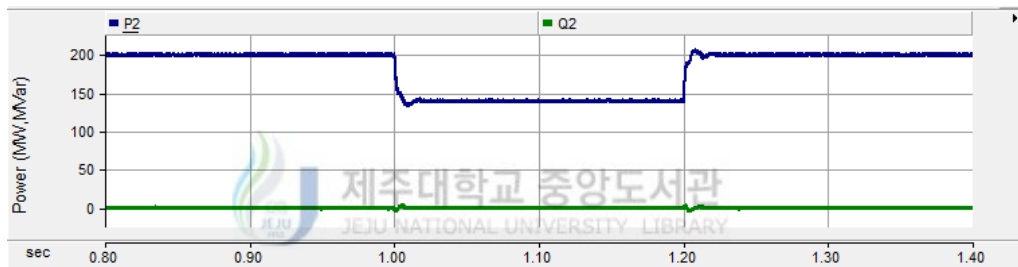(b) Three-phase output current of MMC-2

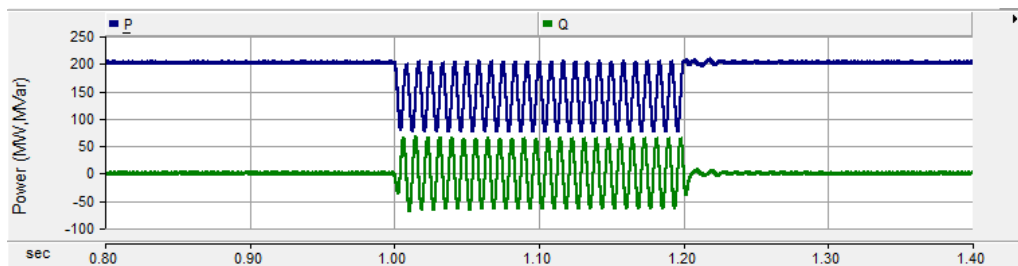Fig. 46 Eliminating negative sequence current - MMC-2 side

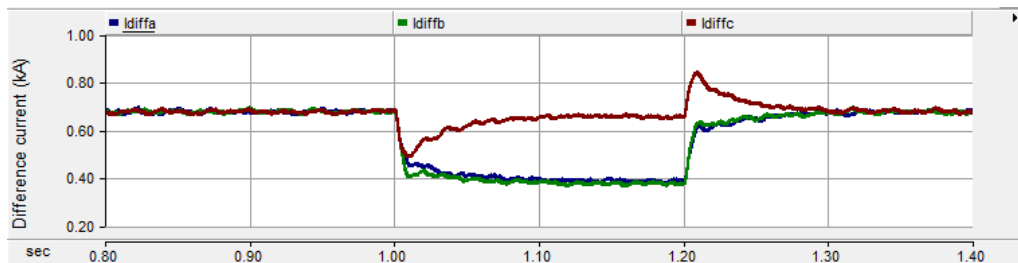(c) dq-axis positive sequence currents of MMC-2

(d) dq-axis negative sequence currents of MMC-2

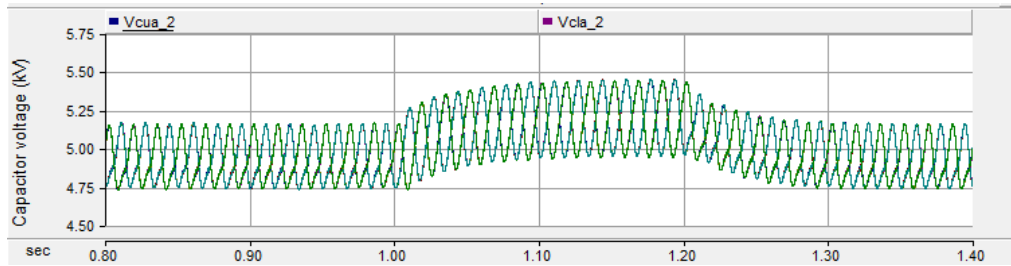(e) Active and reactive powers of MMC-2

(f) Active and reactive powers at the PCC

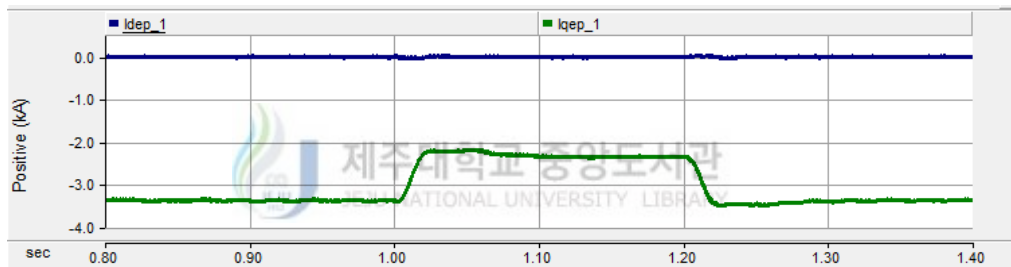(g) Inner difference currents of MMC-2

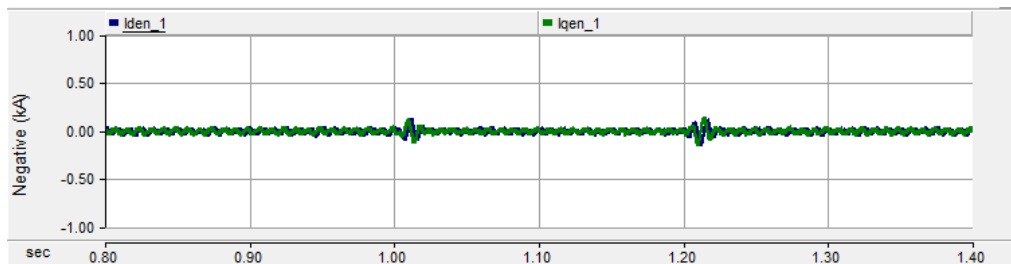Fig. 46 Eliminating negative sequence current - MMC-2 side (cont.)

(h) Capacitor voltages of the submodules in MMC-2

Fig. 46 Eliminating negative sequence current - MMC-2 side (cont.)

With the control method, the fault doesn't propagate to the other side of the MMC-HVDC system. The MMC-1 is still in the normal operation. The output current of the MMC-1 only contains the positive sequence component as shown in Fig. 47(a)-(b). The DC-link voltage has an oscillation at the transient time when the fault occurs (Fig. 47(e)). However, this oscillation is not significant.

(a) dq-axis positive sequence currents of MMC-1

(b) dq-axis negative sequence currents of MMC-1

(c) Active and reactive powers of MMC-1

Fig. 47 Eliminating negative sequence current - MMC-1 side

(d) Inner difference currents of MMC-1

(e) DC-link voltage

(f) Capacitor voltages of the submodules in MMC-1

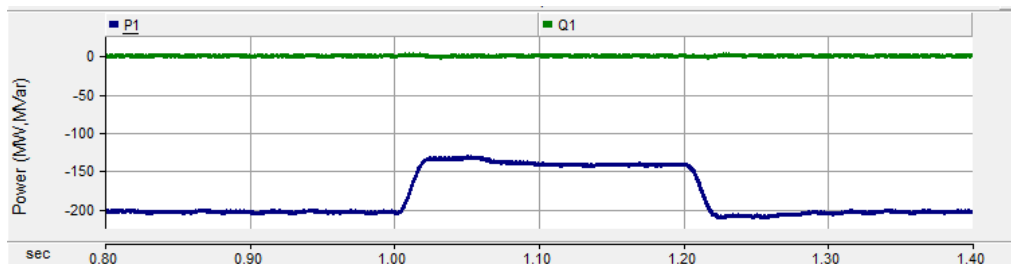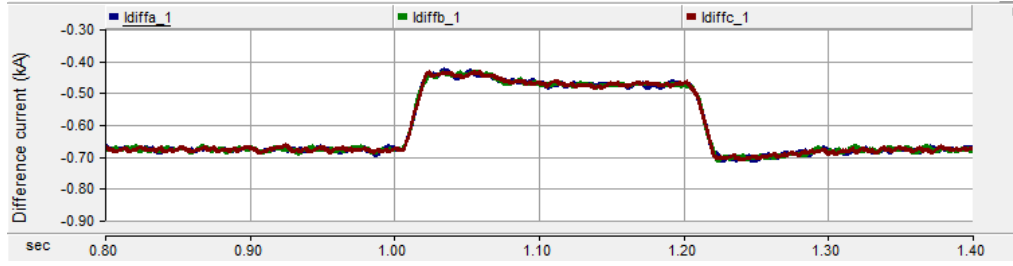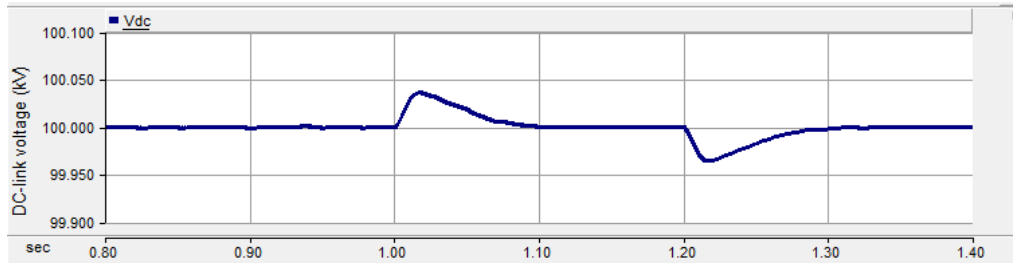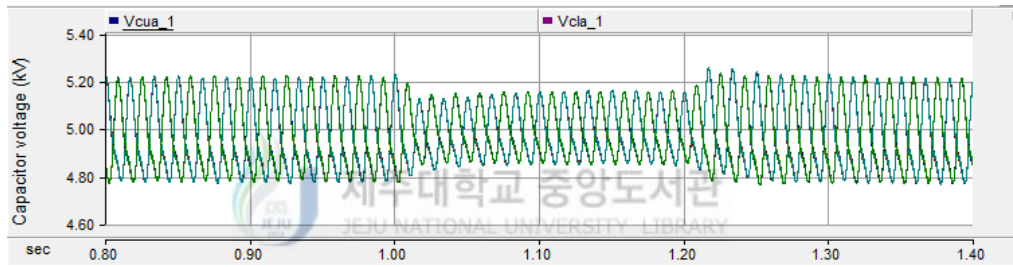Fig. 47 Eliminating negative sequence current - MMC-1 side (cont.)

3.2.3.2 Eliminating oscillation of the active power at the PCC

The unbalanced voltage conditions cause the oscillation in the active power at the PCC. If the capacity of the MMC-HVDC system is high enough, this oscillation will have negative effects to the power system such as tripping relay protection or instability in the system and so on. Thus, the active power oscillation should be eliminated by changing the control method of the MMC-HVDC system. It means that

$$P_{\sin2\_k} = P_{\cos2\_k} = 0 \tag{146}$$

The references of the positive and negative sequence currents can be calculated from (142) as

$$i_{d\_k}^{+*} = -\frac{2v_{sq\_k}^+ Q_k^*}{3\left(v_{sq\_k}^{+2} + v_{sd\_k}^{-2} + v_{sq\_k}^{-2}\right)} \tag{147}$$

66

$$i_{q\_k}^{+*} = \frac{2v_{sq\_k}^{+}P_k^{*}}{3\left(v_{sq\_k}^{+2} - v_{sd\_k}^{-2} - v_{sq\_k}^{-2}\right)} \tag{148}$$

$$i_{d\_k}^{-*} = -\frac{2v_{sq\_k}^{-}Q_k^{*}}{3\left(v_{sq\_k}^{+2} + v_{sd\_k}^{-2} + v_{sq\_k}^{-2}\right)} - \frac{2v_{sd\_k}^{-}P_k^{*}}{3\left(v_{sq\_k}^{+2} - v_{sd\_k}^{-2} - v_{sq\_k}^{-2}\right)} \tag{149}$$

$$i_{q\_k}^{-*} = \frac{2v_{sd\_k}^{-}Q_k^{*}}{3\left(v_{sq\_k}^{+2} + v_{sd\_k}^{-2} + v_{sq\_k}^{-2}\right)} - \frac{2v_{sq\_k}^{-}P_k^{*}}{3\left(v_{sq\_k}^{+2} - v_{sd\_k}^{-2} - v_{sq\_k}^{-2}\right)} \tag{150}$$

The MMC-HVDC system must inject the negative sequence currents to compensate for the oscillation of the active power at the PCC.

Fig. 48 shows the response of the MMC-HVDC system. Because the appearance of the negative sequence current, the three-phase output current is unbalanced (Fig. 48(a)). Phase A and B are increased by 132.7%, which means a severe overcurrent, to compensate for the voltage drop. The q-axis positive sequence current also has an increment of 80% (Fig. 48(b)). The dq-axis negative sequence currents are not zero as seen in Fig. 48(c). Because the reasonable control of the positive and negative sequence currents, the active power of the MMC-2 is remained at the reference value (Fig. 48(d)), and the oscillation of the active power at the PCC is eliminated as seen in Fig. 48(e). However, the reactive power will have a large oscillation of ±222 MVar. The ripples of the capacitor voltages in phase A are increased to 12% during the fault (Fig. 48(g)).
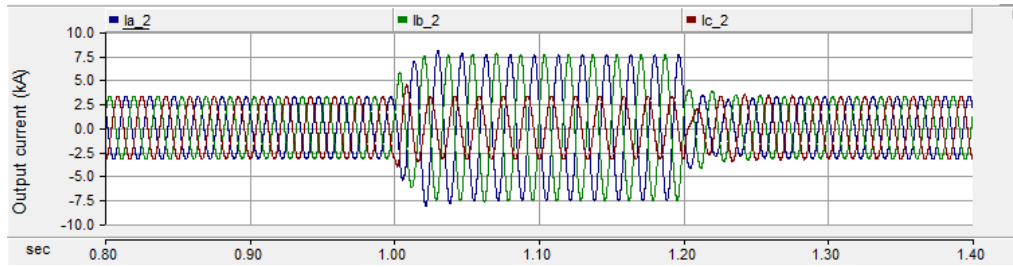
(a) Three-phase output current of MMC-2
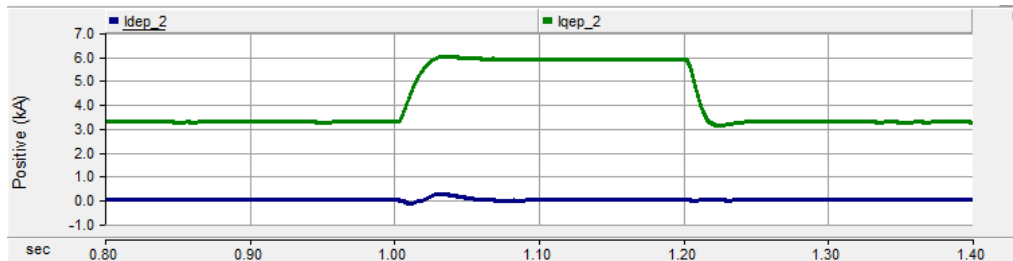
(b) dq-axis positive sequence currents of MMC-2

Fig. 48 Eliminating oscillation of the active power at the PCC
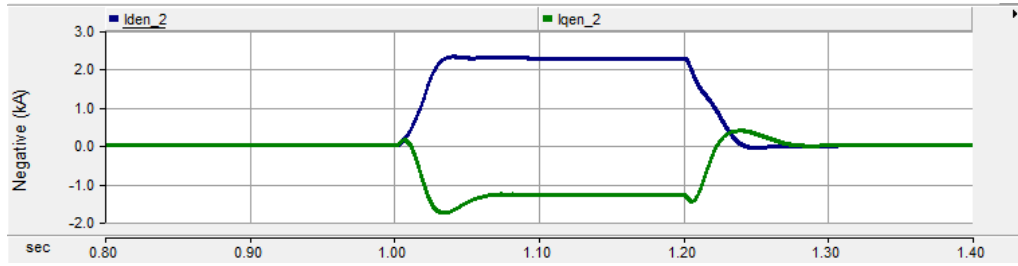
(c) dq-axis negative sequence currents of MMC-2

(d) Active and reactive powers of MMC-2
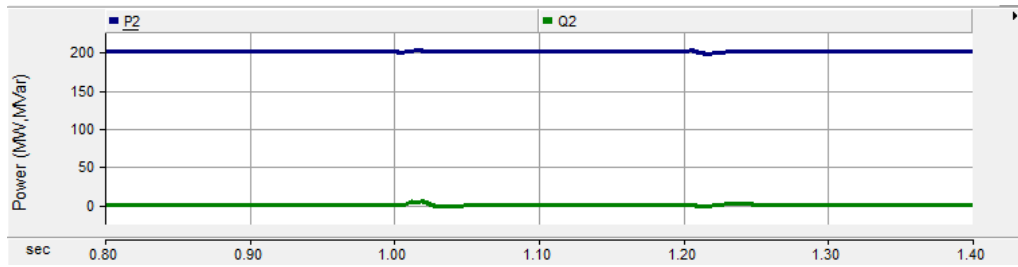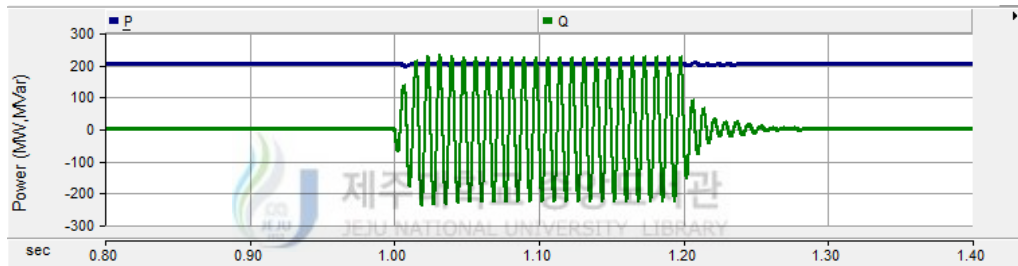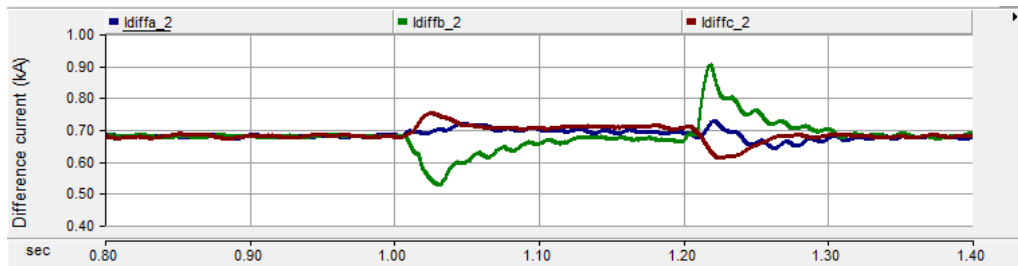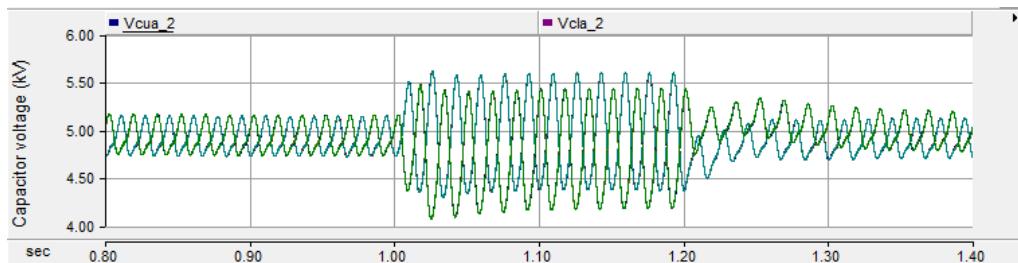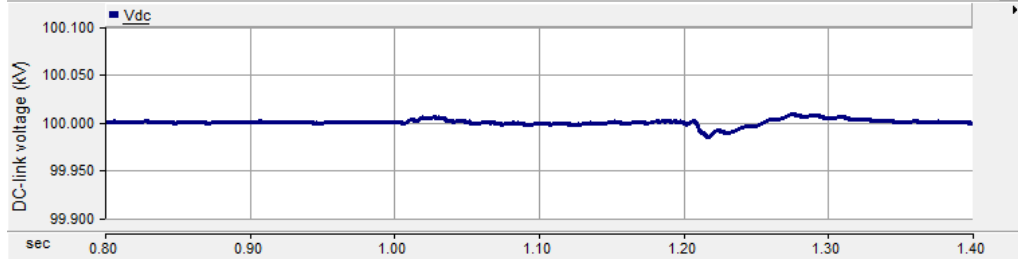

(e) Active and reactive powers at the PCC

(f) Inner difference currents of MMC-2

(g) Capacitor voltages of the submodules in MMC-2

Fig. 48 Eliminating oscillation of the active power at the PCC (cont.)

(h) DC-link voltage

Fig. 48 Eliminating oscillation of the active power at the PCC (cont.)

3.2.3.3 Eliminating oscillation of the reactive power at the PCC

The oscillation of the reactive power will affect to the grid voltage and make the fault to be more serious. Thus, the control objective is to eliminate this oscillation by generating the unbalanced current from the MMC-HVDC system. A condition must be satisfied as follows.

$$Q_{\sin2\_k} = Q_{\cos2\_k} = 0 \tag{151}$$

The references of the positive and negative sequence currents are derived from (142) as

$$i_{d\_k}^{+*} = -\frac{2v_{sq\_k}^+ Q_k^*}{3\left(v_{sq\_k}^{+2} - v_{sd\_k}^{-2} - v_{sq\_k}^{-2}\right)} \tag{152}$$

$$i_{q\_k}^{+*} = \frac{2v_{sq\_k}^+ P_k^*}{3\left(v_{sq\_k}^{+2} + v_{sd\_k}^{-2} + v_{sq\_k}^{-2}\right)} \tag{153}$$

$$i_{d\_k}^{-*} = \frac{2v_{sq\_k}^- Q_k^*}{3\left(v_{sq\_k}^{+2} - v_{sd\_k}^{-2} - v_{sq\_k}^{-2}\right)} + \frac{2v_{sd\_k}^- P_k^*}{3\left(v_{sq\_k}^{+2} + v_{sd\_k}^{-2} + v_{sq\_k}^{-2}\right)} \tag{154}$$

$$i_{q\_k}^{-*} = -\frac{2v_{sd\_k}^- Q_k^*}{3\left(v_{sq\_k}^{+2} - v_{sd\_k}^{-2} - v_{sq\_k}^{-2}\right)} + \frac{2v_{sq\_k}^- P_k^*}{3\left(v_{sq\_k}^{+2} + v_{sd\_k}^{-2} + v_{sq\_k}^{-2}\right)} \tag{155}$$

In this case, the MMC-HVDC system also injects the unbalanced current into the power system as shown in Fig. 49(a). The current in phase C is increased by 73% which can trip the protection devices. By transforming the three-phase output current into dq-frame, it can be seen that the q-axis positive sequence current is increased by 20% (Fig. 49 (b)). This ensures that the oscillation of the reactive power is eliminated effectively as expressed in Fig. 49(e). The active power is still oscillating during the fault because the presence of the negative sequence current. There is an oscillation in the DC-link voltage (Fig. 49(h)). However, it is

69

not significant.
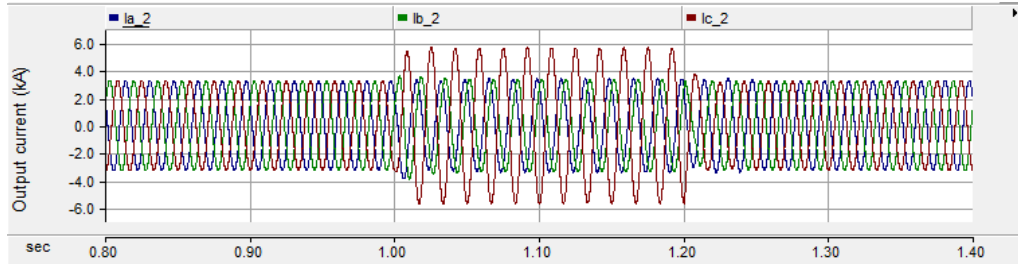
(a) Three-phase output current of MMC-2
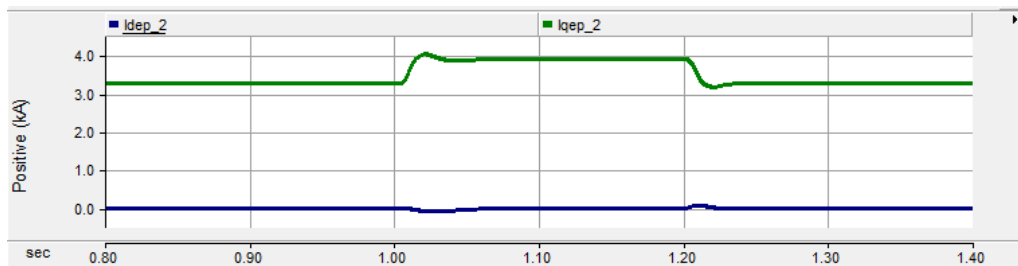
(b) dq-axis positive sequence currents of MMC-2

(c) dq-axis negative sequence currents of MMC-2

(d) Active and reactive powers of MMC-2
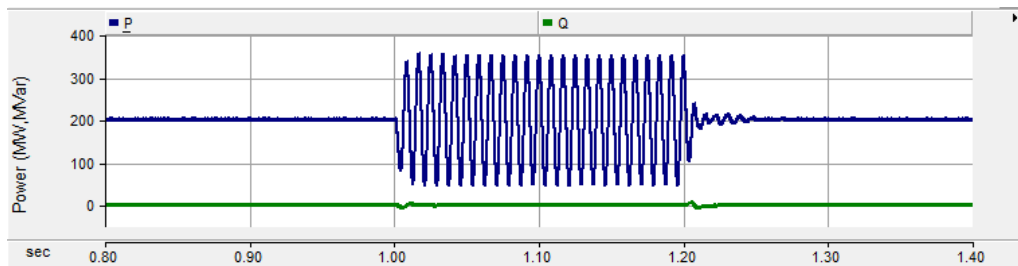
(e) Active and reactive powers at the PCC

Fig. 49 Eliminating oscillation of the reactive power at the PCC

70
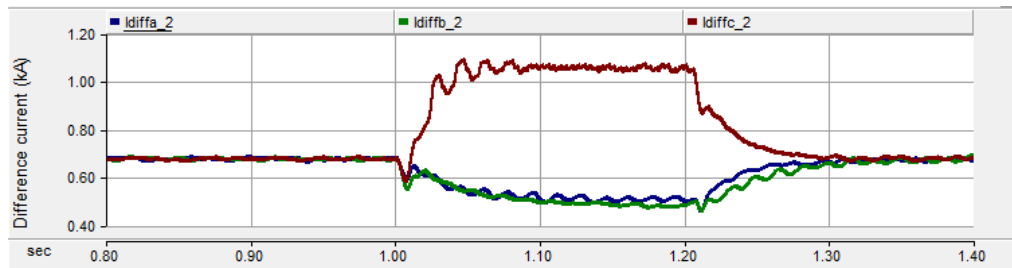
(f) Inner difference currents of MMC-2
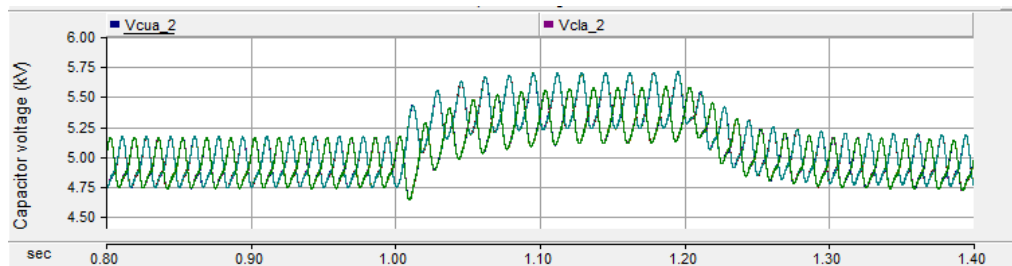
(g) Capacitor voltages of the submodules in MMC-2

(h) DC-link voltage

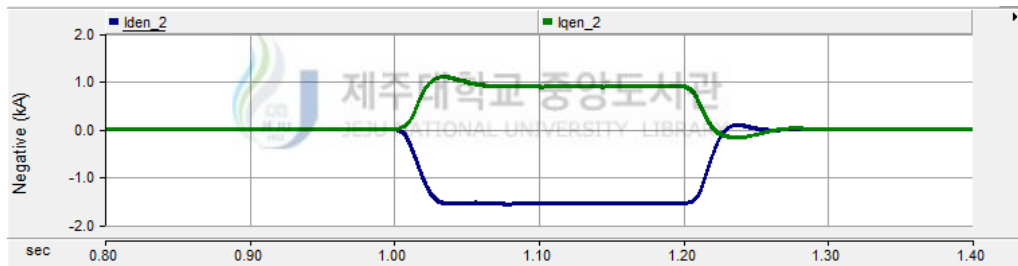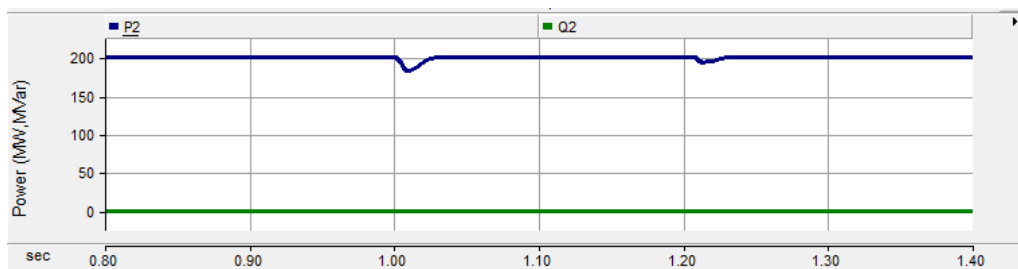Fig. 49 Eliminating oscillation of the reactive power at the PCC (cont.)

3.2.4 Current control with PR controller

A process of controlling a signal in the three-phase system is often performed as follows. The feedback variables are measured and transformed into the dq-frame. Then, the PI controller is applied to eliminate the steady-state error. Moreover, a decomposition of positive and negative sequence components is necessary under unbalanced voltage conditions. This is complicated because the use of a filter introduces delay time and many more PI controllers are required. A development of a new simple controller is essential. Recently, a PR controller has been introduced to control the system under unbalanced voltage conditions [21]. Basically, the PR controller controls the AC signals in the abc-frame or αβ-frame. Each signal can be treated as a single-phase system because there are no cross-coupling terms. As demonstrated in [21], the PR controller can compensate for both positive

71

and negative sequence components. This is because the signals in the αβ-frame only have a frequency of ω under unbalanced voltage conditions. By using the PR controller, the decomposition of positive and negative sequence components into the dq-frame is not necessary, and the control system will be more simple.

A PR controller is a combination of a proportional regulator and a resonant controller. The transfer function of the ideal PR controller at a frequency of ω is expressed by

$$G_{PR} = K_p + \frac{K_i s}{s^2 + \omega^2} \tag{156}$$
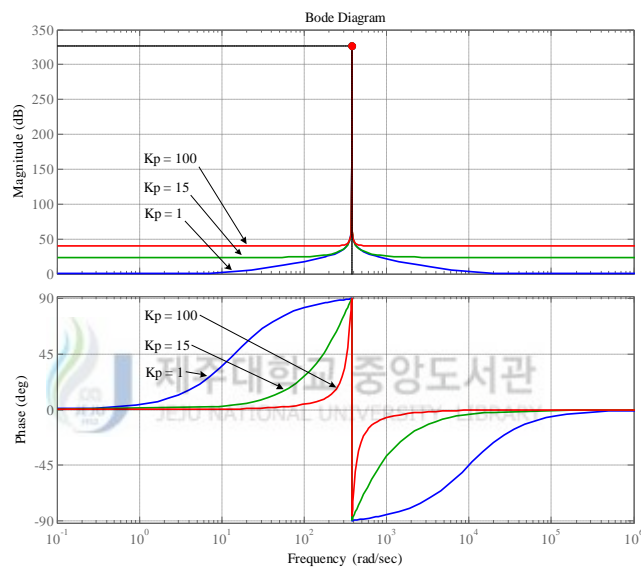
(a) Changing K_p, Fixing K_i
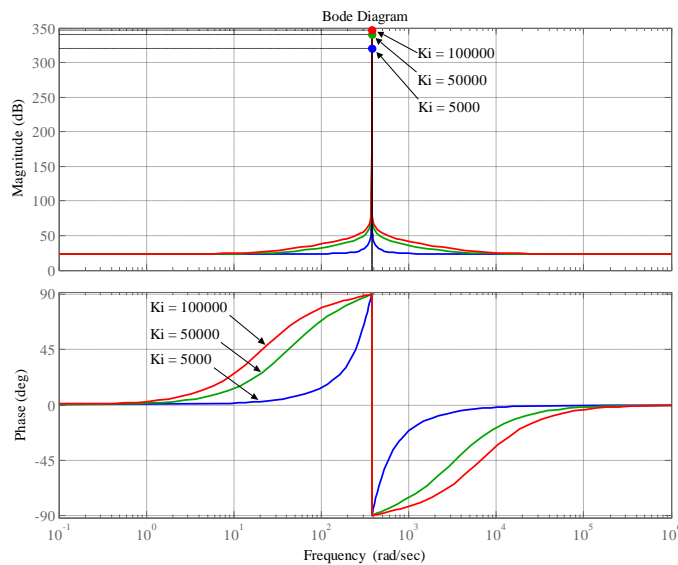
(b) Changing K_i, Fixing K_p

Fig. 50 Bode plots of the PR controller

K_p is the proportional gain that is tuned as the same way for the PI controller. K_r is resonant gain which can be adjusted for shifting the magnitude response vertically. The magnitude and phase responses of the PR controller are shown in Fig. 50. The magnitude response of the PR controller is very high, tend to infinity, at the resonant frequency. This is important to enforce the steady-state error to zero. The magnitude response of the PR controller is increasing with the increase of the value of K_p as seen in Fig. 50(a). However, the resonant peak is remained at the same value. A small value of K_i gives a low resonant peak, whereas a high value of K_i gives a higher resonant peak (Fig. 50(b)).

From above analysis, the PR controller can be used to control the current in the MMC-HVDC system in both balanced and unbalanced voltage conditions [47]. The current controller is achieved by transforming (79) into the αβ-frame as

$$v_{t\alpha\_k}^* = -G_{PR}\left(i_{\alpha\_k}^* - i_{\alpha\_k}\right) + v_{s\alpha\_k} \tag{157}$$

$$v_{t\beta\_k}^* = -G_{PR}\left(i_{\beta\_k}^* - i_{\beta\_k}\right) + v_{s\beta\_k} \tag{158}$$

The control diagram of the current under unbalanced voltage conditions with the PR controller is shown in Fig. 51.

The operation of the MMC-HVDC system with the PR current controller is shown in Fig. 52 and Fig. 53. Because the PR controller has the ability for compensating the negative sequence current, the three-phase output current is in equilibrium. The operation in this case is similar to the Subsection 3.2.3.1. The difference is that there are only two PR current controllers instead of four PI current controllers. The decomposition of three-phase current into positive and negative sequence components is not necessary. Thus, the control method is more simple.
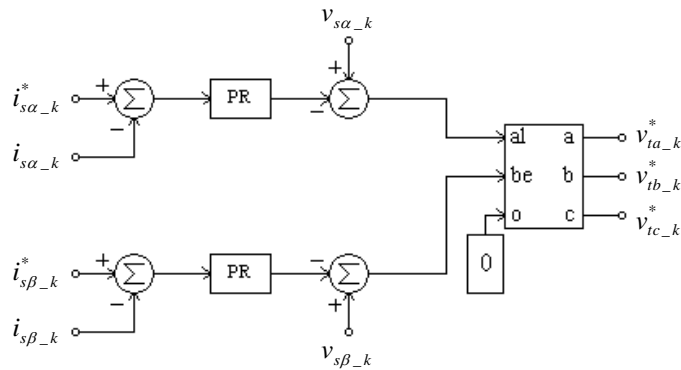
Fig. 51 Control diagram of the current with the PR controller
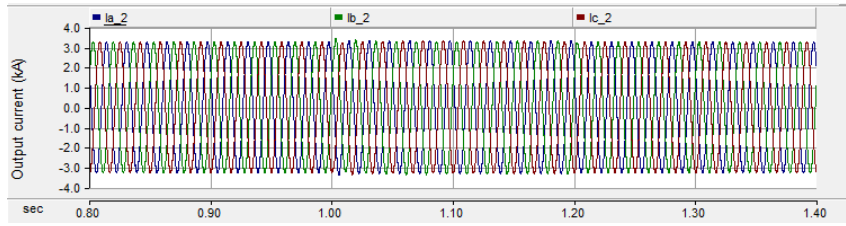
(a) Three-phase output current of MMC-2
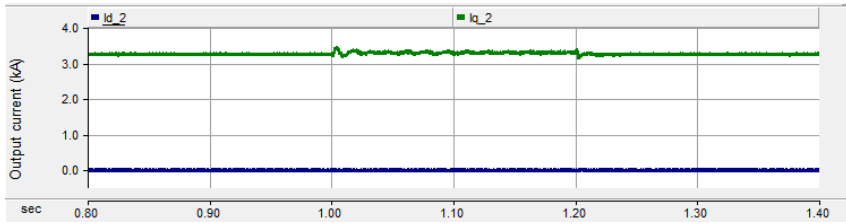
(b) dq-axis output currents of MMC-2
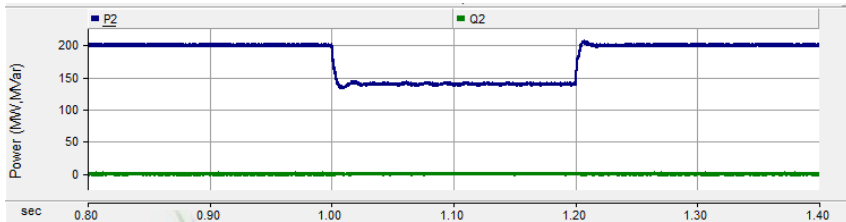
(c) Active and reactive powers of MMC-2
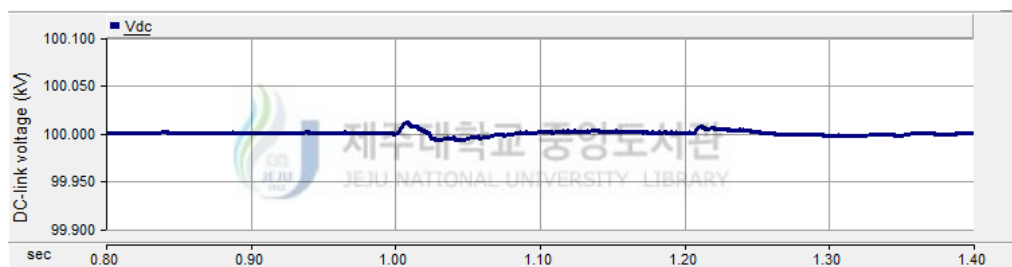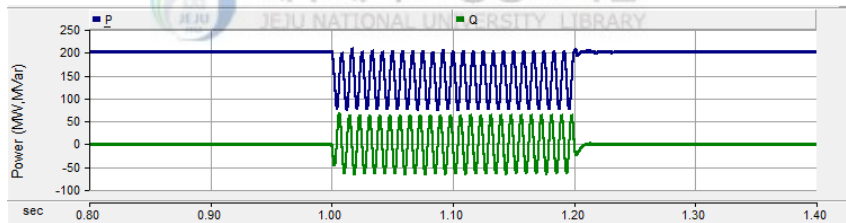

(d) Active and reactive powers at the PCC
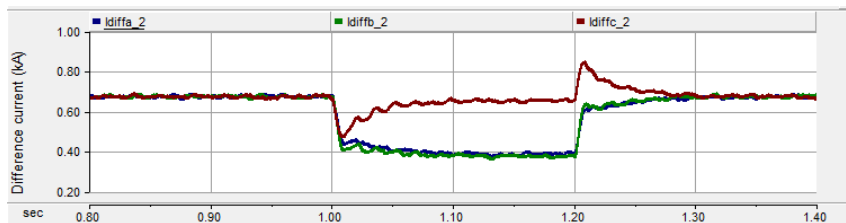
(e) Inner difference currents of MMC-2
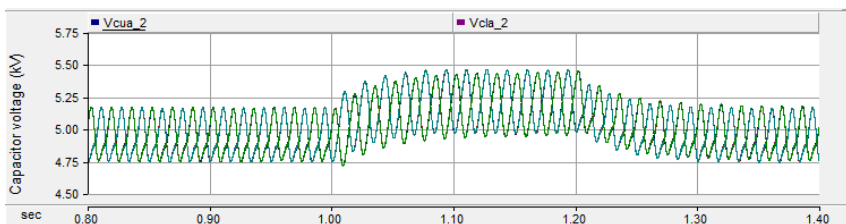
(f) Capacitor voltages of the submodules in MMC-2

Fig. 52 Eliminating negative sequence current with PR controller - MMC-2 side
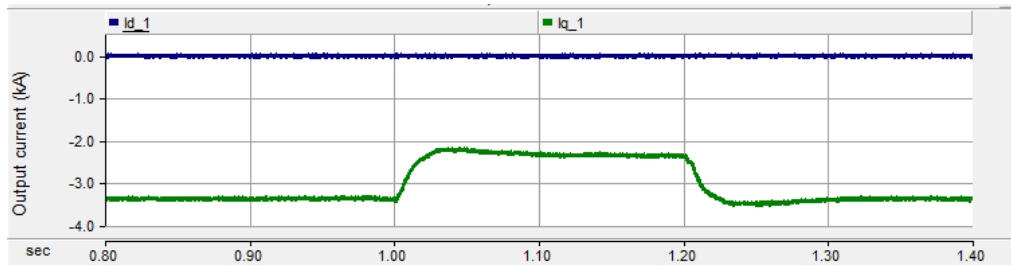
(a) dq-axis output currents of MMC-1
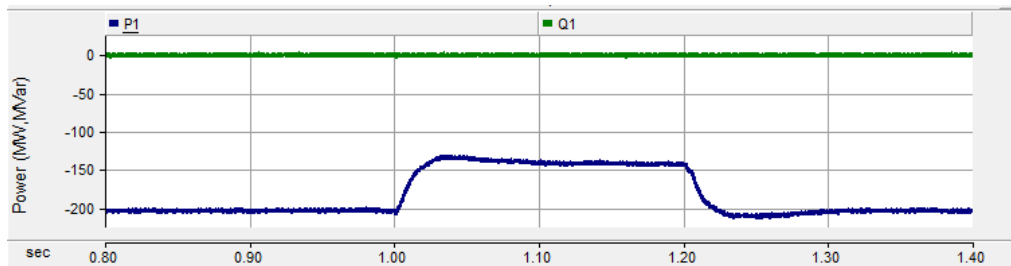
(b) Active and reactive powers of MMC-1
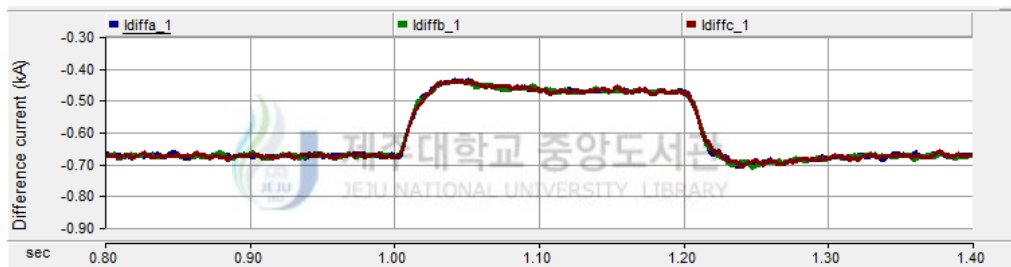
(c) Inner difference currents of MMC-1
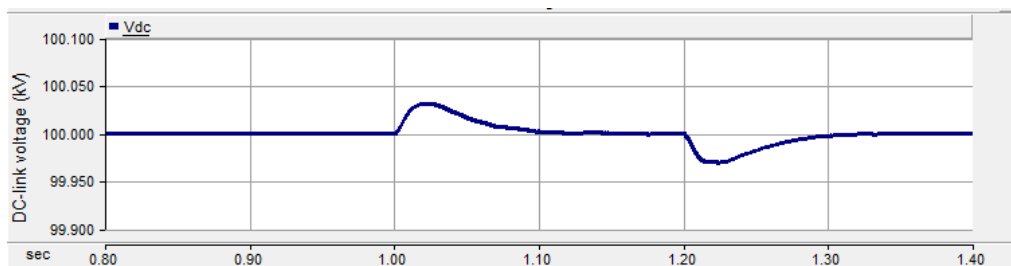
(d) DC-link voltage
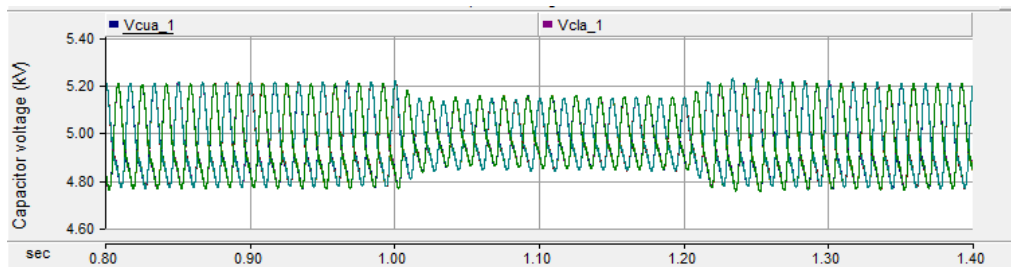
(e) Capacitor voltages of the submodules in MMC-1

Fig. 53 Eliminating negative sequence current with PR controller - MMC-1 side

3.3 Control of the MMC-HVDC system under DC fault

In the VSC-HVDC system, a cable is commonly used because the probability of fault is low. However, the use of the cable will be limited in the area such as mountain. Thus, an overhead transmission line is chosen as an alternative in this area. Once insulation of the DC cable is broken, a fault will be occurred and considered as a permanent fault. The faults on the overhead transmission line may be a permanent or nonpermanent fault. The lightning strikes or air pollution can cause an instantaneous insulation breakdown between two conductors, thus a short circuit fault will occur on the DC transmission line because of the discharging (or arc) phenomenon. The DC arc on the short circuit point is only extinguished when the DC short circuit current is decayed to zero. In these cases, the protection devices such as AC circuit breakers (CBs) or DC CBs must be tripped to protect for the HVDC system, and the system can only be back to normal operation after the fault is cleared completely. Once the CBs are tripped, it takes a little time to restart the system. This causes instability in a long duration. While the nonpermanent DC faults can be extinguished and the insulation can be restored, a trip of the CBs is an unexpected situation.

In the MMC-HVDC system, if the nonpermanent fault occurs on the DC transmission line, all IGBTs should be switched off during fault [48]. This is to protect for the IGBTs to high fault current. In this case, the MMC operates as an uncontrolled rectifier. The fault current will flow through the diodes D_2 and back to the AC side as shown in Fig. 54. If the fault current is high enough, the diode will be damaged. To solve this problem, the bidirectional thyristor switches can be used as shown in Fig. 55 [49]. Both thyristors are connected in parallel with the diode D_2 and controlled by the same gating signal. During normal operation, two thyristor switches are switched off. As soon as the nonpermanent DC fault occurs, the thyristor switches are switched on to protect for diode D_2 and extinguish the DC fault current. Once the thyristor switches are switched on, the SM will be bypassed. Six arms of the MMC become six R-L branches, and the DC fault will become an AC fault. The configuration of the MMC-HVDC system in this case is expressed in Fig. 56. The equivalent resistance of the thyristor switches in one arm is represented by R_0. The upper arm voltages can be expressed by

$$R_0 i_{ua} + L_0 \frac{di_{ua}}{dt} = \frac{v_{dc}}{2} - v_{ta} \tag{159}$$

$$R_0 i_{ub} + L_0 \frac{di_{ub}}{dt} = \frac{v_{dc}}{2} - v_{tb} \tag{160}$$

$$R_0 i_{uc} + L_0 \frac{di_{uc}}{dt} = \frac{v_{dc}}{2} - v_{tc} \tag{161}$$

where v_{dc} is the DC-link voltage under DC fault.
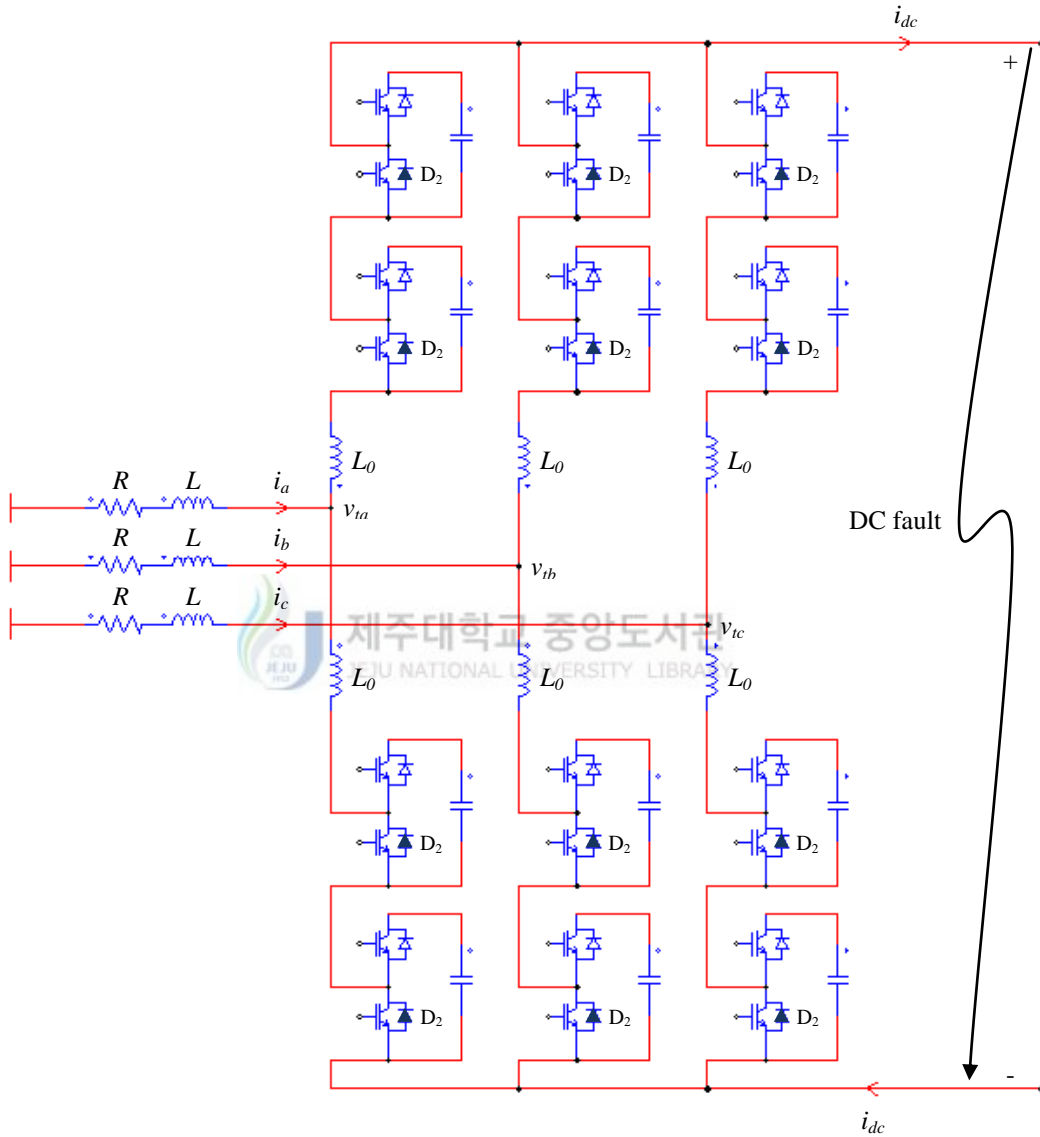
Fig. 54 Circuit diagram of the MMC under DC fault
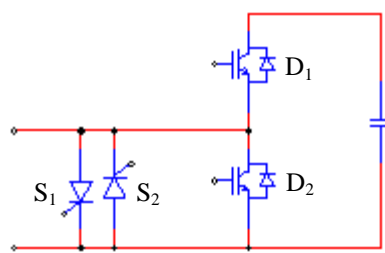
Fig. 55 Submodule with bidirectional thyristor switches
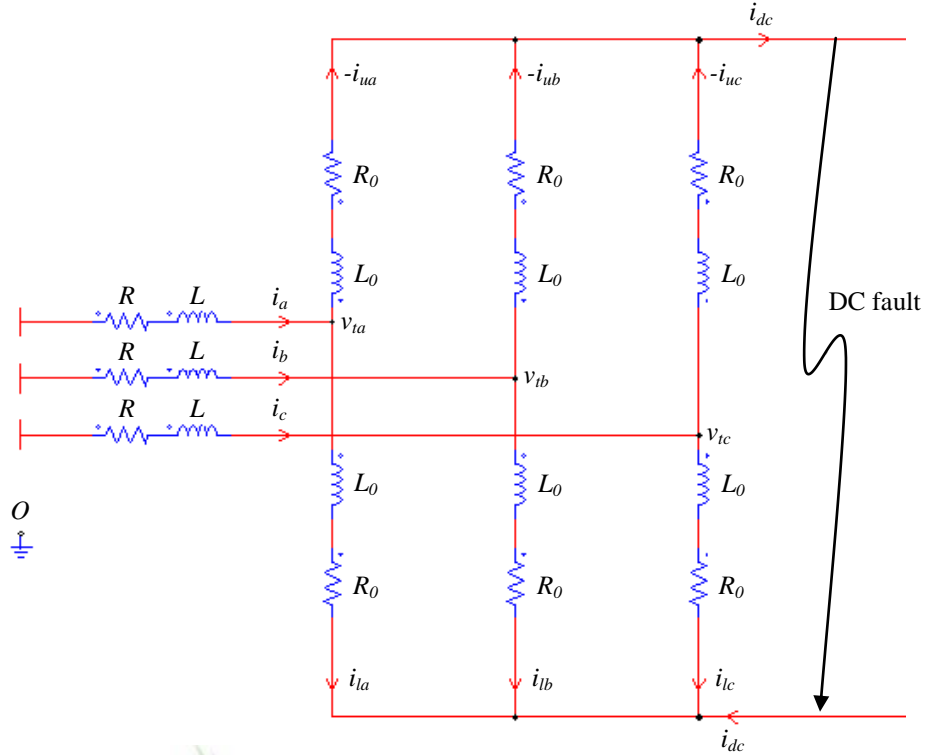
Fig. 56 Equivalent circuit diagram of MMC during the DC fault with bidirectional thyristor switches in the submodule

By summing (159)-(161), we obtain

$$R_0(i_{ua} + i_{ub} + i_{uc}) + L_0\frac{d(i_{ua} + i_{ub} + i_{uc})}{dt} = 3\frac{v_{dc}}{2} - (v_{ta} + v_{tb} + v_{tc}) \qquad (162)$$

If the three-phase system is balanced, the total of three phase voltages will be zero. It means that

$$v_{ta} + v_{tb} + v_{tc} = 0 \qquad (163)$$

By using the bidirectional thyristor switches under DC fault condition, the DC current can be written as

$$i_{dc} = -(i_{ua} + i_{ub} + i_{uc}) \qquad (164)$$

Substituting (163)-(164) into (162) and rearranging this equation, we get

$$v_{dc} = -\frac{2}{3}\left[R_0 i_{dc} + L_0 \frac{di_{dc}}{dt} \right] \qquad (165)$$

Under the DC fault, the DC-link voltage can also be written by

$$v_{dc} = R_f i_{dc} + L_f \frac{di_{dc}}{dt} \qquad (166)$$

where R_f and L_f are the resistance and inductance of the DC fault current path.

Subtracting (165) from (166), the dynamic of the DC current can be formed as

$$\frac{di_{dc}}{dt} + \frac{R_f + \frac{2}{3}R_0}{L_f + \frac{2}{3}L_0} i_{dc} = 0 \qquad (167)$$

By solving (167), the DC current can be found as

$$i_{dc} = I_0 e^{-(t-t_0)/\tau} \qquad (168)$$

where I_0 is the DC current at the time t_0 when the thyristor switches are switched on. τ denotes the time constant which is described by

$$\tau = \frac{L_f + \frac{2}{3}L_0}{R_f + \frac{2}{3}R_0} \qquad (169)$$

The DC fault current in (168) is a damping current to the time. It means that the fault current will be decayed to zero. If the DC fault is the nonpermanent fault, the DC arc will be extinguished, and the insulation on the transmission line will be restored.

The operation modes of the MMC-HVDC system with this control method are explained as follows.

Normal operation: All thyristor switches are switched off. The MMC-HVDC system transfers the power normally.

Protection: As soon as the DC fault is detected, all thyristor switches are switched on and all IGBTs are switched off.

Automatic recovery: As soon as the DC fault current is cleared, all thyristor switches are switched off. The AC short circuit current is removed after a fundamental frequency period.

After the DC-link voltage is restored (around one fundamental frequency period), all IGBTs are back to the normal operation.

A simulation is set up to evaluate the effectiveness of the above analysis. The parameters of the MMC-HVDC system are given in Table 3. To improve the simulation time, the simulation results are only performed for one MMC. The other MMC is modeled as a DC resistor. The conditions of the simulation are as follows. The MMC-HVDC system is operating with the active power of 200 MW. At t = 0.5 s, a nonpermanent fault occurs on the DC transmission line. The resistance of the DC fault current path is assumed to 2 Ω. The simulation results are shown in Fig. 57. The three-phase output voltage is balanced as expressed in Fig. 57(a). At t = 0.5 s, the DC-link voltage is dropped down to zero because of the fault (Fig. 57(b)). To detect the fault, the DC current is compared to an activating threshold I_{act}. If the DC current is higher than the I_{act}, the MMC will move to the "protection" mode. If the DC current is smaller than a restoring threshold I_{res}, the MMC will move to the "automatic recovery" mode. In this simulation, the I_{act} is set to $1.5I_{dc\_nom}$ and I_{res} is set to $0.005I_{dc\_nom}$ (I_{dc_nom} is the nominal DC current). At t = 0.54582 s, the DC fault current is cleared ($I_{dc\_fault} < 0.005I_{dc\_nom}$) as seen in Fig. 57(c), and the gating signals of the thyristor switches are removed. As soon as the DC arc is extinguished, the insulation on the short circuit point will be restored. 16.67 ms after the DC fault is cleared (at t = 0.56249 s), all IGBTs are back to the normal operation. With the bidirectional thyristor switches, the nonpermanent DC fault will become the AC short circuit fault, and the DC fault current is extinguished quickly. It takes about 65 ms to clear DC fault. The three-phase output current and the arm currents are increased under fault as shown in Fig. 57(d)-(e). During the fault, the thyristor S_2 will share the short circuit current to diode D_2, thus the diode D_2 is protected as seen in Fig. 57(f)-(g).

Table 3. Parameters of the MMC-HVDC system - DC fault

Quantity	Value
Active power	200 MW
Reactive power	100 MVar
AC voltage	154 kV
Nominal frequency	60 Hz
Transformer ratio	154 kV/50 kV
DC-link voltage	±50 kV
Number of SMs per arm	10
Arm inductance	0.0035 H
SM capacitance	3900 μF
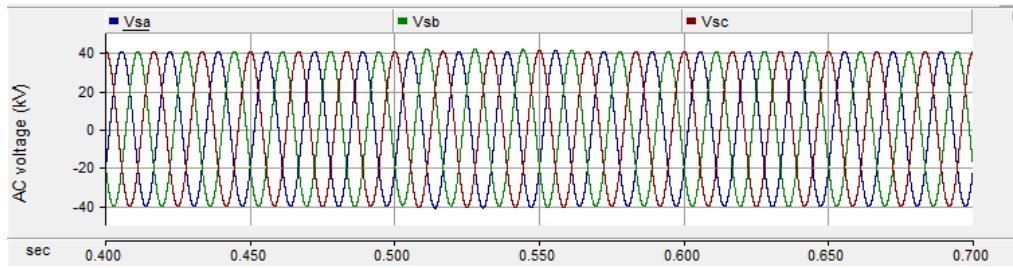
(a) Three-phase grid voltage
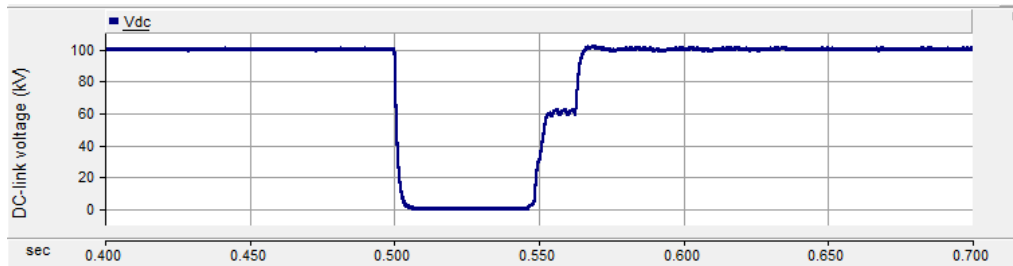
(b) DC-link voltage
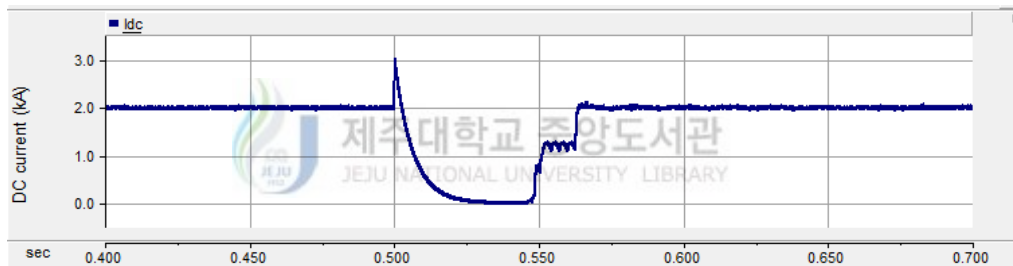
(c) DC current
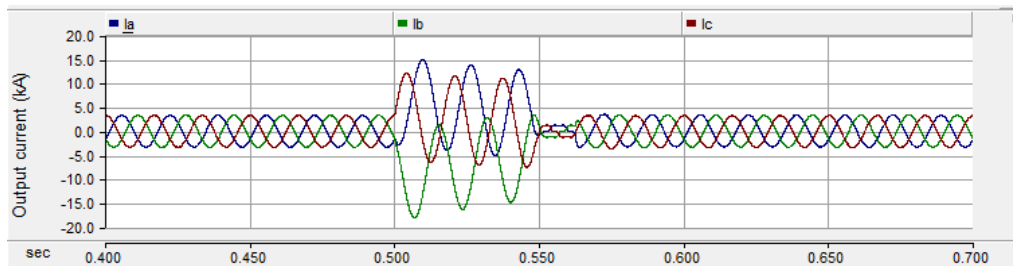
(d) Three-phase output current
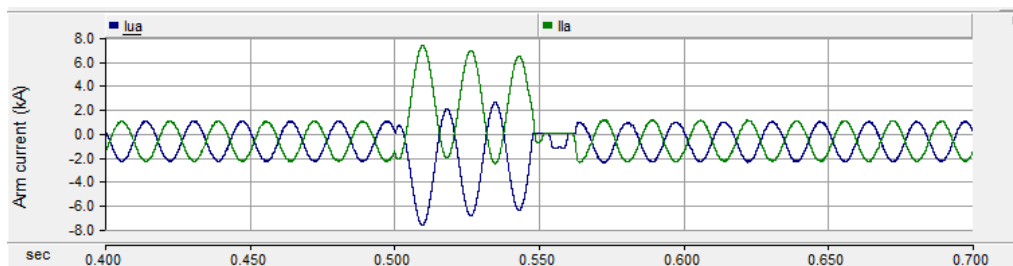
(e) Upper and lower arm currents of phase A

Fig. 57 Operation of the MMC-HVDC under nonpermanent DC fault

(f) Diode current

(g) Thyristor currents

Fig. 57 Operation of the MMC-HVDC under nonpermanent DC fault (cont.)

Chapter 4. Application of the MMC-HVDC System to the Jeju Island Power System

4.1 Overview of the Jeju Island power system

At present, the Jeju Island power system consists of two LCC-HVDC systems (HVDC #1 and HVDC #2), two Statcom systems, wind farms, thermal power plants, transformers, transmission and distribution lines. The main power source in Jeju Island focuses on the wind farms because Jeju Island has the highest average wind speed among all promising sites in Korea. The annual wind speed in the east and west areas of Jeju Island is estimated about 7~8 m/s [50], [51]. This is the reason why many companies are investigating to build wind farms in these areas. The total installed capacity of the wind farms in 2014 is about 114.6 MW. But the output power of the wind farms is not stable, and it depends on the wind velocity. Thus, the power system needs the support of the thermal power plants and the LCC-HVDC systems which generate both the active and reactive powers. However, the reactive power of the LCC-HVDC systems relates strictly to the active power (it is about 60% of the active power), and it is almost constant. The random change of the load causes the voltage ripple in the power system. This can reduce the lifetime or damage the electrical devices. To solve this problem, the Statcom systems have been installed in the Sinjeju and Halla sub-stations, respectively. The detail of the power generating sources and wind farms in Jeju Island is shown in Table 4 and Table 5, respectively.
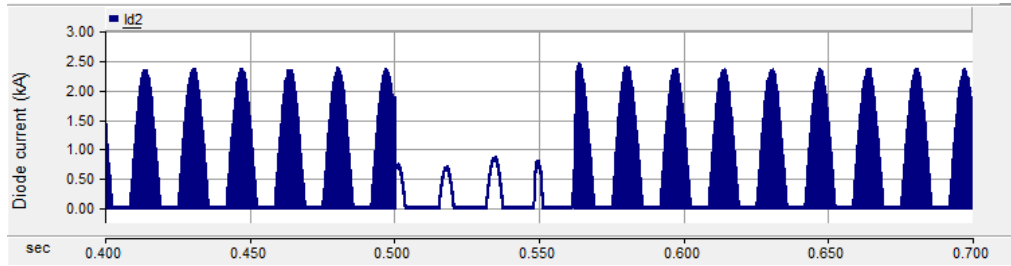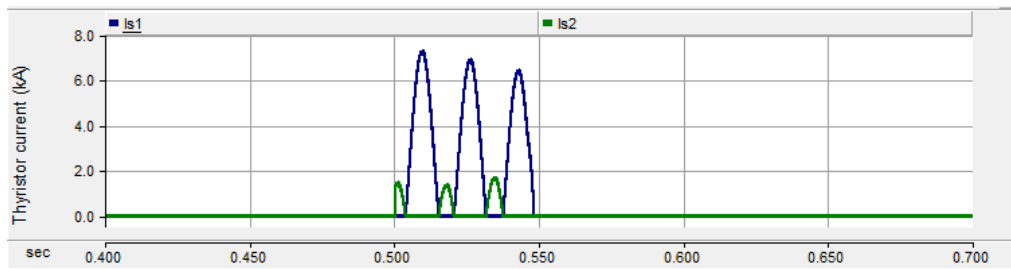
The modeling of the Jeju Island power system that is established based on the parameters and measured data from the real Jeju Island power system is presented in Fig. 58. Because the wind farms almost concentrate on the east and west sides of Jeju Island, thus these wind farms are represented by the 'East Wind Farm' and the 'West Wind Farm'. The wind farms and HVDC systems will supply the power to the demand load. In other words, they will inject a three-phase current into the power system in response to the current demand of the load. Therefore, these wind farms and the HVDC systems will be modeled by controlled-current sources. Fig. 59 shows the representative model of the HVDC #2. The other ones are similar. The thermal power plants are modeled by the block of synchronous machine in PSCAD/EMTDC library as shown in Fig. 60.

Table 4. Power generating sources in the Jeju Island power system

No.	Generation source	Installed capacity (MW)	Operating range		Ramp rate (MW/min)
			Minimum (MW)	Maximum (MW)	
1	Jeju T/P #2	75	45	79	1
2	Jeju T/P #3	75	45	79	1
3	Jeju D/P #1	40	28	40	1.2
4	Jeju D/P #2	40	28	40	1.2
5	Jeju G/T #3	55	16	44	5
6	Namjeju T/P #1	100	50	103	5
7	Namjeju T/P #2	100	50	103	5
8	Hallim C/C	105	41	90	8.7*2
9	Wind Farm	114.6	-	-	-
10	Solar Energy	6.9	-	-	-
11	LFG	2.2	-	-	-
12	Small hydro	0.46	-	-	-
13	Haenam-Jeju HVDC	300	40	150	-
14	Jindo-Jeju HVDC	400	60	250	-

Table 5. Capacity of the wind farms in Jeju Island

No.	Wind farm	Capacity (MW)
1	Hangwon	13.4
2	Hangyeong	21.0
3	Sinchang	1.7
4	Woljeong	1.5
5	Woljeong (offshore)	5.0
6	Seongsan	20.0
7	Samdal	33.0
8	Gimnyeong	1.5
9	Gasiri	15.0
10	Wollyeong	2.0
11	Gapado	0.5
	Total	114.6
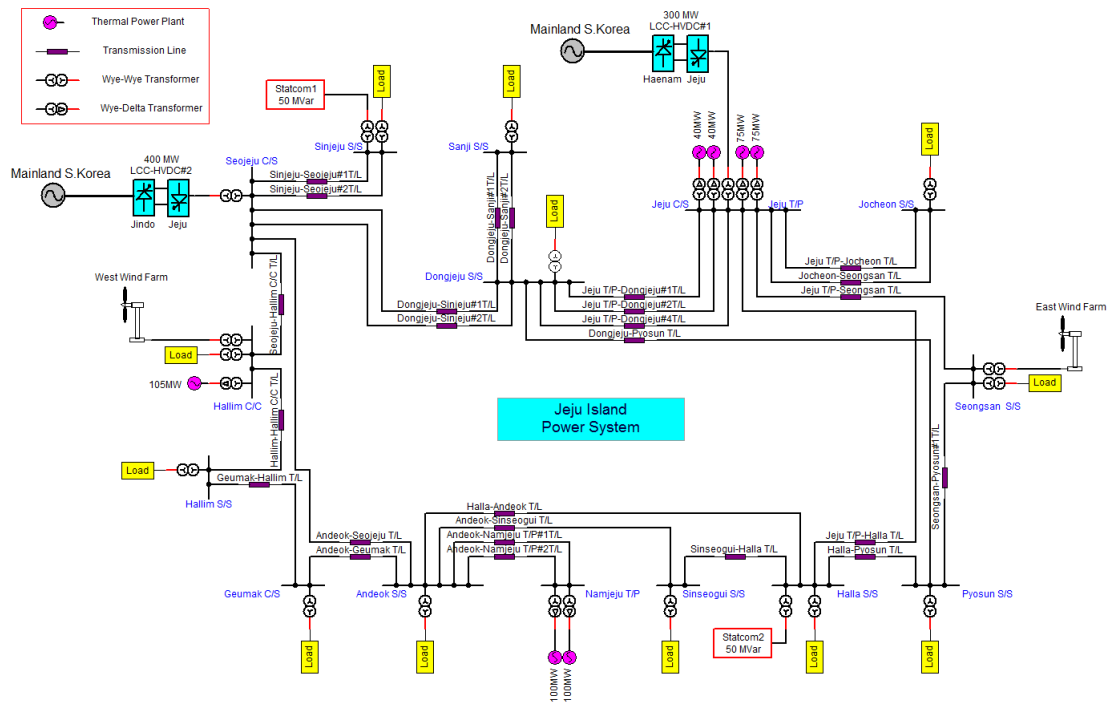
Fig. 58 Modeling of the Jeju Island power system

Fig. 59 Modeling of the HVDC #2

Fig. 60 Modeling of the thermal power plant

4.2 MMC-HVDC system for regulating grid voltage based on the Jeju Island power system

As introduced in Section 4.1, the voltage ripple in the Jeju Island power system will be eliminated by using the Statcoms. However, the voltage ripple can be serious at the transient time because the capacity of the Statcoms is limited. Meanwhile, the responses of the thermal power plants and the HVDC systems are slow. If the MMC-HVDC system is used in the Jeju Island power system, this situation can be improved because it can support the amount of variable reactive power and its response is fast. The ability of regulating the grid voltage of the MMC-HVDC system is similar to the Statcom, and it is shown in Fig. 61 [52]. The load is requiring the reactive power from the power source. This is the common case in the power system. From Fig. 61(a), the source and load currents are calculated by

$$i_s = i_l = i_p + ji_q \tag{170}$$

where i_s and i_l are the source and load currents, respectively. i_p and i_q are the active and reactive currents of load.
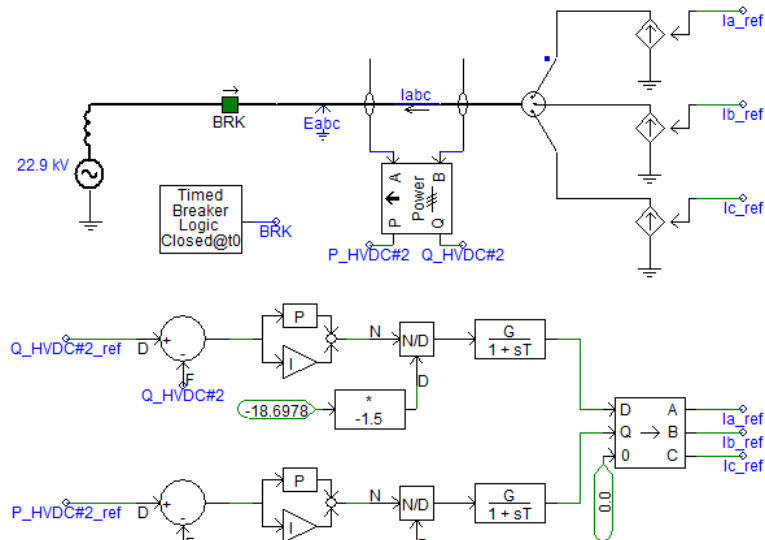
Assuming that the reactive current of the load is compensated by the MMC-HVDC system as shown in Fig. 61(b), the source and load currents can be rewritten as

$$i_s = i_p \tag{171}$$

$$i_l = i_p + ji_c \tag{172}$$

where i_c is compensation current from the MMC-HVDC system.

The source current in (171) is smaller than the source current in (170) because there is only one component of the active current. It means that the power losses in the transmission lines and transformers are reduced by using the MMC-HVDC system. Therefore, the voltage received at the load side will be improved.

The operation of the MMC-HVDC system for regulating the grid voltage is verified by applying it to the Jeju Island power system. In this case, the HVDC #1 is replaced by the MMC-HVDC system. The parameters of the MMC-HVDC system are shown in Table 6.
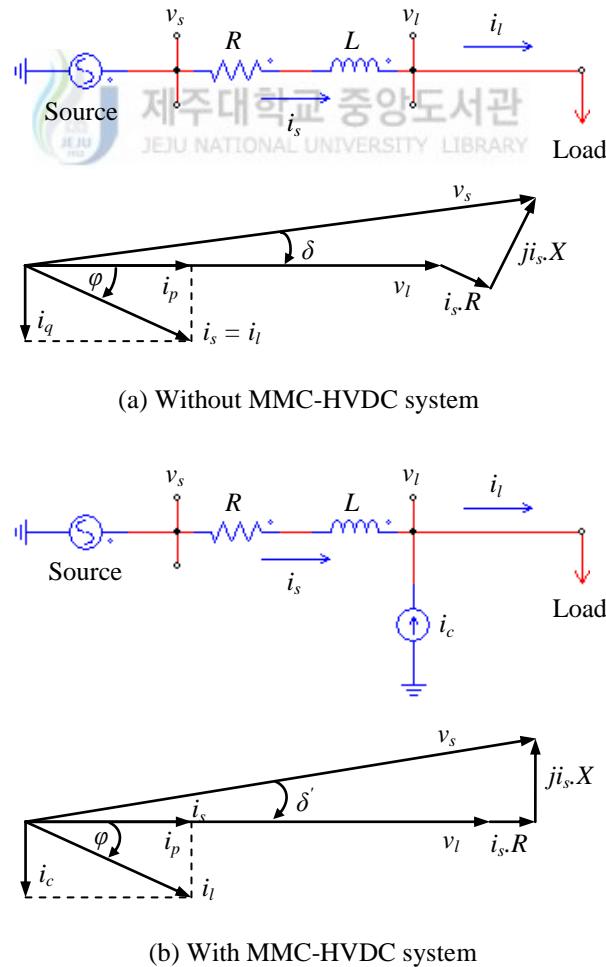

(a) Without MMC-HVDC system

(b) With MMC-HVDC system

Fig. 61 Single-line and vector diagrams of the reactive power compensation

87

Table 6. Parameters of the MMC-HVDC system - Application 1

Quantity	Value
Active power	300 MW
Reactive power	140 MVar
AC voltage	154 kV
Nominal frequency	60 Hz
Transformer ratio	160 kV/55 kV
DC-link voltage	±50 kV
Number of SMs per arm	20
Arm inductance	0.0037 H
SM capacitance	9900 μF

The measured results from the real Jeju Island power system on 09/18/2013 are shown in Fig. 62. To get this figure, the measured data from the real Jeju Island power system is saved in the ".txt" files. Then, the blocks "File Read" in the PSCAD/EMTDC simulation program are used to read data from these files.

The output power of the wind farms is small and variable during this day as shown in Fig. 62(a). To response sufficiently the load demand, the LCC-HVDC systems transfer the active power from the mainland to the Jeju Island power system and it is almost constant at each time. In this case, the thermal power plants supply the largest power among the power generating sources. The main reactive power source will come from the filters of the LCC-HVDC systems and thermal power plants as described in Fig. 62(b). The Statcom systems are used to stabilize the voltage ripple in the power system. However, the grid voltage is still a small ripple as shown in Fig. 62(c). In this case, the grid voltage is measured at the Jocheon sub-station. At t = 10h46min, the grid voltage has a large oscillation because the HVDC #2 is activated to supply the power for the system.

In this section, the symbols of the active and reactive powers in figures are defined as follows.

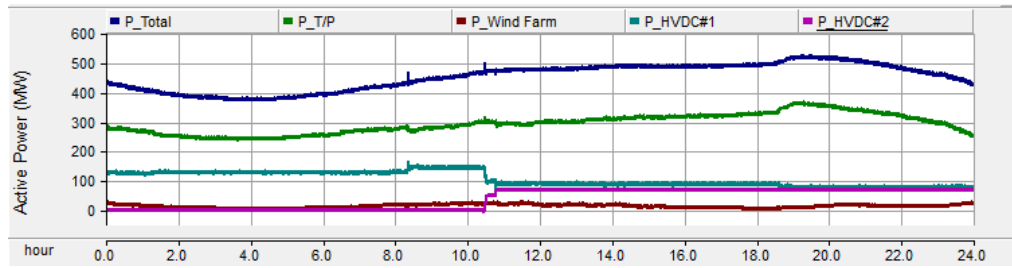P_Total: Total active power of the wind farms, thermal power plants, HVDC #1 and HVDC #2.

P_T/P: Total active power of the thermal power plants.
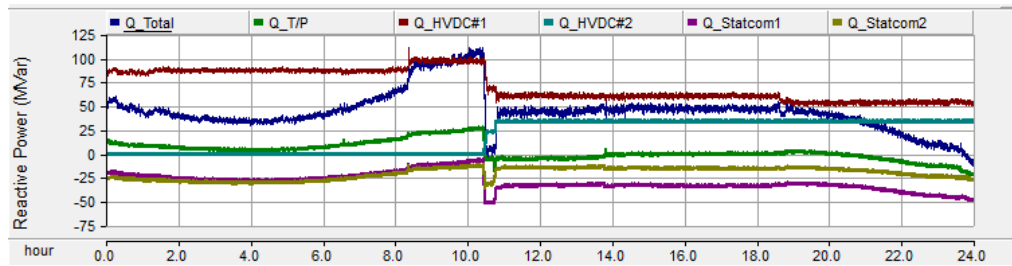
P_Wind Farm: Total active power of the wind farms.

P_HVDC#1: Active power of the HVDC #1.
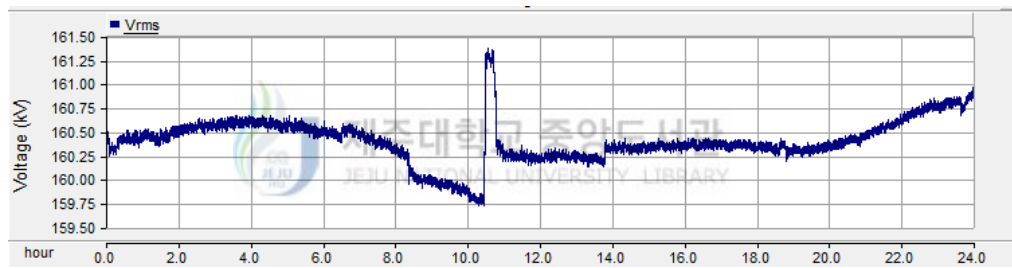
P_HVDC#2: Active power of the HVDC #2.

Q_Total: Total reactive power of the thermal power plants, HVDC #1, HVDC #2, Statcom1 and Statcom2.

(a) Active powers

(b) Reactive powers

(c) Grid voltage

Fig. 62 Measured results of the Jeju Island power system

Q_T/P: Total reactive power of the thermal power plants.

Q_HVDC#1: Reactive power of the HVDC #1.

Q_HVDC#2: Reactive power of the HVDC #2.

Q_Statcom1: Reactive power of the Statcom1.

Q_Statcom2: Reactive power of the Statcom2.

The simulation results of the Jeju Island power system based on the real parameters and measured data are expressed in Fig. 7. It is recognized that the simulation results and the measured data are almost similar. This proves the reliability of the modeling of the Jeju Island power system in PSCAD/EMTDC simulation program.
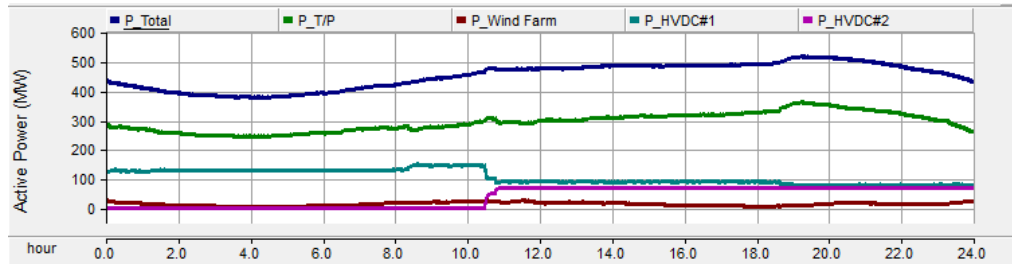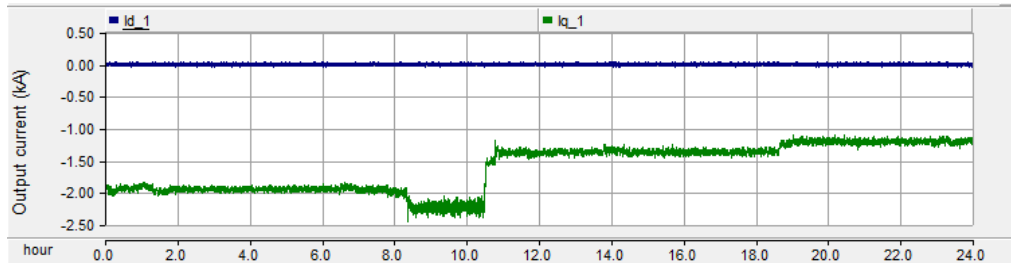
(a) Active powers
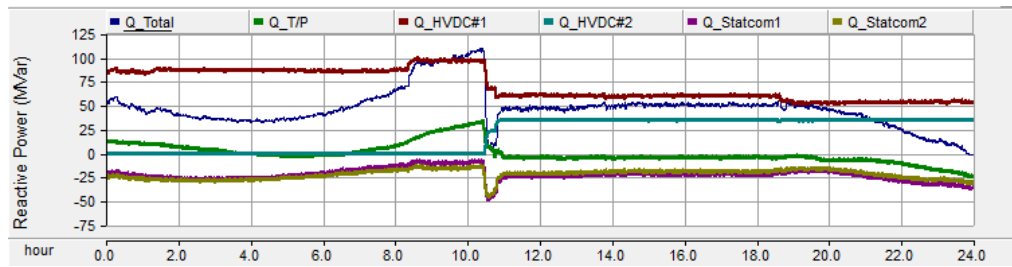
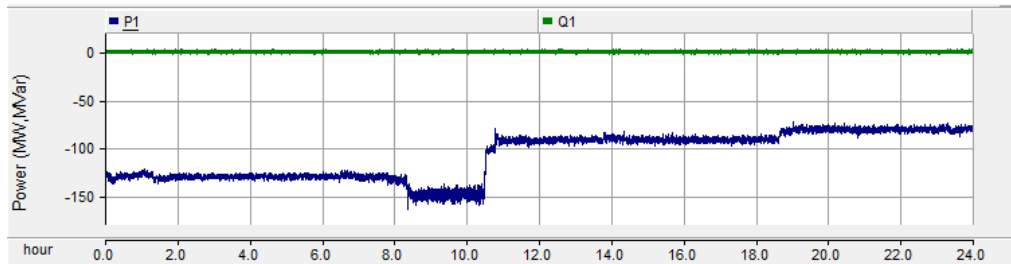(b) Reactive powers
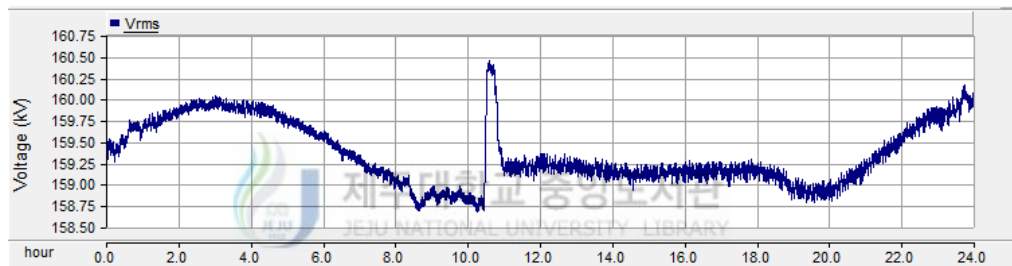
(c) Grid voltage

Fig. 63 Simulation results of the Jeju Island power system

The operation of the MMC-HVDC system in the Jeju Island power system is shown in Fig. 64. The dq-axis output current components of the MMC-1 are expressed in Fig. 64(a). Fig. 64(b) shows the corresponding active and reactive powers. The reactive power is controlled to zero. It means that the MMC-1 is operating at the unit power factor. The active power will depend on the power control in the MMC-2. The DC-link voltage is always kept at its reference value as shown in Fig. 64(c). Fig. 64(d) is the capacitor voltages of the SMs in the MMC-1. It is maintained at their nominal value. The dq-axis output current components of the MMC-2 are shown in Fig. 64(e). Fig. 64(f) illustrates the corresponding active and reactive power flows. The reactive power of the MMC-2 is controlled according to the requirement of the voltage controller. It is not zero in this case. In other words, the MMC-2 is not operating at the unit power factor. The active power is adjusted depending on the power demand of the Jeju Island power system. Fig. 64(g) shows the capacitor voltages of the SMs in the MMC-2.
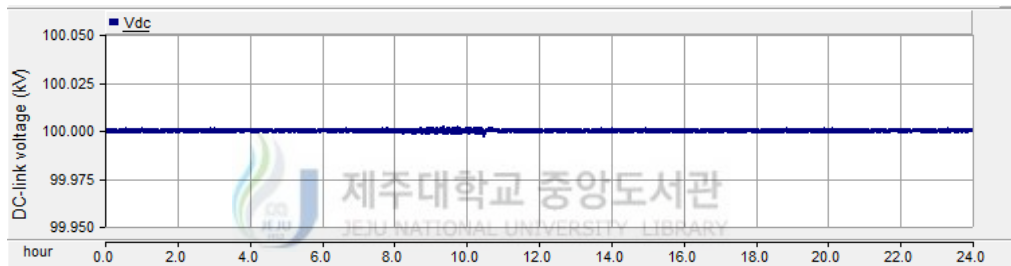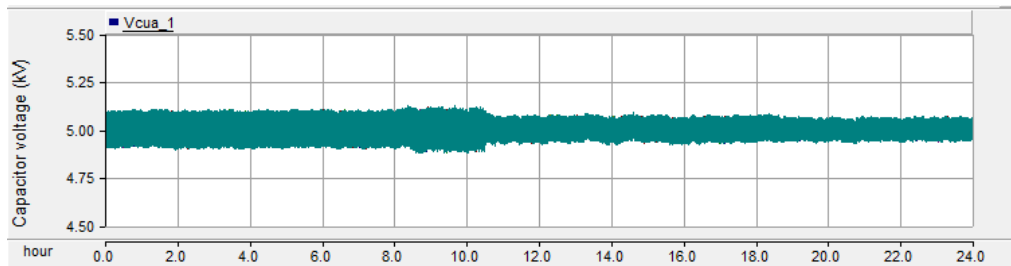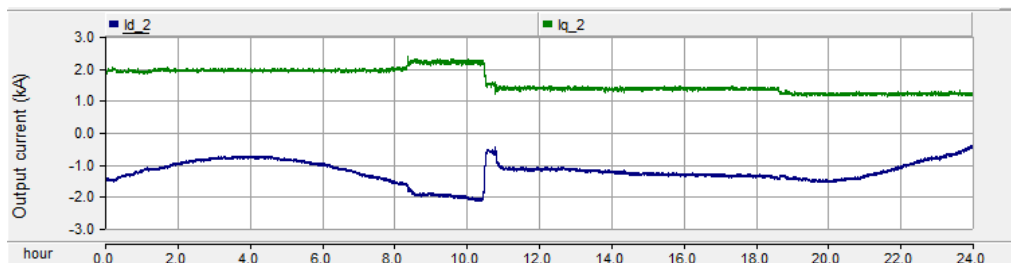
90

(a) dq-axis output currents of MMC-1

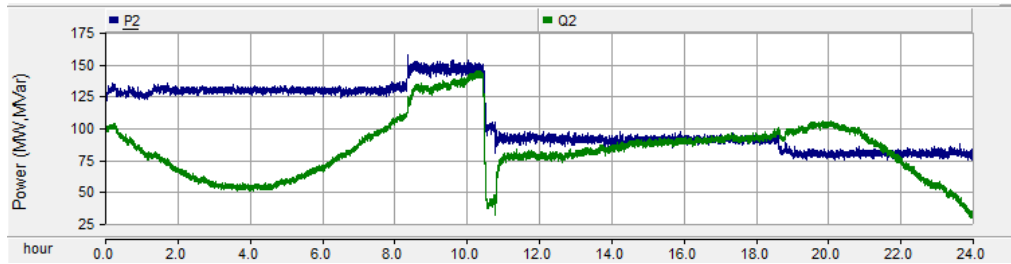(b) Active and reactive powers of MMC-1

(c) DC-link voltage

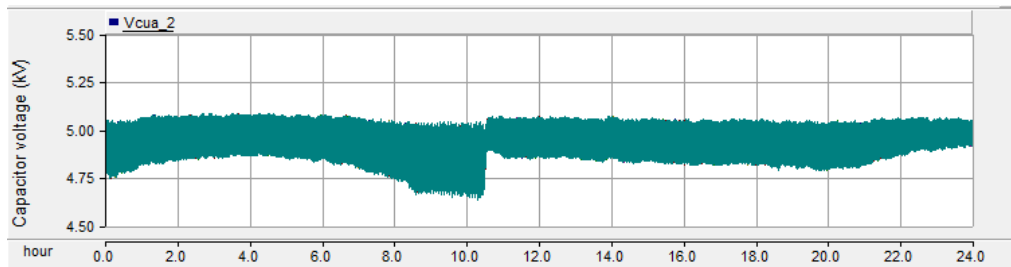(d) Capacitor voltages of the submodules in MMC-1

(e) dq-axis output currents of MMC-2

Fig. 64 The operation of the MMC-HVDC system

(f) Active and reactive powers of MMC-2

(g) Capacitor voltages of the submodules in MMC-2

Fig. 64 The operation of the MMC-HVDC system (cont.)

The operation of the Jeju Island power system with the MMC-HVDC system is shown in Fig. 65. Comparing with and without using the MMC-HVDC system, it is seen that the active powers in Fig. 65(a) are almost same with the active powers in Fig. 63(a). However, the reactive powers are quite different as shown in Fig. 65(b) and Fig. 63(b). This is due to the MMC-HVDC system supplies the reactive power according to the requirement of the grid voltage controller. The reactive powers, which are supplied by the Statcoms, are almost stable. In addition, the peak powers of the Statcoms at the transient time are also smaller. With the implementation of the voltage controller, the grid voltage is more stable as illustrated in Fig. 65(c) and Fig. 63(c). The peak oscillation of the grid voltage at the transient time is reduced significantly. This points out the effectiveness of the voltage controller. The MMC-HVDC system is still operating well while it is supporting for the grid voltage stability. In this case, the using efficiency of the MMC-HVDC system is highest. It not only transfers the active power, but also supports for regulating the grid voltage.

Because of the rapid development of the demand load and wind farms in Jeju Island, the Korean government has a plan to build a new HVDC system which can exchange the active power between the mainland and the Jeju Island power system. With the above analysis, the proposal of using the MMC-HVDC system is quite suitable. Moreover, the installation of a new Statcom is not necessary in this case.
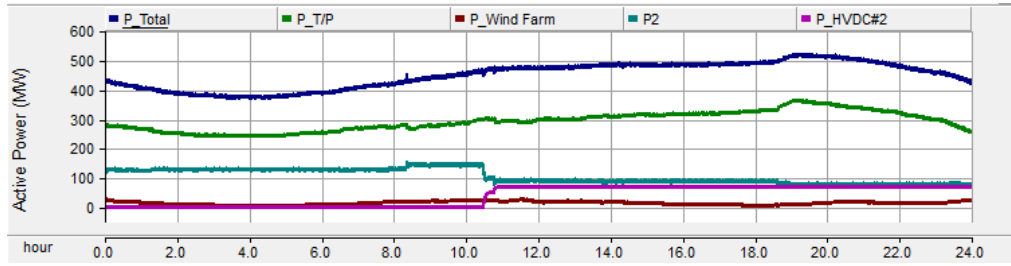
(a) Active powers
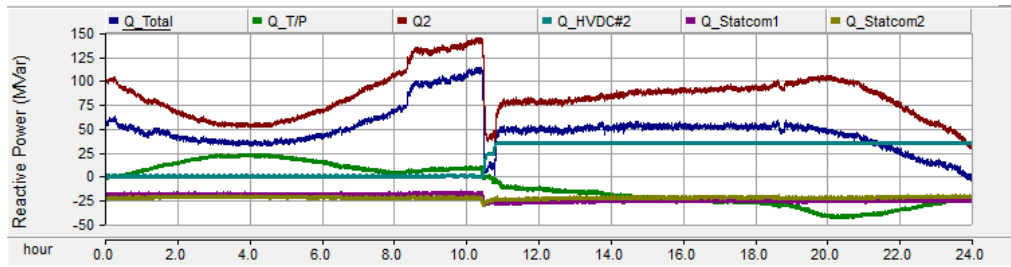
(b) Reactive powers
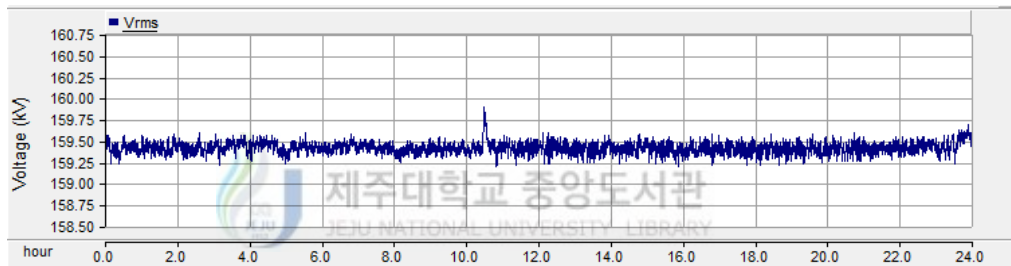
(c) Grid voltage

Fig. 65 The operation of the Jeju Island power system with the MMC-HVDC system

4.3 MMC-HVDC system for stabilizing the Jeju Island power system

As mentioned in Section 4.1, the Jeju Island power system consists of many power generating sources. Hence, it shows that the possibility of electrical fault is high and it will be increased along with the new installation of renewable energy sources. This can cause instability in the Jeju Island power system. As Jeju Island to be a free-trade international province, the demand of reliable electric energy sources is urgently increasing. It is not only the problem of energy supply source, but also the power quality is becoming an important issue to meet the expectation of international standard in building the infrastructures. Moreover, since the island is located in a hurricane's path and is known to have frequent lightnings, there has been frequent contingencies because of the system heavily depending on HVDC tie lines from the mainland Korea and sporadic variable output from many wind farms located in the east and west sides of Jeju Island. At present, two HVDC systems will

93

support for the stability of the Jeju Island power system. Nevertheless, these HVDC systems only operate in one direction, from the mainland to Jeju Island. This will be no longer suitable in the future because the increase of demand load and wind power. Following the data of the Korean government in the winter in 2020, the maximum demand load in Jeju Island is about 944 MW and the wind farms can supply up to 500 MW in total capacity of demand load. Thus, the installation of a new HVDC system, HVDC #3, is really necessary, which can operate in bi-direction (i.e., from the mainland to Jeju Island and from Jeju Island to the mainland) to transfer power between the mainland and the Jeju Island power systems. This section will analyze the stability of the Jeju Island power system in 2020 with the HVDC #3, MMC-HVDC system [53]. The general configuration of the Jeju Island power system in 2020 is shown in Fig. 66.

The power generation will come from wind farms, steam turbines, and two HVDC systems.

$$P_{Total} = P_{Wind\ Farm} + P_{Steam\ Tubine} + P_{HVDC\#1} + P_{HVDC\#2} \tag{173}$$

The HVDC #1 and HVDC #2 will supply a constant power, meanwhile the main function of the MMC-HVDC system is to stabilize for the Jeju Island power system in combining with the adjustment of the wind farm output power and demand load. The parameters of the MMC-HVDC system are shown in Table 7. The overall operation of the system will be tested in three cases.
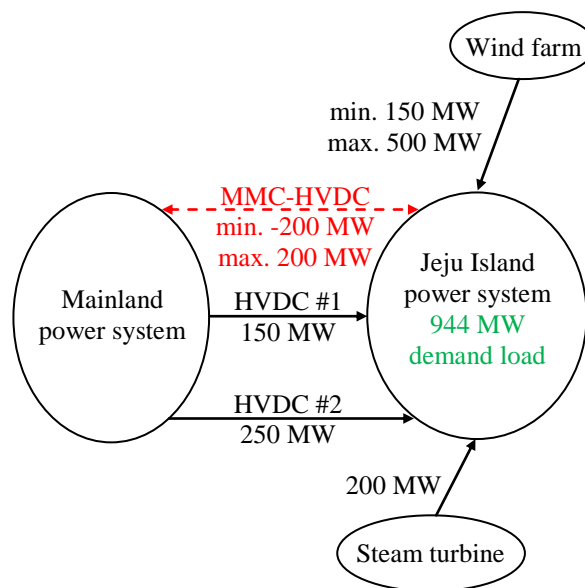

Fig. 66 General configuration of the Jeju Island power system in 2020

Table 7. Parameters of the MMC-HVDC system - Application 2

| Quantity	Value
Active power	200 MW
Reactive power	100 MVar
AC voltage	154 kV
Nominal frequency	60 Hz
Transformer ratio	154 kV/55 kV
DC-link voltage	±50 kV
Number of SMs per arm	20
Arm inductance	0.0046 H
SM capacitance	3300 µF

4.3.1 The variable wind speed

At the normal operation, the powers of the steam turbines, HVDC #1, and HVDC #2 are represented in Fig. 67(a). The most general operation case of the wind farms is its operation under the variable wind speed. In the study case, the output power of the wind farms will be controlled between minimum and maximum values as shown in Fig. 67(b). If the wind farms supply the minimum power of 150 MW, the total power generation will be 750 MW as depicted in Fig. 67(c). This amount of power is less than 944 MW demand load. Thus, the MMC-HVDC system will transfer 944 MW - 750 MW = 194 MW from the mainland to Jeju Island. Similarly, if the output power of the wind farms reaches to maximum value of 500 MW, the total power generation will be 1100 MW. In this case, the MMC-HVDC system will transfer 944 MW - 1100 MW = -156 MW from Jeju Island to the mainland to make a power balancing in the Jeju Island power system. The power and the DC-link voltage of the MMC-HVDC system are shown in Fig. 67(d)-(e), respectively. With the new HVDC system, the power system in Jeju Island is always stable at its demand value. The voltage and the frequency of the Jeju Island power system is almost constant during operation time as described in Fig. 67(f)-(g).
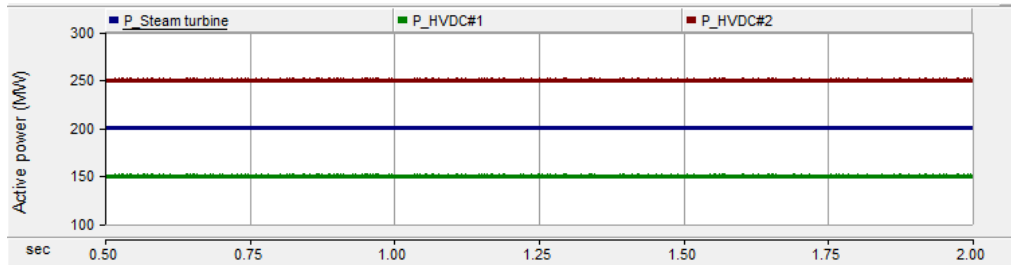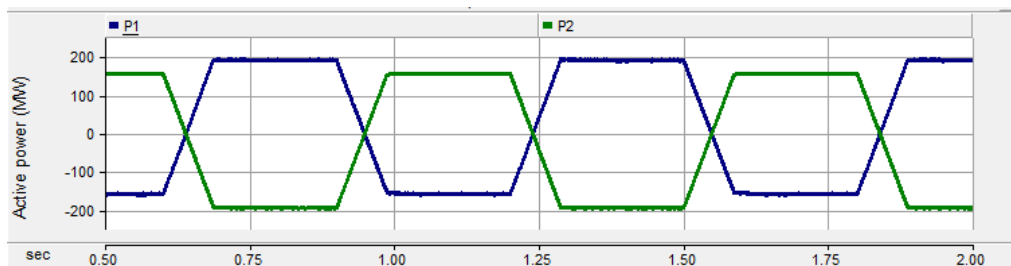
(a) Active powers of steam turbine, HVDC #1, and HVDC #2
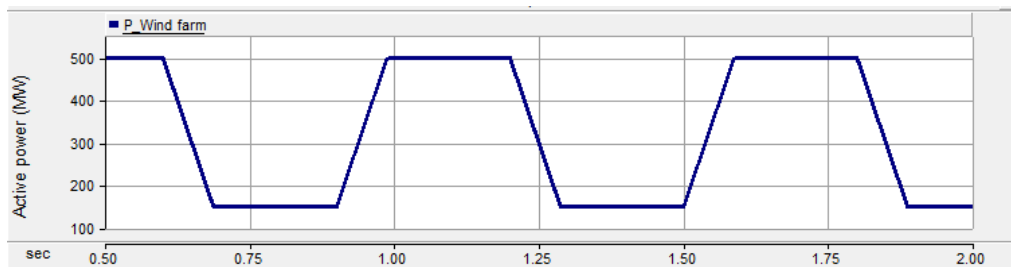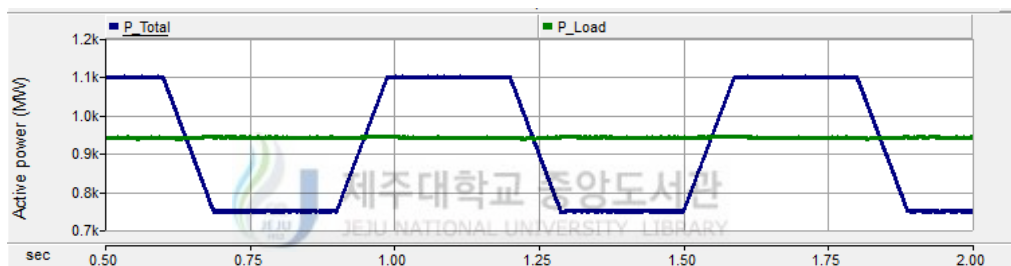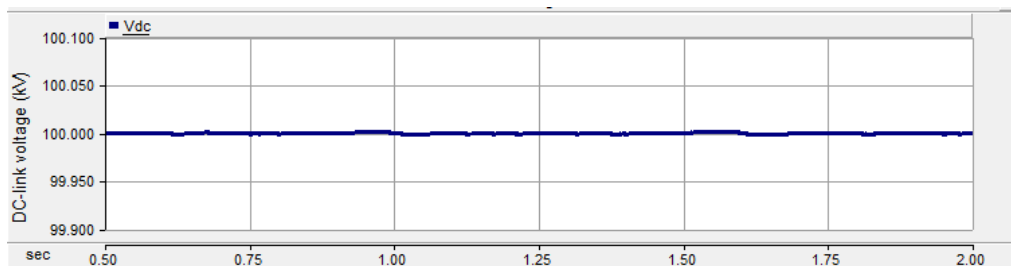

(b) Output power of wind farm

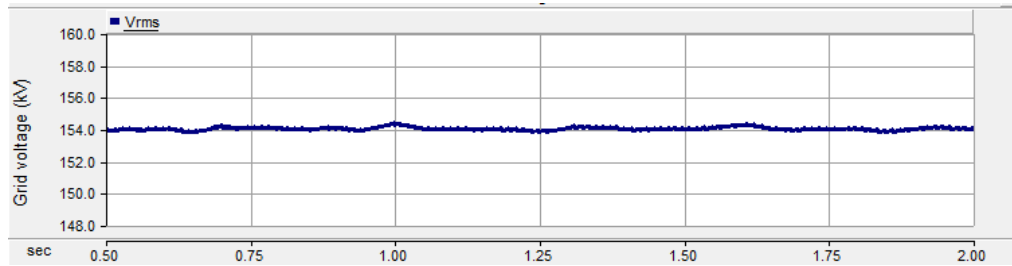(c) Total generation power and load power
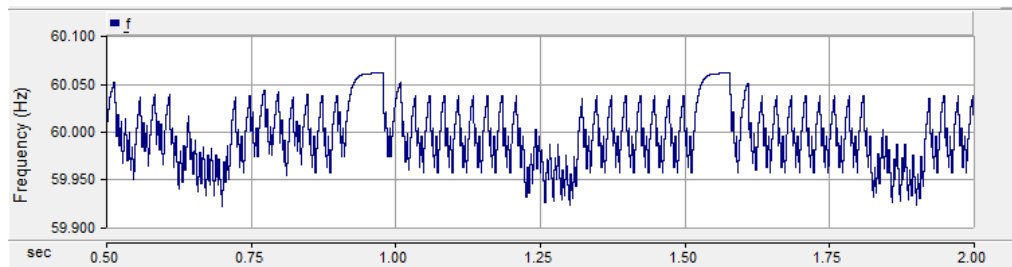

(d) Active powers of MMC-HVDC system

(e) DC-link voltage

Fig. 67 The operation of the Jeju Island power system under the variable wind speed
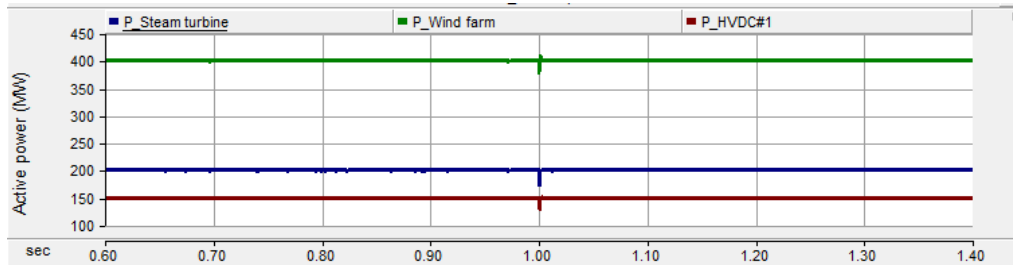
(f) Grid voltage

(g) Grid frequency

Fig. 67 The operation of the Jeju Island power system under the variable wind speed (cont.)

4.3.2 The shutdown fault of the HVDC #2

In this study case, the operation of the Jeju Island power system is as follows. The wind farms are operating with the output power of 400 MW; the powers from the steam turbines, HVDC #1, and HVDC #2 are 200 MW, 150 MW, and 250 MW as shown in Fig. 68(a)-(b). The total power generation is 1000 MW, meanwhile the demand load is 944 MW as described in Fig. 68(c). Hence, it needs to transfer 944 MW - 1000 MW = -56 MW from Jeju Island to the mainland. At t = 1.0 s, the HVDC #2 is shutdown because of the fault or overhaul. The total power generation is decreased to 750 MW due to the power of the HVDC #2 is zero. In this case, the Jeju Island power system needs to receive 944 MW - 750 MW = 194 MW from the mainland. The power which is transferred by the MMC-HVDC system is shown in Fig. 68(d). Although the HVDC #2 is disconnected suddenly, the DC-link voltage is still kept at its reference value in the steady-state time (Fig. 68(e)). There is an oscillation at the transient response of the AC voltage. However, it is not significant because it only occurs at a very short time as described in Fig. 68(f). Similarly, the frequency of the system is also stable during the shutdown fault of the HVDC #2 (Fig. 68(g)).

(a) Active powers of steam turbine, wind farm, and HVDC #1
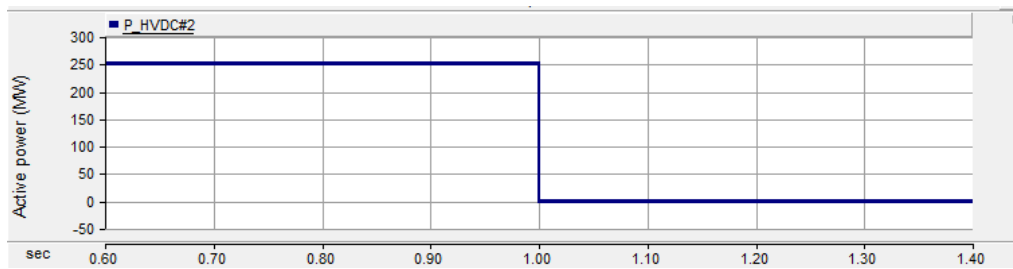
(b) Active power of HVDC #2
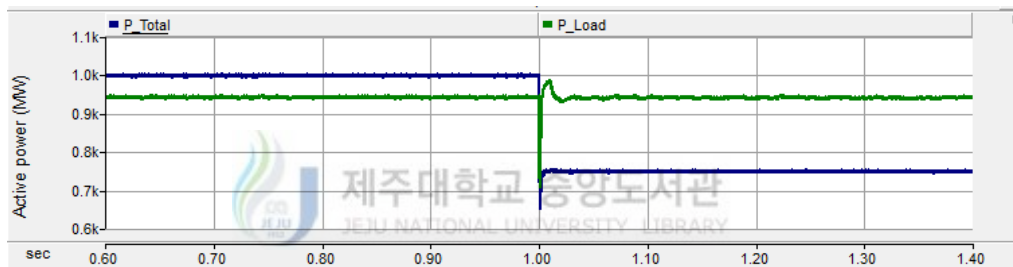
(c) Total generation power and load power

(d) Active powers of MMC-HVDC system
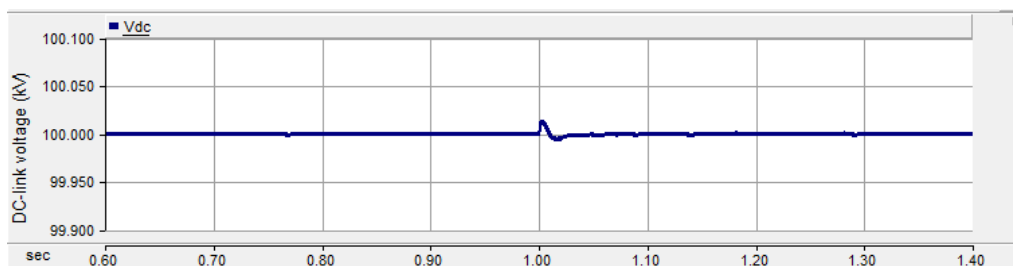
(e) DC-link voltage

Fig. 68 The operation of the Jeju Island power system under the shutdown fault
of the HVDC #2
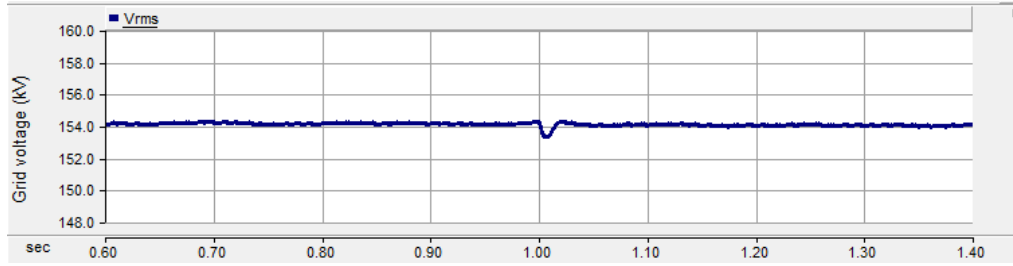
(f) Grid voltage
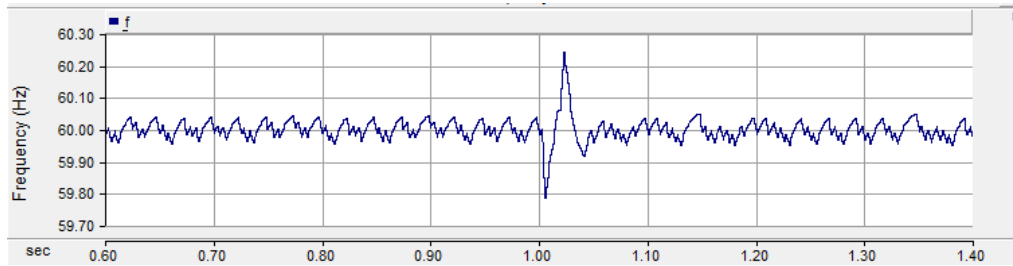
(g) Grid frequency

Fig. 68 The operation of the Jeju Island power system under the shutdown fault
of the HVDC #2 (cont.)

4.3.3 Short circuit fault at the mainland side
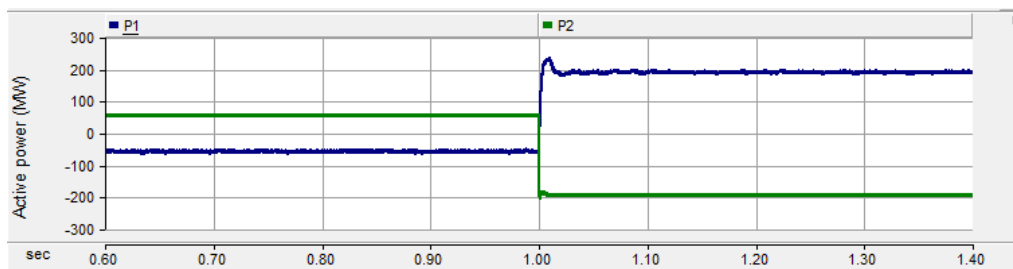
In case of single phase to ground fault, the actual power flow through the MMC-HVDC
system is always smaller than the nominal power, $P_{MMC\text{-}HVDC\_fault} < P_{MMC\text{-}HVDC\_nom}$. As
mentioned in (145), the maximum power can be calculated by

$$P_{k\_\max} = \frac{3}{2}v_{sq\_k}^{+}.i_{q\_k\_\max} \tag{174}$$

If the maximum power is smaller than the reference power, the actual power that transfers
through the MMC-HVDC system will be the maximum power. If the maximum power is
larger than the reference power, the actual power will follow the reference power.

In the study case, the single phase to ground fault appears at t = 0.7 s and removes at t = 1
s. The powers of the steam turbines, HVDC #1, and HVDC #2 are kept at 200 MW, 150
MW, and 250 MW, respectively. The simulation results are carried out in two cases as
shown in Fig. 69 and Fig. 70.

First case: In normal operation, when the output power of the wind farms achieves
maximum value of 500 MW (Fig. 69(b)), the total power generation on the Jeju Island power
system is 1100 MW (Fig. 69(c)). It needs to transfer 944 MW - 1100 MW = -156 MW to the

99

mainland by using the MMC-HVDC system (Fig. 69(d)). However, under the single phase to ground fault, the MMC-HVDC system can only transfer the maximum power of -105 MW (Fig. 69(d)). Therefore, it remains (-156 MW) - (-105 MW) = -51 MW on the Jeju Island power system. This amount of power can cause an overvoltage or losses on the system. To solve this problem, some wind turbines must be turned off with the power of 51 MW (Fig. 69(b)). As a result, the power system is balanced and stabilized as depicted in Fig. 69(c), (f), (g).
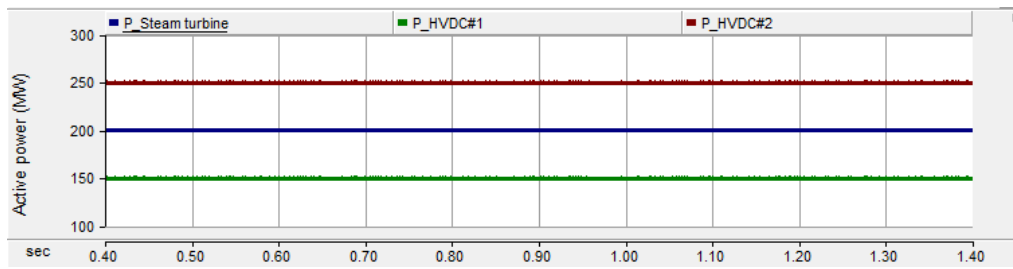
(a) Active powers of steam turbine, HVDC #1, and HVDC #2
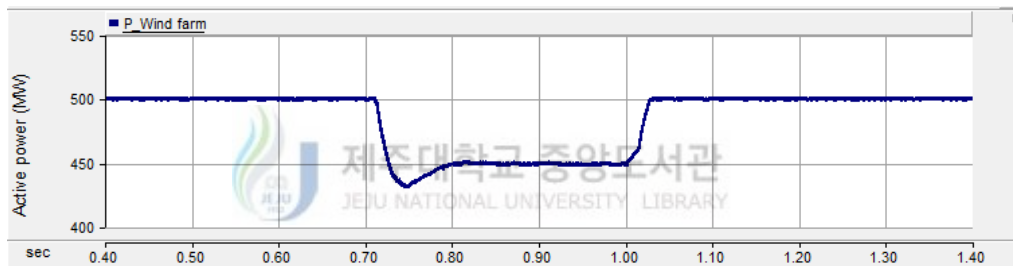
(b) Output power of wind farm
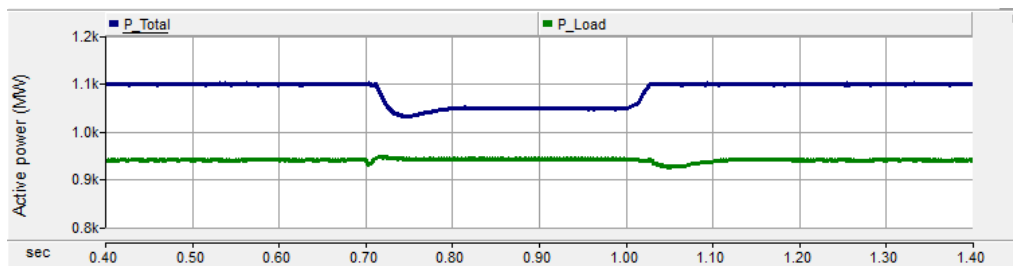
(c) Total generation power and load power
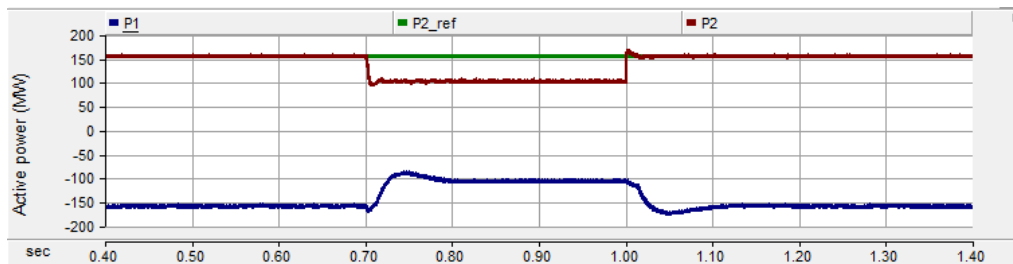

(d) Active powers of MMC-HVDC system

Fig. 69 The operation of the Jeju Island power system under the single phase to ground fault - first case

(e) DC-link voltage
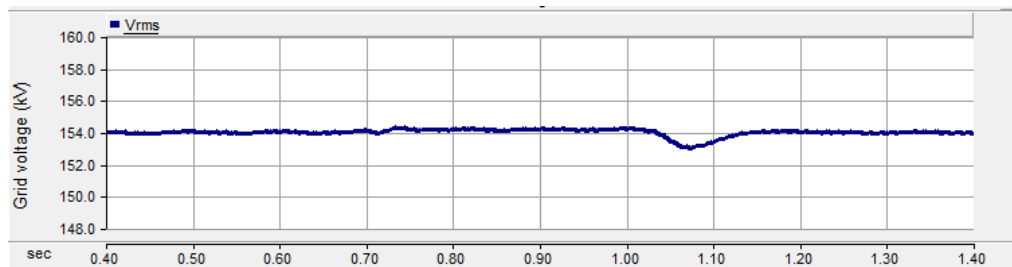
(f) Grid voltage

(g) Grid frequency

Fig. 69 The operation of the Jeju Island power system under the single phase
to ground fault - first case (cont.)

Second case: When the output power of the wind farms is minimum 150 MW (Fig. 70(b)), the total power generation on the Jeju Island power system is 750 MW (Fig. 70(c)). To balance the power system, it needs to receive 944 MW - 750 MW = 194 MW from the mainland. However, similar to the first case, the MMC-HVDC system can only transfer the maximum power of 105 MW under the single phase to ground fault. Therefore, the Jeju Island power system will be lacked 194 MW - 105 MW = 89 MW. This amount of power can cause a voltage drop or damage to the Jeju Island power system. As a result, some loads must be switched off with the power of 89 MW (Fig. 70(c)). Finally, the power system will be stabilized as shown in Fig. 70(c), (f), (g). With these control methods, the Jeju Island power system is always kept in balancing state, and the system operates with the highest efficiency.

(a) Active powers of steam turbine, HVDC #1, and HVDC #2

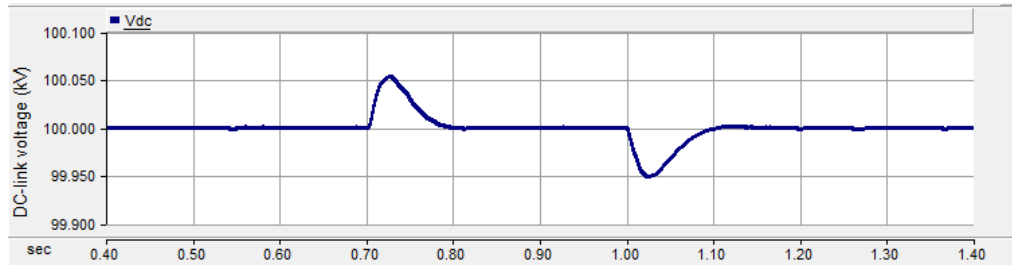(b) Output power of wind farm

(c) Total generation power and load power
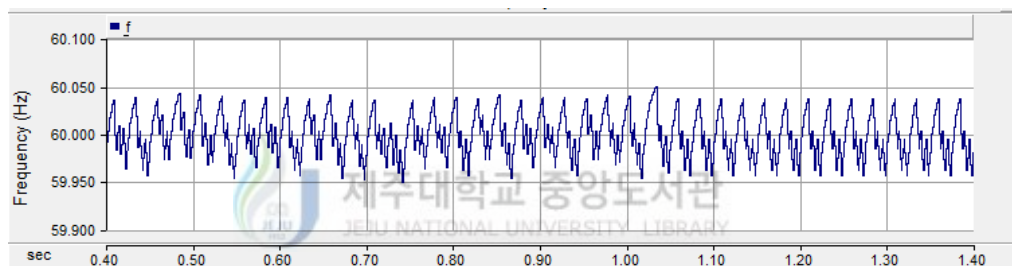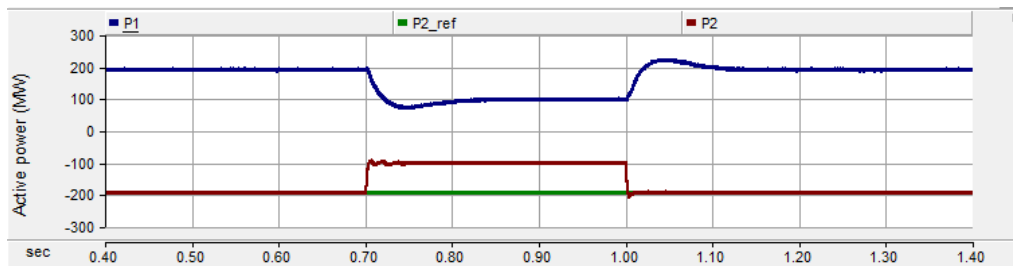

(d) Active powers of MMC-HVDC system

(e) DC-link voltage

Fig. 70 The operation of the Jeju Island power system under the single phase
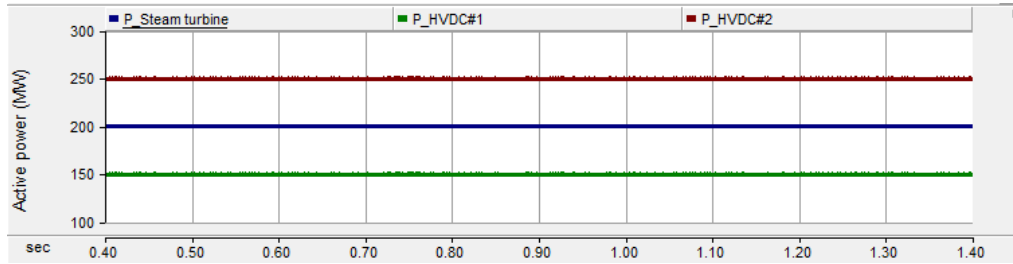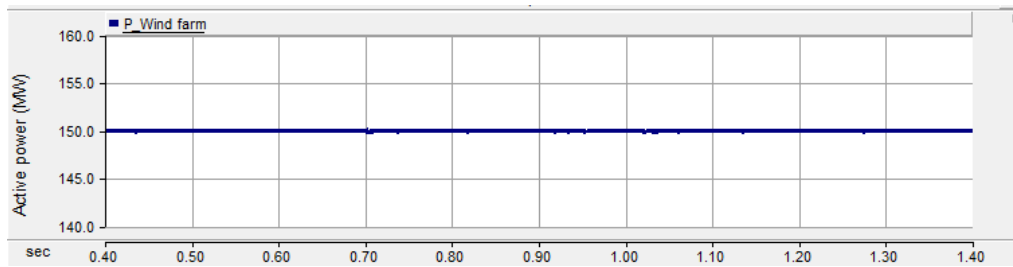to ground fault - second case

(f) Grid voltage
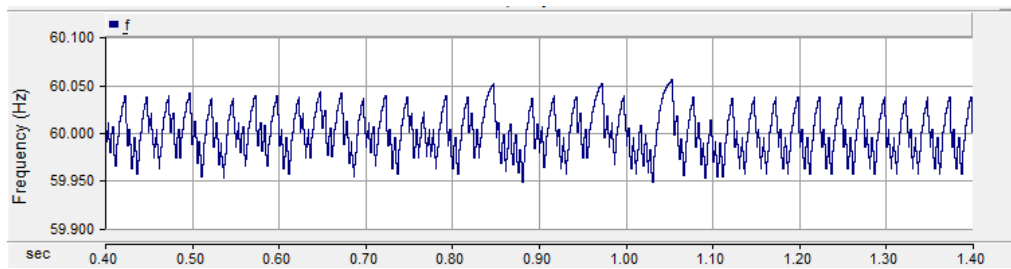
(g) Grid frequency

Fig. 70 The operation of the Jeju Island power system under the single phase
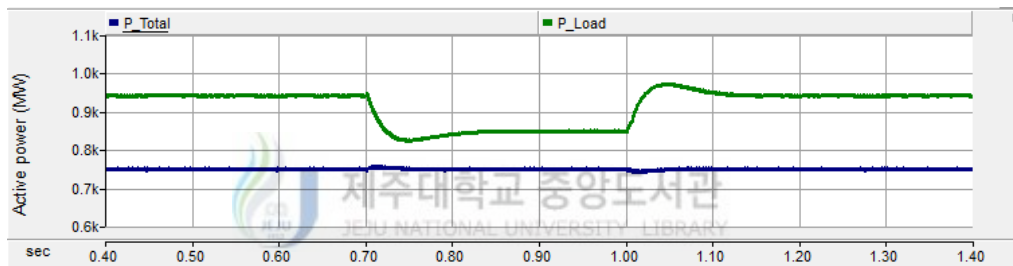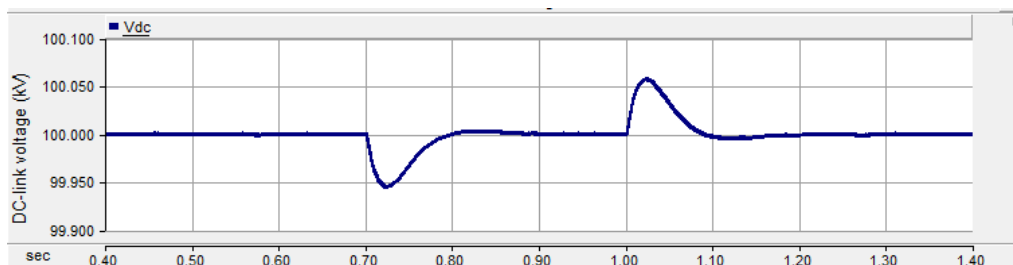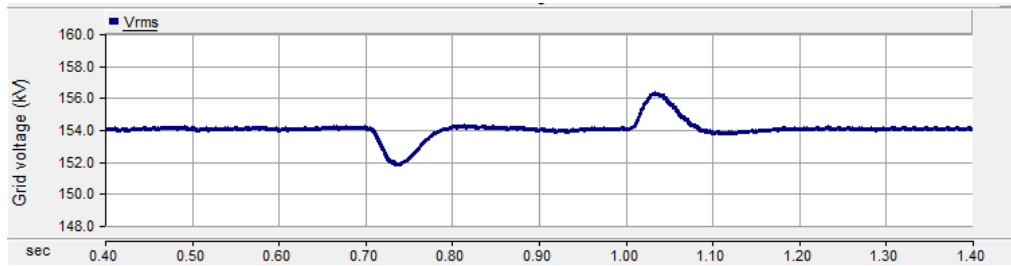to ground fault - second case (cont.)

Chapter 5. Conclusions

This dissertation presents the control methods of the MMC-HVDC system under various operating conditions and its application to the Jeju Island power system. The controls of the MMC-HVDC system are based on the fast inner control loop, the outer power and voltage control loops. Under the normal operating conditions, the MMC-HVDC system operates as a VSC-HVDC system. It can control the active and reactive powers independently, support the reactive power for the power system and control the active power in bi-direction. The effectiveness of the capacitor voltage balancing control and circulating current control is proven. The circulating current is controlled to zero, meanwhile the capacitor voltages in the arm are balanced.

Under the unbalanced voltage conditions, the control methods of the MMC-HVDC system are based on the inner current control loop. If the PI current controller is used, the inner current controller will be divided to the positive and negative sequence current controllers. Three methods to calculate the reference currents are presented. By eliminating the negative sequence currents, the converter can operate safely because the AC three-phase current is limited. The converter can be in dangerous situations when the oscillation of the active and reactive powers is eliminated. This is due to the converter injects the negative sequence currents into the power system. The existence of the negative sequence currents causes a serious overcurrent in the converter. Therefore, this control method should be avoided. If the PR current controller is used, the negative sequence currents will be eliminated directly in the αβ-frame. A decomposition of the positive and negative sequence currents is not necessary. The effectiveness of the PI and PR current controllers is almost similar together. Although the negative sequence currents are eliminated, the ripples in the DC current still remain. A modification of the inner control loop is proposed to eliminate the zero sequence component of the circulating current. As a result, the ripples in the DC current are suppressed.

Under the nonpermanent DC fault, the protection method for the MMC-HVDC system is proven effectively. This is done by connecting two thyristor switches in parallel to the diode D_2 of the SM. As soon as the nonpermanent DC fault is detected, the MMC-HVDC system moves to the protection mode. After the thyristor switches are switched on, the DC fault will become the AC fault, and the DC fault current is extinguished. Then, the MMC-HVDC system will be back to the normal operation without tripping.

The application of the MMC-HVDC system to the Jeju Island power system has been also investigated in this dissertation. It is demonstrated that the response of the MMC-HVDC system is excellent. It not only transfers the active power, but also supports for the grid voltage. The grid voltage of the Jeju Island power system with the MMC-HVDC system is more stable than that with the LCC-HVDC system. Because of the development of the demand load and wind power in Jeju Island, the installation of a new HVDC system, MMC-HVDC system or HVDC #3, in 2020 is proposed. The MMC-HVDC system is connected between the mainland and Jeju Island power systems. The operation of the MMC-HVDC system in this case is tested in three cases such as the variable wind speed, the shutdown fault of the HVDC #2 and the short circuit fault at the mainland side. The simulation results demonstrate that the MMC-HVDC system has excellent responses to stabilize for the Jeju Island power system under various operating conditions.

References

[1] O. Heyman, L. Weimers, and M. Bohl, "HVDC - A key solution in future transmission systems," *WEC Montreal 2010*.

[2] J. Varley, "HVDC: Fifty years on," *Modern Power Systems*, vol. 24, no. 10, pp. 18-20, 2004.

[3] V. K. Sood, *HVDC and FACTS Controllers*, Boston: Kluwer Academic Publishers, 2004.

[4] R. Marquardt, A. Lesnicar, and J. Hildinger, "Modulares stromrichterkonzept für netzkupplungsanwendungen bei hohen spannungen," *ETG Conference 2002, Bad Nauheim,* 2002.

[5] A. Lesnicar and R. Marquardt, "An innovative modular multilevel converter topology suitable for a wide power range," *Power Tech Conference Proceedings, 2003 IEEE Bologna,* vol. 3, Jun. 2003.

[6] S. Allebrod, R. Hamerski, and R. Marquardt, "New transformerless, scalable modular multilevel converters for HVDC-transmission," *IEEE Power Electronics Specialists Conference, 2008. PESC 2008*, pp. 174-179, Jun. 2008.

[7] Y. Zhao, X. H. Hu, G. F. Tang, and Z. Y. He, "A study on MMC model and its current control strategies," *2010 2nd IEEE International Symposium on Power Electronics for Distributed Generation Systems (PEDG)*, pp. 259-264, Jun. 2010.

[8] L. G. Franquelo, J. Rodriguez, J. I. Leon, S. Kouro, R. Portillo, and M. A. M. Prats, "The age of multilevel converters arrives," *IEEE Industrial Electronics Magazine*, vol. 2, no. 2, pp. 28-39, Jun. 2008.

[9] HVDC- High Voltage Direct Current Transmission, http://www.energy.siemens.com/ hq/pool/hq/power-transmission/HVDC/HVDC-Classic/HVDC-Classic_Transmission_ References_en.pdf

[10] N. Mahimkar, G. Persson, and C. Westerlind, "HVDC technology for large scale offshore wind connections," *Smartelec, Vadodara,* Apr. 2013.

[11] Alstom, HVDC-VSC: Transmission technology of the future, http://www.alstom.com/Global/Grid/Resources/Documents/Smart%20Grid/Think-Grid-08-%20EN.pdf.

[12] A. Antonopoulos, L. Angquist, and H.-P. Nee, "On dynamics and voltage control of the modular multilevel converter," *13th European Conference on Power Electronics and Applications, 2009. EPE '09*, pp. 1-10, Sep. 2009.

[13] M. Hagiwara and H. Akagi, "Control and experiment of pulsewidth-modulated modular multilevel converters," *IEEE Transactions on Power Electronics*, vol. 24, no. 7, pp. 1737-1746, Jul. 2009.

[14] S. Rohner, S. Bernet, M. Hiller, and R. Sommer, "Modulation, losses, and semiconductor requirements of modular multilevel converters," *IEEE Transactions on Industrial Electronics*, vol. 57, no. 8, pp. 2633-2642, Aug. 2010.

[15] Q. Tu, Z. Xu, H. Huang, and J. Zhang, "Parameter design principle of the arm inductor in modular multilevel converter based HVDC," *2010 International Conference on Power System Technology (POWERCON)*, pp. 1-6, Oct. 2010.

[16] Q. Tu, Z. Xu, and J. Zhang, "Circulating current suppressing controller in modular multilevel converter," *IECON 2010 - 36th Annual Conference on IEEE Industrial Electronics Society*, pp. 3198-3202, Nov. 2010.

[17] Q. Tu, Z. Xu, and L. Xu, "Reduced switching-frequency modulation and circulating current suppression for modular multilevel converters," *IEEE Transactions on Power Delivery*, vol. 26, no. 3, pp. 2009-2017, Jul. 2011.

[18] M. Saeedifard and R. Iravani, "Dynamic performance of a modular multilevel back-to-back HVDC system," *IEEE Transactions on Power Delivery*, vol. 25, no. 4, pp. 2903-2912, Oct. 2010.

[19] Q. Tu, Z. Xu, Y. Chang, and L. Guan, "Suppressing DC voltage ripples of MMC-HVDC under unbalanced grid conditions," *IEEE Transactions on Power Delivery*, vol. 27, no. 3, pp. 1332-1338, Jul. 2012.

[20] M. Guam and Z. Xu, "Modeling and control of a modular multilevel converter-based HVDC system under unbalanced grid conditions," *IEEE Transactions on Power Electronics*, vol. 27, no. 12, pp. 4858-4867, Dec. 2012.

[21] R. Teodorescu, F. Blaabjerg, M. Liserre, and P. C. Loh, "Proportional-resonant controllers and filters for grid-connected voltage-source converters," *in IEE Proceedings Electric Power Applications,* vol. 153, no. 5, pp. 750-762, Sep. 2006.

[22] M. P. Bahrman, "HVDC transmission overview," *IEEE PES Transmission and Distribution Conference and Exposition, 2008. T&D*, pp. 1-7, Apr. 2008.

[23] Y. Li, L. Luo, C. Rehtanz, S. Ruberg, and F. Liu, "Realization of reactive power compensation near the LCC-HVDC converter bridges by means of an inductive filtering method," *IEEE Transactions on Power Electronics*, vol. 27, no. 9, pp. 3908-3923, Sep. 2012.

[24] B. R. Andersen, L. Xu, P. J. Horton, and P. Cartwright, "Topologies for VSC transmission," *Power Engineering Journal*, vol. 16, no. 3, pp. 142-150, Jun. 2002.

[25] N. Flourentzou, V. G. Agelidis, and G. D. Demetriades, "VSC-based HVDC power transmission systems: An overview," *IEEE Transactions on Power Electronics*, vol. 24, no. 3, pp. 592-602, Mar. 2009.

[26] N. Ahmed, S. Norrga, H.-P. Nee, and A. Haider, "HVDC supergrids with modular multilevel converters - The power transmission backbone of the future," *2012 9th International Multi-Conference on Systems, Signals and Devices (SSD)*, pp. 1-7, Mar. 2012.

[27] The Grid Code, Issue 4 Revision 2, 2010, National Grid Electricity Transmission.

[28] Siriroj Sirisukprasert, "Optimized Harmonics Stepped-Waveform for Multilevel Inverter," MSc. Thesis, Department of Electrical and Computer Engineering, Virginia Polytechnic Institute and State University (Virginia Tech), Sep. 1999.

[29] G. S. Konstantinou and V. G. Agelidis, "Performance evaluation of half-bridge cascaded multilevel converters operated with multicarrier sinusoidal PWM techniques," *4th IEEE Conference on Industrial Electronics and Applications, 2009. ICIEA 2009*, pp. 3399-3404, May 2009.

[30] V. K. Chinnaiyan, J. Jerome, J. Karpagam, and T. Suresh, "Control techniques for multilevel voltage source inverters," *International Power Engineering Conference, 2007. IPEC 2007*, pp. 1023-1028, Dec. 2007.

[31] G. Carrara, S. Gardella, M. Marchesoni, R. Salutari, and G. Sciutto, "A new multilevel PWM method: A theoretical analysis," *IEEE Transactions on Power Electronics*, vol. 7, no. 3, pp. 497-505, Jul. 1992.

[32] A. K. Gupta and A. M. Khambadkone, "A space vector PWM scheme for multilevel inverters based on two-level space vector PWM," *IEEE Transactions on Industrial Electronics*, vol. 53, no. 5, pp. 1631-1639, Oct. 2006.

[33] Z. Li, P. Wang, H. Zhu, Z. Chu, and Y. Li, "An improved pulse width modulation method for chopper-cell-based modular multilevel converters," *IEEE Transactions on Power Electronics*, vol. 27, no. 8, pp. 3472-3481, Aug. 2012.

[34] M. Guan, Z. Xu, and H. Chen, "Control and modulation strategies for modular multilevel converter based HVDC system," *IECON 2011 - 37th Annual Conference on IEEE Industrial Electronics Society*, pp. 849-854, Nov. 2011.

[35] X. Yang, J. Li, X. Wang, W. Fan, and T. Q. Zheng, "Circulating current model of modular multilevel converter," *2011 Asia-Pacific Power and Energy Engineering Conference (APPEEC)*, pp. 1-6, Mar. 2011.

[36] K. Ilves, S. Norrga, L. Harnefors, and H.-P. Nee, "Analysis of arm current harmonics in modular multilevel converters with main-circuit filters," *2012 9th International Multi-*

Conference on Systems, Signals and Devices (SSD), pp. 1-6, Mar. 2012.

[37] K. Ilves, A. Antonopoulos, S. Norrga, and H.-P. Nee, "Steady-state analysis of interaction between harmonic components of arm and line quantities of modular multilevel converters," *IEEE Transactions on Power Electronics*, vol. 27, no. 1, pp. 57-68, Jan. 2012.

[38] Q. Song, W. Liu, X. Li, H. Rao, S. Xu, and L. Li "A steady-state analysis method for a modular multilevel converter," *IEEE Transactions on Power Electronics*, vol. 28, no. 8, pp. 3702-3713, Aug. 2013.

[39] A. Yazdami and R. Iravani, *Voltage-Sourced Converters in Power Systems*, Willy-IEEE in Press, 2010.

[40] J. Qin and M. Saeedifard, "Predictive control of a modular multilevel converter for a back-to-back HVDC system," *IEEE Transaction on Power Delivery*, vol. 27, no. 3, pp. 1538-1547, Jul. 2012.

[41] N. C. Scott, D. J. Atkinson, and J. E. Morrell, "Use of load control to regulate voltage on distribution networks with embedded generation," *IEEE Transactions on Power Systems*, vol. 17, no. 2, pp. 510-515, May 2002.

[42] W. Gong, S. Hu, and H. Xu, "Robust current control design of voltage source converter under unbalanced voltage conditions," *2013 IEEE PES Asia-Pacific Power and Energy Engineering Conference (APPEEC)*, pp. 1-5, Dec. 2013.

[43] J. S. Chen, W. Zhang, and P. Zhang, "Coordinated control strategy of DFIG for balanced currents and constant torque during grid voltage unbalance," *2013 International Conference on Electrical Machines and Systems (ICEMS)*," pp. 368-371, Oct. 2013.

[44] P. Rodriguez, A. Luna, M. Ciobotaru, R. Teodorescu, and F. Blaabjerg, "Advanced grid synchronization system for power converters under unbalanced and distorted operating conditions," *IECON 2006 - 32nd Annual Conference on IEEE Industrial Electronics*, pp. 5173-5178, Nov. 2006.

[45] J. W. Moon, C. S. Kim, J. W. Park, D. W. Kang, and J. M. Kim, "Circulating current control in MMC under the unbalanced voltage," *IEEE Transactions on Power Delivery*, vol. 28, no. 3, pp. 1952-1959, Jul. 2013.

[46] H. S. Song and K. H. Nam, "Dual current control scheme for PWM converter under unbalanced input voltage conditions," *IEEE Transactions on Industrial Electronics*, vol. 46, no. 5, pp. 953-959, Oct. 1999.

[47] N. T. Quach, J. H. Ko, D. W. Kim, and E. H. Kim, "An application of proportional-resonant controller in MMC-HVDC system under unbalanced voltage conditions," *Journal of Electrical Engineering & Technology*, vol. 9, no. 5, pp. 1746-1752, Sep. 2014.

[48] Y. Gao, M. Bazargan, L. Xu, and W. Liang, "DC fault analysis of MMC based HVDC system for large offshore wind farm integration," *2nd IET Renewable Power Generation Conference (RPG 2013)*, pp. 1-4, Sep. 2013.

[49] X. Li, Q. Song, W. Liu, H. Rao, S. Xu, and L. Li, "Protection of nonpermanent faults on DC overhead lines in MMC-based HVDC systems," *IEEE Transactions on Power Delivery*, vol. 28, no. 1, pp. 483-490, Jan. 2013.

[50] E. H. Kim, J. H. Kim, S. H. Kim, J. Choi, K. Y. Lee, and H. C. Kim, "Impact analysis of wind farms in the Jeju Island power system," *IEEE Systems Journal*, vol. 6, no. 1, pp.134-139, Mar. 2012.

[51] F. Zhang, K. Cho, J. Choi, Y. M. Lee, and K. Y. Lee, "A study on wind speed prediction using artificial neural network at Jeju Island in Korea II," *2011 IEEE 54th International Midwest Symposium on Circuits and Systems (MWSCAS), Seoul, South Korea*, pp. 1-4, Aug. 2011.

[52] N. T. Quach, D. H. Lee, H. C. Kim, and E. H. Kim, "Application of MMC-HVDC system for regulating grid voltage based on Jeju Island power system," *The Transactions of the Korean Institute of Power Electronics*, vol. 19, no. 6, Dec. 2014.

[53] N. T. Quach, D. H. Lee, H. C. Kim, and E. H. Kim, "Analyzing stability of Jeju Island power system with modular multilevel converter based HVDC system," *Journal of Electrical Engineering & Technology*, vol. 10. no. 1, Jan. 2015.